UNIVERSITY OF OKLAHOMA
GRADUATE COLLEGE

ULTRA-LOW CROSS POLARIZATION ANTENNA ARCHITECTURES FOR MULTI-FUNCTION PLANAR PHASED ARRAYS

A DISSERTATION
SUBMITTED TO THE GRADUATE FACULTY
in partial fulfillment of the requirements for the
Degree of
DOCTOR OF PHILOSOPHY

By

JOSÉ DAVID DÍAZ DIÁZ
Norman, Oklahoma
2021

ULTRA-LOW CROSS POLARIZATION ANTENNA ARCHITECTURES FOR MULTI-FUNCTION PLANAR PHASED ARRAYS

A DISSERTATION APPROVED FOR THE
SCHOOL OF ELECTRICAL AND COMPUTER ENGINEERING

BY THE COMMITTEE CONSISTING OF

Dr. Jorge L. Salazar-Cerreño, Chair

Dr. Caleb J. Fulton

Dr. Hjalti H. Sigmarsson

Dr. Robert D. Palmer

Dr. Alberto M. Marino Valle

This dissertation is dedicated to my parents Tito and Magali, for sacrificing so much of their lives for their children's education and future.

Esta disertación es dedicada a mi papá y mamá Tito y Magali, por sacrificar gran parte de sus vidas por la educación de sus hijos y su futuro.

Acknowledgments

I would like to first acknowledge my research advisor and chair Dr. Jorge L. Salazar-Cerreño for taking a chance on me as an undergraduate student back in 2014 at the National Center for Atmospheric Research in Boulder, CO. Dr. Salazar's passion for teaching and research resonated with me early on, making me realize what I wanted to do for a career. I'm very grateful for his support, patience, and encouragement.

I want to express my gratitude to my committee members Dr. Caleb J. Fulton, Dr. Hjalti H. Sigmarsson, Dr. Robert D. Palmer, and Dr. Alberto M. Marino for taking time from their busy schedules to help me learn, expand my knowledge in and outside of the classroom, engaging in insightful discussions, listening to my crazy ideas, and for their continuous support in this work. I also want to thank my friend and co-worker Dr. Nafati Aboserwal. Dr. Aboserwal's support was pivotal in the development of this dissertation, providing very insightful comments and advice throughout the whole process. I also want to extend my gratitude to the Advanced Radar Research Center (ARRC) faculty and staff for their never-ending support and commitment to the students making the ARRC feel like a home away from home. To my friends in the PAARD team: thank you for all the wonderful memories that made my days brighter and more enjoyable. Special thanks to Dr. Javier Ortiz, Dr. David Schvartzman, Dr. Rodrigo Lebron, Dr. Arturo Umeyama, and future Dr. Tony

Segales.

I also want to thank my entire family for supporting and believing in me. Tito and Magali (i.e., papi y mami), words alone cannot express my deep appreciation for the life you gave me. Thank you for teaching me hard work, perseverance, kindness, humility, and unconditional care for others. You are my role models and who I want to be when I grow up. The pillar of my family, my sister Soly. Thank you for never doubting my capabilities and for being the best sister that I could have ever asked for. I was only able to complete this goal knowing that you were there for our family. To my brother Junito, thank you for keeping life fun and interesting, and always showing me a good time. Uncle Eulalio, thank you for encouraging me to strive for greatness and for advising me in life. Last but not least, to my better half and best friend Melissa Rosa, with whom I'm sharing my life and starting a beautiful feline family. Thank you for jumping into the unknown, feeding me delicious food, being my personal editor, and trusting me in this crazy journey.

Table of Contents

List of Tables

List of Figures

Abstract

For over thirty years, single-beam mechanically steered radars have dominated the field of atmospheric observations, and since then, newer improved technologies have emerged that could provide a replacement for aging radars. Phased array radar technology offers meteorologists and scientists a unique opportunity to enhance weather forecasting through rapid electronic adaptive scans. Multiple array geometries exist for phased array radars (i.e., spherical, cylindrical, and planar); however, this work concentrates on enhancing the performance of planar antenna architectures. Planar phased array radar antennas have been under scrutiny due to the challenges posed when trying to satisfy all polarimetric weather requirements met by conventional parabolic dish reflectors (e.g., co-polarized beam mismatch under 0.1 dB, input isolation higher than 40 dB, cross-polarized radiation under -40 dB). This dissertation takes a fresh look into the electromagnetic characteristics of traditional antennas used in planar phased array geometries and provides mathematical insight to prove their performance, limitations, and advantages. The metrics used to evaluate essential performance characteristics were bandwidth, scanning range, polarization, co-polarized beam match, cross-polarization, isolation, and intrinsic cross-polarization (IXR).

The antennas presented in this work (i.e., Horus, Polarimetric Atmospheric Imaging Radar (PAIR), and Horus-ONR) were validated by comparing the results of predictive simulating tools against physical antenna measurements. The Horus antenna was made using aperture coupling feeding technique with stacked microstrip patches. It achieved a fractional bandwidth of 15.4%, a co-polarized beam mismatch of 0.08 dB, and scanned cross-polarization levels of -29 dB, based on Ludwig's third definition of polarization for $\theta_s = \pm 45°$. The PAIR antenna was made using balanced probe-fed stacked microstrip patches and it totaled fractional bandwidths of 7.7%, co-polarized beam mismatch of 0.21 dB, and -40 dB cross-polarization within the required imaging field of view. Lastly, the Horus-ONR antenna. Its design follows Horus guidelines for manufacturing but improves bandwidths up to 24.8% by trading the scanned co-polarized beam mismatch and cross-polarization required for weather missions. Other antenna architectures proposed for future phased array radar developments are the ultra-low cross-polarization microstrip patch (ULCP-MPA) and a dielectric covered slot antenna (ULCP-DCSA). The ULCP-MPA and the ULCP-DCSA can achieve cross-polarization levels of -40 dB for $\theta_s = \pm 45°$. The antenna designs presented in this dissertation show the lowest scanned cross-polarizations with highly calibratable polarization and might be the best planar radiating elements present in literature so far, despite not achieving all polarimetric weather requirements for multi-function phased array radars. Microstrip patch antennas offer a scalable, low profile solution with excellent polarization diversity and reasonable scanned bandwidths for multi-function, planar phased array radar platforms of the future.

Chapter 1

Introduction

1.1 Preface

Phased array technology originated in the first quarter of the 20th century [1] and it experienced significant advancements during World War II [2]. Since its beginnings, phased array technology was applied to radar tracking applications [3]. In more recent times, phased array antenna technology evolved to be introduced into everyday applications such as: radio broadcasting [4], satellite internet [5], and cellular communications [6]. Currently, phased array radar systems are positioned to become the next generation of polarimetric weather radars [7]–[9].

When compared to single-beam mechanically scanned radars, phased array radars provide a plethora of benefits, including: rapid update of fast-developing events which can increase warning time for hazardous weather, tailored scan patterns that might improve rainfall estimates, and rapid update of developing weather through adaptive scanning [8].

As a part of the initiative to replace the existing weather and air surveillance radar networks, the ARRC at the University of Oklahoma initiated the development of a Line Replaceable Unit (LRU) Phased Array Radar (PAR)

a) Line Replaceable Unit (completed)

b) Mobile All-digital PAR (currently in development)

c) All-digital PAR Testbed Concept

Figure 1.1: Horus radar system renderings. a) The 8 x 8, dual-polarized fully digital line replaceable unit (LRU) was completed and tested in Spring 2020 at the ARRC. b) The mobile radar platform is scheduled for completion in Winter 2021. c) Rendering of a full-scale all-digital PAR testbed. Images courtesy of the ARRC's Engineering Department. Drawings not to scale.

(see Fig. 1.1). This fully digital, dual-polarized weather radar building block named "Horus", after the Egyptian god of war and sky, allows full control of transmitted and received signals of each antenna element; providing high flexibility for beamforming techniques and scanning strategies [10].

1.2 Motivation

Dual-polarized weather radars require both low cross-polarization (lower than -40 dB) and well matched co-polar patterns (less than 0.1 dB co-polar beam mismatch) to successfully retrieve the polarimetric products (Z_{DR}, ϕ_{DP}, and ρ_{HV}) of a scanned atmosphere sector [11]–[13]. Weather polarimetry established the most stringent and restraining requirements among all radar users in terms of antenna performance, due to the required high polarization purity of the aperture. For this reason, the design of any phased array weather radar requires achieving the same or improved antenna performance, when compared to single-beam mechanically scanned apertures. However, no antenna in a planar phased array architecture has been capable of satisfying these requirements. Additional details about this shortcoming are given in Sections 1.4 and 2.1.1.

1.3 Previous Work

The Doppler Weather Surveillance Radar (WSR-88D) operates since 2011 with a dual-polarized parabolic dish reflector capable of rotating in azimuth 360° and elevation angles starting at 0.5°[14]. Due to the nature of the scan, in which the parabolic reflector is always perpendicular to the plane where measurements are retrieved, the antenna produces extremely low cross-polarization radiation (30 dB lower than the beam peak) with negligible differences between radiated beam peaks [15]. In contrast, a phased array version of the WSR-88D should operate without mechanical rotation, introducing some major challenges into the analysis related to cross-polarization levels and co-polar beam matching [13]. A possible solution for some of these issues is a phased array aperture that has a cylindrical shape [16]. Another possible solution is the correction of the biases introduced by a planar phased array antenna through calibration [17]. Nevertheless, either approach is limited by the embedded element pattern of the phased array aperture [18]. Several antenna architectures have been proposed in the literature to satisfy the requirements of the next generation of weather radars [19]–[26].

This next generation of weather radars exploits Printed Circuit Board (PCB) technology for antenna manufacturing. PCB technology allows for high accuracy designs at relatively low costs when mass produced [27]. For this reason, most solutions are based on microstrip antennas. However, PCB technology also imposes manufacturing challenges based on the dielectric substrate characteristics of the stackup (e.g., dielectric material, dielectric permittivity, dielectric thickness, etc.). Nonetheless, with improved design, manufacturing challenges currently present for microstrip antennas can be mitigated.

A microstrip antenna is a type of planar resonator, as shown in Fig. 1.2. Traditionally, the resonator is made from a thin layer of copper mounted on a dielectric substrate material with a backing ground plane. Microstrip patch antennas are versatile in terms of resonant frequency, polarization, radiation pattern, and impedance [28]. Depending on the feeding technique used to excite the resonator, more flexibility is achieved in terms of bandwidth, cross-polarization, and efficiency. In general, the feeding techniques used for microstrip patch antennas are divided into contact and non-contact feeding techniques, as discussed in further detail in Sections 1.3.1 and 1.3.2.

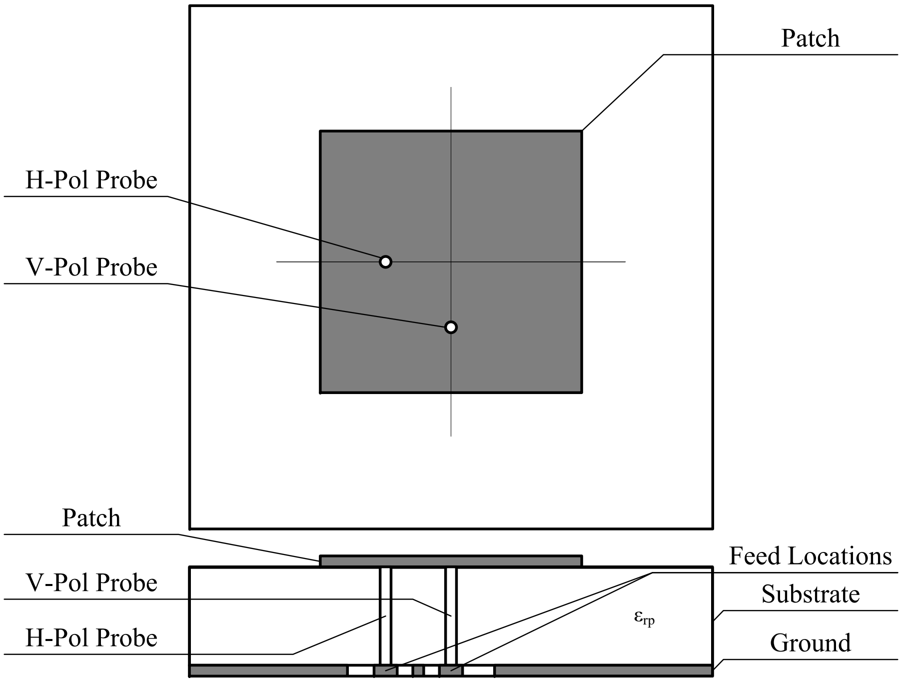

Figure 1.2: Top and side view of the dual-polarized probe-fed microstrip patch antenna geometry in where ϵ_{rp} is the permittivity for the microstrip patch dielectric substrate.

1.3.1 Contact-fed Microstrip Patch Antennas

Contac-fed in the context of microstrip patch antennas refers to a continuous form of connection between the microstrip patch and the feeding network. Probe-fed microstrip patches as shown in [19]–[22] use a probe to couple energy directly to the microstrip patch, as shown in Fig. 1.2. In [19]–[21], four probes are excited (two for each polarization), with a phase difference of 180° between each polarization pair, portrayed in Fig. 1.3. This balanced-fed configuration enforces a symmetry plane between horizontal (H) and vertical (V) polarizations resulting in exceedingly low cross-polarization levels and nearly equal frequency responses. Specific to [19], [20], no backing ground plane was incorporated in the antenna which makes work from [21] rather unique. The presence of

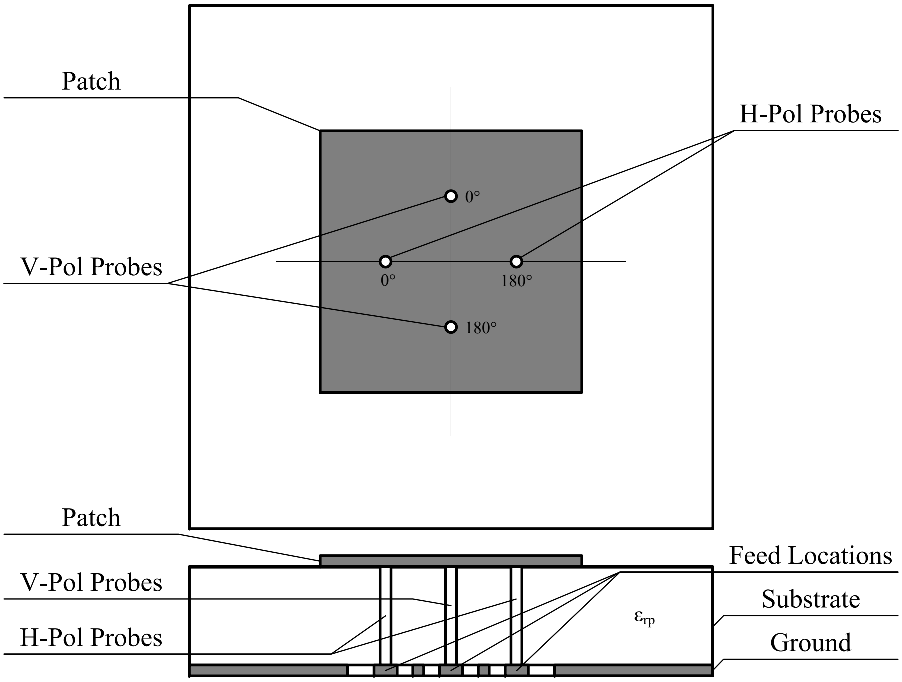

Figure 1.3: Top and side view of the dual-polarized balanced probe-fed microstrip patch antenna geometry in where ϵ_{rp} is the permittivity for the microstrip patch dielectric substrate.

the ground plane acts as a radiation stopper for the feeding network that is necessary to excite the antenna. When incorporated, it can reduce the potential of cross talk between the elements in the back of the array. Other drawbacks in this geometry are related to the feeding network.

First and foremost, there is a risk of introducing a scan blindness in the antenna if it is designed with a reactive hybrid balun [29], like the ones used in [20], [21]. Secondly, PCB technology limits how tall a via can be on a given substrate [27], while the height of the substrate is proportional to the bandwidth [30]. For this reason, most of these designs are limited to bandwidths of about 10% [28]. Lastly, there is the possibility of spurious radiation from the probes that can increase cross-polarization levels [28]. Despite all their drawbacks, balanced probe-fed microstrip patch antennas are solid contenders to satisfy the requirements of the next generation of weather radars. Today, this antenna design can be found in multiple phased arrays, including the Advanced Technology Demonstrator (ATD) [19].

Other forms of direct contact feeding techniques used with microstrip antennas involve a transmission line (TL) that connects directly to the patch. Dual-polarized microstrip-fed patch antennas like the one shown in Fig. 1.4 offer the advantage of integrating the feeding network in the same layer of the radiator (patch). Unfortunately, in phased array weather radars this advantage poses no positive impact and might prove detrimental to the design. The presence of the microstrip line can introduce significant levels of spurious radiation capable of driving the cross-polarization higher than required in a dual-polarized PAR for weather applications.

Another approach to mitigate some of the spurious radiation in this configuration is using two transmission lines to feed each polarization. With 180° phase shift between the two lines that excites each polarization, vertical and horizontal symmetry planes can be obtained. This approach is similar to the probe-fed design with four vias directly connected to the microstrip patch without transmission lines. Due to its similarities, the microstrip-fed patch has not become part of the antennas proposed for phased array weather radars.

Comments on Contact-fed Microstrip Patch Antennas

Even though different dielectric substrate stackups and antenna sizes were used, when scanning in the vertical and horizontal planes, [19]–[22] reported cross-polarization levels ranging from -35 to -45 dB. In the diagonal plane, all works reported levels of cross-polarization of about -25 dB. In terms of

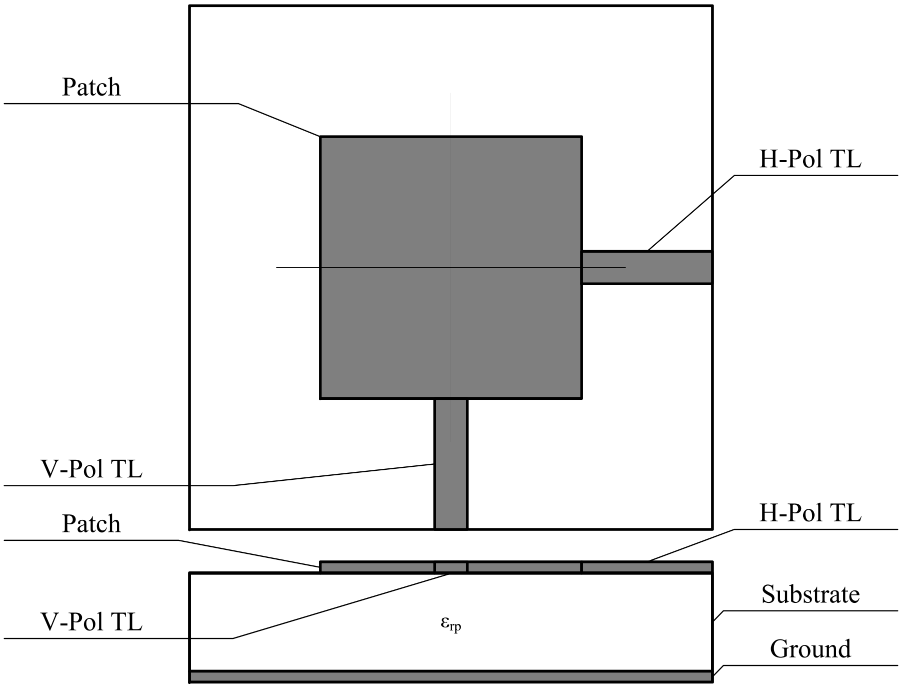

Figure 1.4: Top and side view of the dual-polarized transmission line-fed microstrip patch antenna geometry in where ϵ_{rp} is the permittivity for the microstrip patch and the transmission line dielectric substrate.

scanning, the balanced probe feeding architecture showed scanning capabilities in $-45^\circ \leq \theta \leq 45^\circ$. Given the consistency of these results, it can be said that the balanced probe feeding technique seems to be dictating the achievable cross-polarization in these antennas. On the other hand, none of these designs comply with the weather requirements of cross-polarization for simultaneous transmit and receive (STSR) radar operation [13]. This requirement dictates than even in the diagonal plane, cross-polarization levels of -40 dB are needed to avoid bias in the polarimetric variables Z_{DR} and ϕ_{DP}. For this reason, a calibration procedure that corrects the cross-polarization introduced in the measurements is needed when using these antennas.

1.3.2 Non-contact Fed Microstrip Patch Antennas

Non-contact fed in microstrip patch antennas implies that the patch is not in direct contact with the feeding network. These forms of feeding techniques usually experience higher bandwidths at the cost of a more complex design [31], [32]. Some of the non-contact feeding techniques that can be used for weather radars are the aperture and proximity coupling. The aperture coupling technique, as shown in Fig. 1.5, consists of a transmission line that excites a slot in the ground plane. The slot then is responsible of coupling the energy to the patch. This form of excitation allows tuning the feeding network (aperture and transmission line) independently from the patch geometry which turns into greater flexibility for impedance control [33]. Also, given that the ground plane separates the feeding network and the microstrip patch, low cross-polarization levels can be achieved. Works from [22]–[25] are examples of apertured couple patch antennas that have been proposed for weather radars.

In [22], the two-probe feeding is combined with the aperture coupling technique to make a hybrid dual-polarized antenna element. With this hybrid configuration, cross-polarization levels in the order of -40 dB in the principal planes (E- and H-plane) can be obtained with scanning capabilities of $-45^\circ \leq \theta \leq 45^\circ$. However, a critical factor is missing in the design: a backing ground plane to ease integration on a system and avoid possible interaction of the antenna elements in the back of the array. The aperture coupled patch antennas shown in [23] and [25] deal with this issue using striplines instead of microstrip lines to excite the apertures. Nonetheless, they were designed for applications in which multiple antennas are combined in the same feeding network making it difficult to wage the performance of the element on its own.

Another form of the aperture coupled patch antennas was presented in [24],

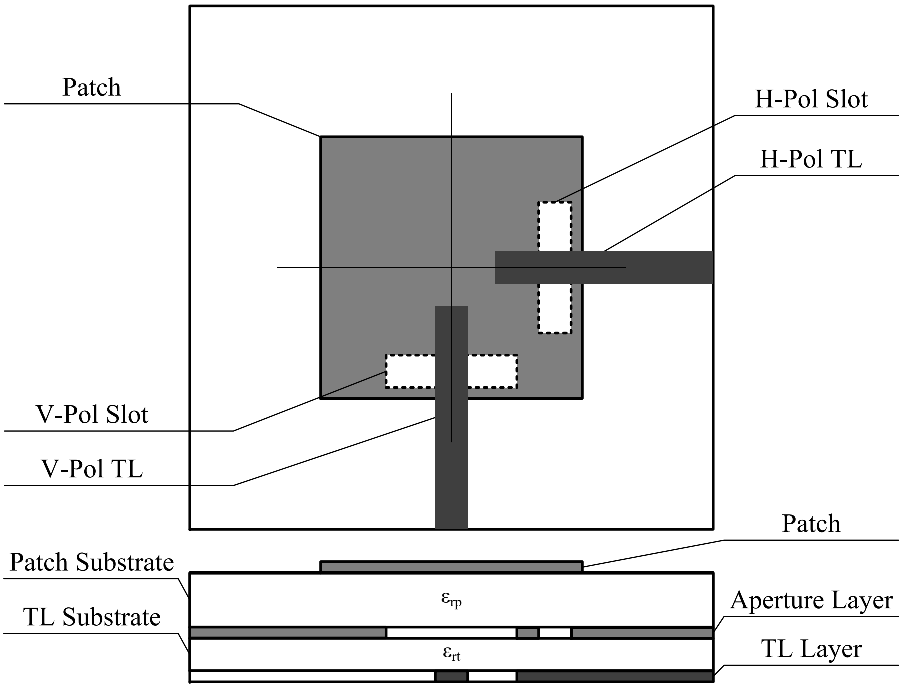

Figure 1.5: Top and side view of the dual-polarized aperture coupled microstrip patch antenna geometry in where ϵ_{rp} and ϵ_{rt} are the permittivity for the microstrip patch and the transmission line dielectric substrates, respectively.

[34]. In contrast to [23] and [25], the separated slots from Fig. 1.5 are combined into one aperture in the center of the ground plane, underneath the microstrip patch as shown in Fig. 1.6. This geometry offers other benefits when compared to the two independent slots configuration. First, by combining both apertures, a symmetry plane for both polarizations can be drawn which could lead to lower cross-polarization levels. Secondly, by separating both polarizations with the ground plane, higher isolation between both polarizations can be obtained which can also lead to lower cross-polarization. Finally, both H- and V- feeding networks can be independently controlled to achieve better impedance control. This antenna configuration showed scanning capabilities for $-45^\circ \leq \theta \leq 45^\circ$ with sustained cross-polarization levels of about -30 dB in the same region.

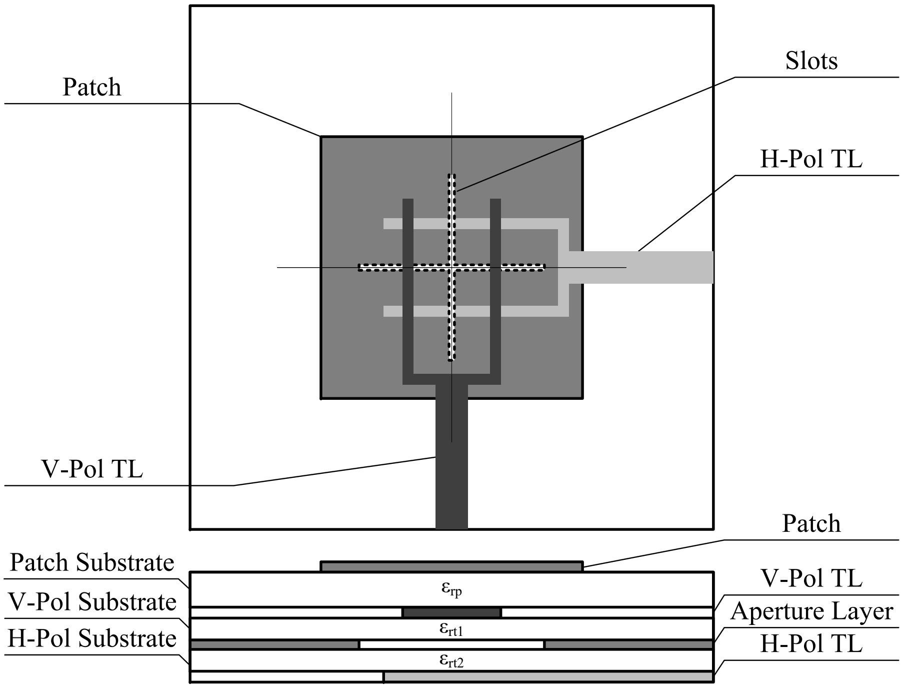

Figure 1.6: Top and side view of the centered-fed dual-polarized aperture coupled microstrip patch antenna geometry in where ϵ_{rp} and ϵ_{rt} are the permittivity for the microstrip patch and the transmission line dielectric substrates, respectively. Notice, ϵ_{rt1} is not necessarily equal to ϵ_{rt2}.

Unfortunately, there are drawbacks related to its feeding network.

Given that H- and V-polarizations can be independently tuned, the design of the antenna is rather complex. Moreover, for one of the polarizations, part of the probe that excites the transmission line would be exposed underneath the radiator. This probe has the potential of producing spurious radiation that can raise the cross-polarization of the antenna. Additionally, the architecture does not contain a backing ground plane, which can result in possible interactions between the antennas in the back of the array. Despite these drawbacks, this architecture was one of the final candidates to become part of the Airborne Phased Array Radar (APAR), to be operated for weather-related research in a

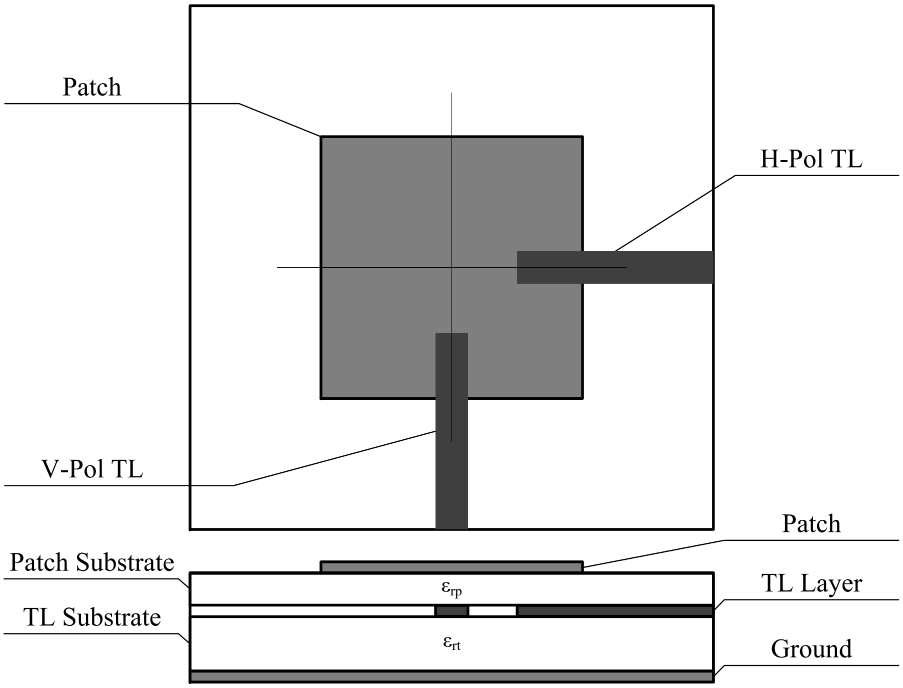

Figure 1.7: Top and side view of the dual-polarized proximity coupled microstrip patch antenna geometry in where ϵ_{rp} and ϵ_{rt} are the permittivity for the microstrip patch and the transmission line dielectric substrates, respectively.

C-130 aircraft [24].

The other form of non-contact feeding for microstrip patch antennas is the proximity coupling. Proximity coupling, as shown in Fig. 1.7, uses a transmission line in close proximity to the microstrip patch as an excitation. Like microstrip-fed patch antennas, two more transmission lines can be added (one to each polarization) to balance the feeds and obtain symmetric planes for the excitations as it was presented in [35]. Out of all of the other feeding mechanisms for a patch antenna, proximity coupling exhibits the highest operational bandwidth [28], [36]. Proximity coupling also allows high flexibility for impedance matching given that the dielectric substrate for the transmission line does not have to be the same as the one for the microstrip patch. However, these advantages do not come without drawbacks. Even though symmetrical planes are established in the vertical and horizontal planes, the feeding transmission lines are still exposed above the ground plane which can introduce spurious radiation in the antenna. Proximity coupling microstrip patch antennas have not been integrated on any phased array weather radar project at the time this document was written.

Comments on Non-contact Fed Microstrip Patch Antennas

In contrast to contact-fed, non-contact fed microstrip patch antennas allow independent tunning of the feeding network, to control the impedance response of the resonator with the added advantage of wider bandwidths. Moreover, non-contact fed microstrip patch antennas have shown cross-polarization levels that are comparable to those presented in the balanced probe fed architecture. These results are rather intriguing given that two different feeding mechanisms exhibit similar results for scanning performance and cross-polarization, even though multiple dielectric substrate stackup configurations were used. On the other hand, the results are also somewhat disappointing. None of the presented feeding mechanisms for microstrip patch antennas have been able to lower the cross-polarization levels to those required by weather polarimetry. From these results, it appears that a fundamental limit on the achievable cross-polarization is being imposed on microstrip patch antennas. This limit seems to depend on physical characteristics of the radiator and is not necessarily related to the feeding network.

1.3.3 Non-standard PCB Antennas

Rather than using standard PCB manufacturing techniques, some authors have proposed antenna designs that benefit from PCB technology but requires non-standard assembly procedures. The most famous example of this architecture is the printed crossed dipole antenna [26]. The printed crossed dipole antenna, as shown in Fig. 1.8, uses PCB technology to produce a microstrip line version of a dipole with a reactive balun on a dielectric substrate. A dual-polarized radiator can be made by introducing a notch from the top and through the vertical center of the antenna and combining it with another that has the complementary cut (i.e., a cut from the bottom of the antenna through the vertical center). To direct the energy, a mounting slotted ground plane is introduced at the dipole's base. To make the antenna operational, the different ground planes should be combined. This can be achieved by using soldering paste or any conductive material that can bond them together and realize a continuous ground.

In terms of performance, the printed crossed dipole antenna presented in [37] cross-polarization levels below -40 dB in the vertical and horizontal planes. Unfortunately, the scanning capability of the antenna out of the principal planes was not shown. In a later publication by the same author [38], the cross-polarization for a 6 x 6 scanned array was shown to be -30 dB in the diagonal plane. As it is known from the literature [39], the measured cross-polarization in a small array is not going to be the same as the one predicted by the embedded element pattern due to the presence of edge effects in the truncated non-infinite ground. Even though promising, it is not clear what will be the performance of this crossed dipole on a planar phased array architecture.

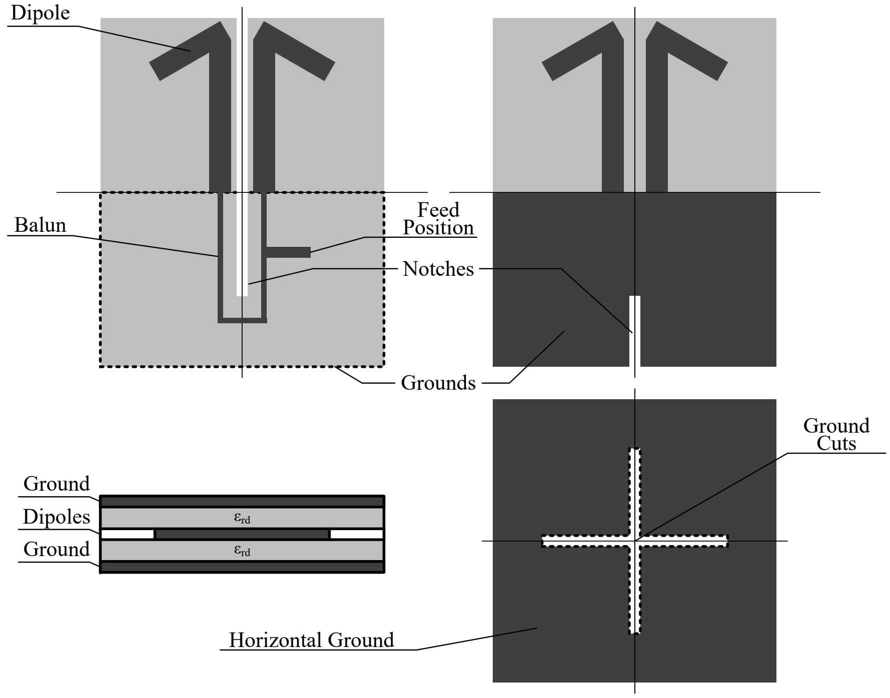

Figure 1.8: Top and side view of the printed crossed dipole antenna geometry in where ϵ_{rd} is the permittivity of the dipole dielectric substrate.

1.4 Problem Statement

After reviewing the literature for radiating elements that could satisfy all weather polarimetry requirements in PARs (e.g., scanned cross-polarization levels of -40 dB), is clear that no antenna has shown the capability of fulfilling these in a planar phased array. In fact, all reviewed antennas would need to rely on some sort of bias calibration procedure to compensate for cross-polarization and co-polar beam mismatch introduced in the measurements. For this reason, there is a gap in the weather community for functional antenna elements that can exhibit scanned cross-polarization of -40 dB and low co-polar beam mismatch under real world conditions.

1.5 Justification

Dual-polarized antennas with scanned cross-polarization levels of -40 dB and perfect co-polar beam mismatch can be found in theory. They are modeled as a superimposed electric-magnetic dipole element. Alas, these antennas cannot be made for practical designs. They cannot be made because the dipoles radiate energy in almost all directions without a ground plane. Then, when they are placed with a ground plane to make the antenna directive, the reflected energy from the ground plane suffers a phase offset that introduces cross-polarization and co-polar beam mismatch. In practice, the reflected radiation from the ground can be controlled. In other words, there might be an antenna architecture that can show some degree of destructive interference in the cross-polarization with minimal co-polar beam mismatch when some physical characteristics of the design are properly tuned.

1.6 Hypothesis

From previous works it is seen that aperture coupled microstrip patch antennas have shown cross-polarization improvements in the diagonal plane when compared to the balanced probe-fed configuration. However, it is difficult to say what is the reason for such improvements, especially when these could have originated from one or multiple sources within the antenna geometry. Thus, this work hypothesized that proper control of the reflections coming from the ground in planar antenna architectures would lead to lower cross-polarization levels in phased arrays and that these reflections are controlled by the physical characteristics (i.e., feeding network, dielectric substrate, and patch dimensions) of the microstrip radiator.

1.7 Research Objectives

This work requires identifying the best suited antenna element to satisfy the requirements of weather polarimetry using PARs. Therefore, to tackle the design of the best antenna architecture, one has to dive deep into the literature to comprehend the mechanisms of radiation, the behavior of microwave systems, the design of electronics, the means of calibration, the art in signal processing, and in our case, weather and polarimetry. A specific set of objectives were defined to identify which antenna element is best suited to satisfy weather polarimetry requirements in PARs.

The first objective is to determine which characteristics make one antenna better than another. In terms of polarization, the answer might be: "the antenna that offers the lowest cross-polarization". However, as one puts together the whole picture of the system, the answer is more complex than just one variable. To answer this question, we present a set of metrics established throughout the literature that would allow differentiation between multiple antennas. Some of the metrics included in the discussion are: bandwidth, scanning range, polarization, and calibration. These metrics grant an unbiased reasoning strategy when deciding which antenna element is better suited than others.

The second objective is to produce a detailed assessment of today's phased array antennas. The assessment is realized by weighing their advantages and shortcomings through rigorous theoretical and mathematical formulations. It helps us uncover what kind of antenna architectures are superior for our purposes. By the end of the study, the best suited antenna architectures to satisfy weather polarimetry requirements are identified. However, they may or may not be correlated with practical manufacturing rules.

This brings us to our third objective: antenna design trade-offs. It is imperative for the successful deployment of the Horus and other phased array radars to design antenna elements that conform to standard manufacturing techniques. We may see antenna designs that do not conform to these standards. However, by examining the performance metrics, a compromise in the antenna can be made to reach an efficient design.

Finally, our last objective: the successful design of antennas for phased arrays. The antennas are designed using all acquired knowledge in a full wave electromagnetic solver. Once manufactured, the antennas are measured and validated against the expected performance acquired with the simulator.

These objectives ultimately form the goal of making operational antenna designs for the next generation of phased array weather radars.

1.8 Contributions

Attention in the development of state-of-the-art phased array radar systems has increased over the past few years [40]–[43]. Due to these systems development, antenna designs with excellent polarization characteristics were developed and published [21], [22], [44], [45]. However, most of these designs were made without much insight into the intrinsic limitations or advantages in some antenna architectures. For this reason, one of the main contributions of this work is the compilation of robust mathematical formulations and modeling techniques that allowed us to confidently say which antenna elements are best suited for weather phased array radars.

Following these results, multiple antenna designs were made for some of the current and future platforms for the weather community. The Horus antenna [42], [44], an aperture coupled microstrip patch that includes a backing ground plane at the bottom of the structure for ease of electrical aperture integration. Made from two PCB assemblies, its flexibility allows for having the feeding network completely separated from the antenna radiators which mitigates the issue of how tall a PCB can be made. The design went directly to hold the position of lowest scanning cross-polarization antenna ever published. With expected cross-polarization levels of -30 dB in the diagonal plane and better than -45 dB in the principal planes, the Horus antenna is capable of scanning in a cone defined by $-45^\circ \leq \theta \leq 45^\circ$.

The Polarimetric Atmospheric Imaging Radar (PAIR), funded by the National Science Foundation, is a dual-polarized C-band phased array that has the potential to study tornadogenesis and other severe weather phenomena with unprecedented temporal resolution [43]. A four probe-fed microstrip antenna panel made from 5 electrical layers including a feeding network and a backing ground plane was developed: by careful design of the aperture and emphasis on reducing manufacturing costs. In terms of performance, all electrical scanning capabilities of the project were completely satisfied with this design.

To follow on the success of the Horus antenna design, a collaboration was setup with the U.S. Naval Research Laboratory to explore the model in other frequencies. This collaboration sparked the design of the ultra-low cross-polarization (ULCP) antenna. The ULCP antenna originated after finding that the dielectric substrate underneath a microstrip patch played more than a passive role in the performance of cross-polarization. Rather than using the traditional cavity model to describe the radiation characteristics of the microstrip patch, the electric current model was used. This led me to discover that an odd permittivity of about 1.7 underneath the patch would allow the antenna to reach levels of scanning cross-polarization better than the Horus antenna itself [46]. This contribution ultimately answered the question from the scientific community of what is necessary to achieve ultra-low cross-polarization in a planar phased array.

Finally, the Horus-ONR project, another state-of-the-art phased array system that is being developed at the ARRC with the support of the Office of Naval Research (ONR). Seeking to increase the bandwidth capabilities of the Horus antenna and maintain its low cross-polarization characteristics, the Horus-ONR antenna follows a similar design procedure. When compared, the Horus-ONR antenna almost doubles the bandwidth of its counterpart. Rather than having different dielectric substrate cores for radiators and feeding network, the same dielectric substrate is used for both assemblies. This advantage allows the antenna to have a lower effective permittivity when the stacks are combined which results in lower surface wave excitation on the array and admissible levels of cross-polarization. For a complete list of published literature please refer to Appendix C.

1.9 Overview of Chapters

This work is organized to present dual-polarized phased antenna designs based on robust mathematical and theoretical formulations to help satisfy weather polarimetry requirements in PARs. In chapter 2, phased array fundamentals are reviewed, and the most important performance antenna metrics are derived for planar array architectures. In chapter 3, the design trade-offs for planar phased array antennas are discussed in where special attention is made to surface waves and its implications on bandwidth and polarization. This chapter also includes a discussion of the radiation characteristics of multiple antenna elements typically used in phased arrays. In chapter 4, the design of the aperture coupled microstrip patch and the balanced probe-fed microstrip patch antenna are discussed. These chapters cover antenna modeling, design trade-offs, manufacturing, and final validation. In chapter 5, the ULCP antenna design is reviewed along with future steps on how to make a physically realizable design out of its required geometry. Finally, chapter 6 summarizes the findings of this dissertation, its conclusions, limitations, and future research.

Chapter 2

Fundamentals of Phased Array Antennas

2.1 Phased Arrays

A phased array, in antenna theory, is a combination of two or more antenna elements that can be controlled or positioned independently to constructively or destructively produce a resultant radiation pattern [47]. Phased arrays are usually depicted in three major physical geometries: *planar*, *cylindrical*, and *spherical*, as shown in Fig. 2.1. These geometries can be combined to form new array configurations depending on the volume scan required for the application.

As demonstrated throughout the literature, any of these geometries can be used for radar systems [16], [19], [48]. However, for meteorological purposes, the planar [19] and cylindrical [16] geometries have been the two major contending array configurations for the next generation of polarimetric weather radars. There are many reasons (e.g., scanning volume, gain, cross polarization, etc.) why these two array geometries are preferred for this application. When they are compared with one another (i.e., planar vs. cylindrical), it is sometimes difficult to separate which one is best suited for weather radars.

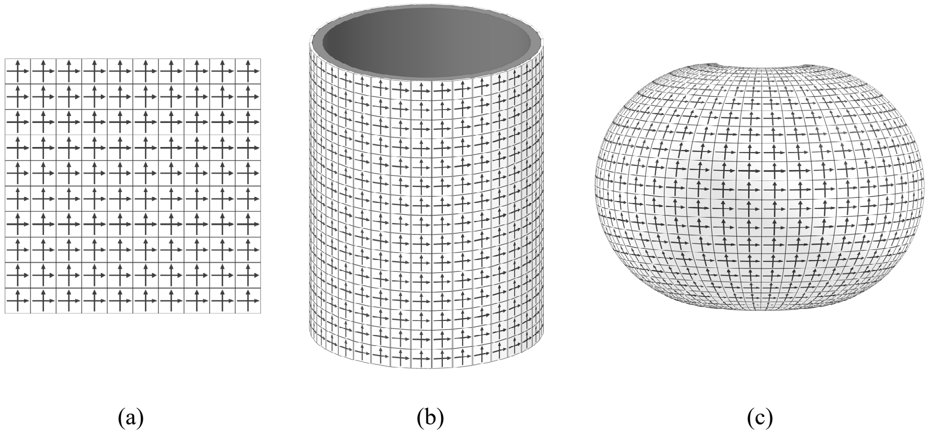
(a) (b) (c)

Figure 2.1: Phased array antenna configurations for dual-polarized antenna elements. a) planar array, b) cylindrical array, and c) spherical array.

2.1.1 Phased Array Antenna Geometries

Planar phased arrays have been making great strides towards becoming the ultimate platform for polarimetric weather radars. With combined efforts from the NSSL and MIT Lincoln Laboratory (MIT-LL), industry partners Lockheed Martin and Ball Aerospace, the Federal Aviation Administration (FAA) and others, the weather community saw the development of the Advanced Technology Demonstrator (ATD) [19]; a massive dual-polarized polarimetric radar responsible of weighing phased array technology for weather forecasting. Rather than having multiple planar faces across a given volume, the ATD uses a pedestal to rotate a planar phased array to the direction in where weather phenomena occurs. Nevertheless, as a planar phased array, the ATD exhibits the advantages and disadvantages that come with its geometry. When the radar points at boresight, it produces a beam with high efficiency and low cross polarization. However, as the excitations on the elements are changed to produce a scanning beam, the planar geometry produces disadvantages.

Examples of these are: the possibility of a surface wave that jeopardizes the scanning capability of the array, a roll-off from its maximum achievable gain that depends on the scanning angular beam position, and cross polarized radiation that is a function of the antenna that constitutes the array [47]. To compensate some of these shortcomings, the planar geometry requires a correction [49]; in contrast, these limitations are not present in the cylindrical geometry [16].

The cylindrical geometry offers an attractive solution that overcomes most of the issues associated with planar and spherical phased array geometries. First, each element distributed on the surface automatically points at boresight. When multiple elements are combined in elevation, they form a planar subarray. This arrangement gives cylindrical geometries the capability of scanning in every direction. The best example for this configuration is the Cylindrical Polarimetric Phased Array Radar (CPPAR). Developed and maintained by the ARRC, it currently serves as a demonstrator for meteorological research [16]. CPPAR effectively leverages the polarization drawbacks of both planar and spherical geometries but is not without downsides. As each column in elevation points away from each other (i.e., subarrays not aligned), there is a loss of energy in the elements that are combined horizontally. This loss of energy makes a cylindrical array radiate less efficient beams at boresight than a planar array. To scan in elevation, the antenna uses a series feed to produce beams that depend on frequency requiring wide operational bandwidths. An additional drawback of the geometry is the possibility of creeping waves on the aperture [50]. Finally, the cylindrical geometry's difficult design and manufacturing makes it especially challenging to produce. Nevertheless, a cylindrical array like CPPAR fulfills weather polarimetry requirements and shows good promise as a next generation polarimetric weather radar.

Spherical phased array radars have not been proposed to satisfy weather polarimetry requirements due to fundamental limitations in the geometry. As the elements are distributed through the spherical surface, the spacing between them is not always the same which makes the array factor and the element patterns dependent on one another. Furthermore, given that the elements are not parallel to each other, the resultant polarization might not be aligned which can result in high cross polarization [47]. This problem can be potentially mitigated by a slight modification in the spherical geometry. The Geodesic Dome Phased Array Antenna, Advanced Technology Demonstrator (GDPAA-ATD) [48], is an example of a spherical array made with multiple planar faces. The geometry used on GDPAA-ATD allows for the array factor and the element patterns to be separated, simplifying its analysis. Each face can be controlled independently to make a planar phased array radar that radiates normally to each array surface. Unfortunately, when considered as a potential solution for weather radars, this geometry suffers from critical efficiency issues due to its size.

As it was mentioned before, it is sometimes difficult to separate which configuration (planar or cylindrical) is better suited for weather radars. In an ideal world, a cylindrical phased array seems to be a more natural solution for azimuth scanning, but in a practical world, it is sometimes better to leverage all available knowledge and experience. The planar configuration offers scalable designs, easier integration, and extensive list of analysis tools for its development. Leading us to conclude that a multi-face planar phased array provides a flexible, efficient, and economic solution, when compared to spherical and cylindrical arrays. For this reason, this work focuses on evaluating the shortcomings of planar phased arrays and use them in the design of antenna elements that can offer the best performance for polarimetric weather radars.

2.2 Phased Array Fundamentals

To understand the fundamentals of planar phased array antennas, we would focus our attention to a special configuration called the linear array. A linear array is an arrangement of N radiating elements positioned on an axis and separated by a certain distance d, as shown in Fig. 2.2. These elements are usually connected to a generator that has a certain characteristic impedance Z_o. As the elements are excited, incident (V^+) and reflected voltages (V^-) can be defined at the terminals of each antenna. Due to the interaction of these voltage waves, the element feed ports can be characterized by a NxN scattering matrix defined as [51], [52],

$$S_{ij} = \left. \frac{V_i^-}{V_j^+} \right|_{V_k^+ \ = \ 0 \ for \ k \neq j} . \tag{2.1}$$

Eq. 2.1 shows that the scattering parameter S_{ij} can be found by driving port "j" with an incident voltage V^+ and measuring the reflected wave V^- coming out of port "i" while all other incident voltages are set to zero (i.e., terminated in matched loads). The total terminal voltage for the ith element can be written as

$$V_i = V_i^+ + V_i^- = V_i^+ + \sum_{j=1}^{N} S_{ij} \ V_i^+ . \tag{2.2}$$

Eq. 2.2 indicates that the total terminal voltage on the ith port is the summation of the incident voltage on the port ith and the fractional energy

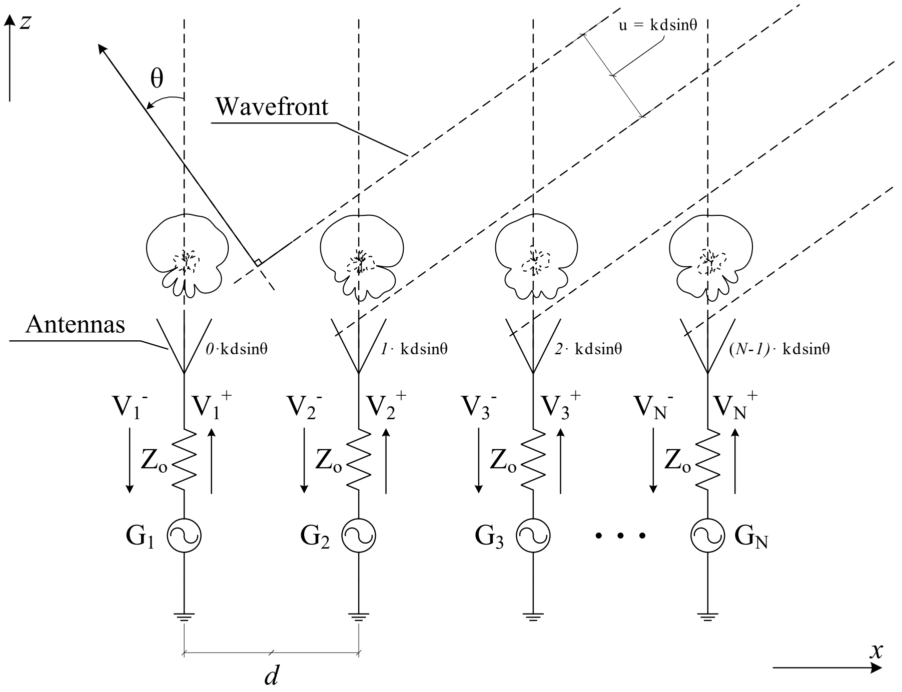

Figure 2.2: Linear phased array antenna characteristics. $V_i^{\pm}$ refers to the incident (+) and reflected voltage waves at the terminals of the “i” element, G_i to the generator, Z_o to the characteristic impedance of the generator, d to the distance between antenna elements, u to the progressive phase shift between elements to the wavefront, k to the propagation constant of the medium, and θ to the angle made by the plane wave.

that is coupled to all other terminated antenna ports. To simplify the radiation characteristics from the antennas, it is assumed that the far-field radiation produced by an element is proportional to its terminal voltage. That is, the fields radiated by a particular antenna can be expressed as

$$E_0(r, \theta) = V_0 \ f(\theta) \ \frac{e^{-jkr}}{r}, \tag{2.3}$$

where V_o is the applied terminal voltage, $f(\theta)$ the dominant radiation of the element (also known as the isolated pattern), and e^{-jkr}/r represents the spherical dependency of the propagated wave. Superimposing the energy of the elements to the same wavefront and assuming each element radiating similarly in all directions, the total radiated field of the array is given by

$$E^a(r,\theta) = f(\theta)\frac{e^{-jkr}}{r}\sum_{n=1}^{N} V_n\ e^{j(n-1)u}, \tag{2.4}$$

where element "1" is taken as a phase reference, u is given by $kd\sin\theta$, k is the propagation constant of the medium, and d the distance between elements. Then, to point energy of a beam in the θ_0 direction requires the elements to be phased by

$$V_n^+ = V_0\ e^{-j(n-1)u_0}, \tag{2.5}$$

which allows Eq. 2.4 to be rewritten when combined with Eq. 2.2 as

$$E^a(r,\theta) = f(\theta)\ \frac{e^{-jkr}}{r}\ V_0\ \sum_{n=1}^{N}\left[e^{-j(n-1)u_0} + \sum_{m=1}^{N} S_{nm}\ e^{-j(m-1)u_0}\right] e^{j(n-1)u}. \tag{2.6}$$

Eq. 2.6 shows one of the most significant results in phased array antenna theory which is that the scanned array pattern is not only a function of the radiation produced by the antennas, but is also dependent on the interaction between neighboring elements. This conclusion opens a discussion into how different antennas can influence the performance of a phased array. We will currently focus on investigating the physical characteristics of the array without considering any specific antenna. Assuming no interactions between antennas in the array, $S_{mn} \to 0$ and Eq. 2.6 reduces to

$$E^a(r,\theta) = f(\theta)\,\frac{e^{-jkr}}{r}\,V_0\sum_{n=1}^{N} e^{j(n-1)(u-u_0)}. \tag{2.7}$$

Eq. 2.7 shows how the physical characteristics of the array are tied to the overall radiation pattern produced by the aperture without considering the interaction or *mutual coupling* between antenna elements. This equation serves as an instrument to understand how the physical characteristics of the array influence the overall radiation pattern. We make use of Eq. 2.7 in Section 2.2.1 to understand the fundamentals of phased arrays without the presence of mutual coupling and later on Section 2.2.2, the discussion will continue with phased array fundamentals considering mutual coupling.

2.2.1 Linear Array without Mutual Coupling

Number of Elements

We first start by considering how the number of elements in the phased array influences the radiation pattern. From Eq. 2.7 is evident that number of elements in the array is proportional to the magnitude of the radiation pattern in the direction of θ_0 for a fixed element spacing d. Fig. 2.3a is constructed when substituting $d = \lambda_o/2$, $f = 3\ GHz$, $\theta_0 = 0^\circ$, $N = 10$, 20, or 30 elements, and normalizing each produced beam to its maximum peak. It can be seen that the main beam in the radiation pattern gets narrower as the number of elements is increased while the sidelobe levels (i.e., secondary beam peaks that are below the highest peak of radiation) remain relatively constant with a value close to -13 dB. Depending on the application, this array feature can be tuned to satisfy gain and/or beamwidth requirements.

Beam Scanning

A progressive phase shift must be introduced in each antenna element in order to scan the array. Traditionally, phase shifters are used for this task. A phase shifter is an RF component that is made from ferrites or diodes which allows to control the signal's phase at the terminals of the antenna. To demonstrate beam scanning, the progressive phase shift is calculated from $u_0 = kd \sin\theta_0$ in where θ_0 is the intended beam direction. For a beam scan of $\theta_0 = -30°$ and substituting $k = 2\pi/\lambda$, $\lambda = c/f$, $f = 3\ GHz$, and $d = \lambda_o/2$ yields $u_0 = -\pi/2$. Fig. 2.3b shows the normalized radiation pattern of a linear array scanned to $-30°$, $0°$ and $30°$. This array feature can be used to calculate the progressive phase shift for a desired beam and predict the true beam direction that depends on the resolution of phase shifters.

Weighting Functions

Sidelobes are an important metric for weather radars because their energy can interfere with measurements. A practical way to control sidelobe energy is by using weighting functions. A weighting function is a mathematical formulation that allows to control or influence the results of a predefined function. Weighting functions are traditionally implemented in antenna elements using a device called attenuator. An attenuator is an RF component made from resistors that allows to lower the magnitude of the voltage signal introduced in the antenna port. Mathematically speaking, the weighting function is introduced in Eq. 2.7 by controlling the terminal voltage on each element, making the V_0 dependent on the element position. Thus, Eq. 2.7 becomes

$$E^a(r,\theta) = f(\theta)\,\frac{e^{-jkr}}{r}\,\sum_{n=1}^{N}\,V_{0,n}\,e^{j(n-1)(u-u_0)}, \tag{2.8}$$

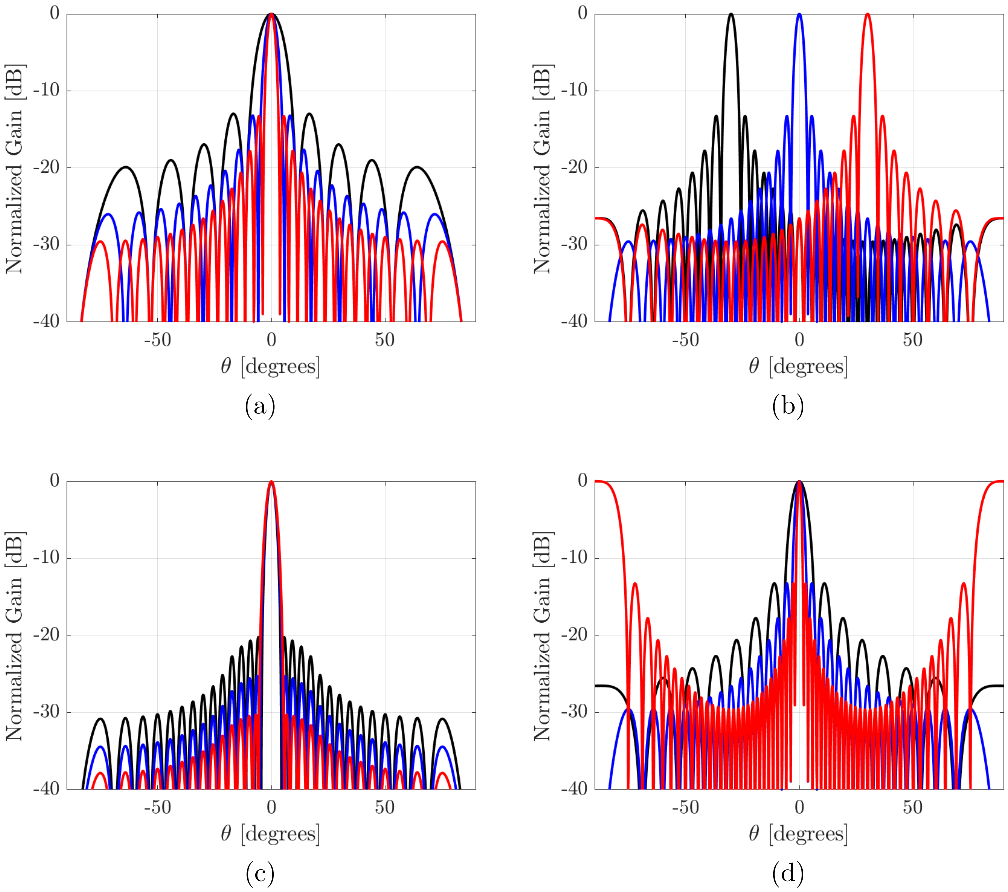

(a) (b) (c) (d)

Figure 2.3: Different linear phased array antenna configurations and characteristics. (a) Normalized radiation pattern for a linear phased array with $d = \lambda_o/2$, $f = 3\ GHz$, $\theta_0 = 0°$, and N elements: 10-black, 20-blue, 30-red. (b) Normalized radiation pattern for a linear phased array with $d = \lambda_o/2$, $f = 3\ GHz$, $N = 30$, and θ_0 scanning beams: $-30°$-black, $0°$-blue, $+30°$-red. (c) Normalized radiation pattern for a linear phased array with $d = \lambda_o/2$, $f = 3\ GHz$, $N = 30$, $\theta_0 = 0°$, and weighting Taylor function of 5 nearly constant sidelobes: -20-black, -25-blue, -30-red. (d) Normalized radiation pattern for a linear phased array with $f = 3\ GHz$, $N = 30$, $\theta_0 = 0°$, and d spacings: $\lambda/4$-black, $\lambda/2$-blue, λ-red.

where $V_{0,n}$ refers to the terminal voltage in the nth element. Fig. 2.3c shows the normalized radiation pattern using a Taylor weighting function with 5 nearly constant sidelobe levels of -20, -25, and -30 dB. The linear array in consideration has $d = \lambda_o/2$, $f = 3\ GHz$, $N = 30$, $\theta_0 = 0°$. It's important to mention that the use of weighting functions is not limited to sidelobe level. Some weighting functions are tailored to control the main beam shape in terms of beamwidth or magnitude and others in suppressing interferences from measurements.

Array Spacing

The spacing between elements in a phased array is responsible of setting most of the radiation characteristics of the aperture. To understand how the spacing controls the radiation characteristics of the array, let us consider the case of a linear array with a fixed number of elements N. For a given operational frequency f and intended beam pointing direction $\theta_0 = 0°$, no matter the spacing between the elements, the array would always produce constructive energy resulting in a main peak of radiation at $\theta = 0°$. In all other directions, the radiation between the elements is combined constructively or destructively resulting in a pattern that depends on the array spacing d. However, it is also true that when $u - u_0 = 2\pi m$, where m can take the value of any integer, the phased array would produce other main peaks of radiation. These secondary peaks of radiation are called grating lobes and for most applications, including ours, they are an unwanted source of radiation. For a grating lobe to exist in the θ_g direction, the relation $u - u_0$ must satisfy

$$2\pi\frac{d}{\lambda}(\sin\theta_g - \sin\theta_0) = 2\pi m \rightarrow \sin\theta_g = \sin\theta_0 + m\lambda/d, \qquad (2.9)$$

for $|\sin\theta_g| \leq 1$. To illustrate the radiation pattern characteristics as a function of the spacing d, we substitute in Eq. 2.7: $f = 3\ GHz$, $N = 30$, $\theta_0 = 0°$ and $d = \lambda_o/4, \lambda_o/2$, and λ_o. The results of the substitution are presented in Fig. 2.3d. It is clear that when $d = \lambda_o$, two secondary peaks of radiation are produced in ±90°; which is consistent with Eq. 2.9 in the case where $m = \pm 1$. Comparing with the other results, the beamwidth produced with this configuration ($d = \lambda$) is narrower than when $d = \lambda_o/4$ or $\lambda_o/2$ even though all have the same number of elements. This result is part of the tradeoffs of phased array design in which the beamwidth, sidelobe levels, and gain can be influenced by the size of the aperture; which is in turn a function of the array spacing. For a polarimetric PAR for weather observations, all of this flexibility is somewhat constricted by the requirement of not having grating lobes in the radiation pattern. To derive a spacing criteria that avoids the presence of any grating lobes requires Eq. 2.9 to be rewritten as

$$d_{max} \leq \frac{\lambda_o}{1 + \sin\theta_{max}}, \tag{2.10}$$

where d_{max} refers to the maximum allowable spacing in the array before introducing grating lobes at the reduced scanning angle θ_{max}. This condition says that in order to scan the array from $\theta = -90°$ to $90°$, the spacing between elements has to be lower than $\lambda/2$. For a weather radar intended to scan from $\theta = -45°$ to $45°$, the spacing condition increases to 0.586λ at the highest operational frequency. As we have seen, the spacing between elements play an important role in the radiation characteristics of planar phased arrays. However, we have been disregarding the effects of mutual coupling. In the next section we focus on the effects of mutual coupling in planar phased arrays.

2.2.2 Linear Array with Mutual Coupling

Mutual coupling in phased arrays is often referred to as the interaction between antenna elements. This interaction occurs in the form of electromagnetic energy and is highly dependent on the physical characteristics of the antenna that makes the array. The radiation characteristics of a phased array including mutual coupling are given by Eq. 2.6, in where it is assumed that each element on the array is driven with the same excitation and radiating similarly in all directions. For $S_{mn} \neq 0$, microwave theory [51] defines the active reflection coefficient (ARC) for the "mth" element as

$$\Gamma_m(\theta) = \frac{V_m^-}{V_m^+} \tag{2.11}$$

where V_m^+ refers to the directed and V_m^- to the reflected voltage waves at the terminals of the antenna. The ARC for the linear array can be found from Eqs. 2.2 and 2.5 as

$$\Gamma_m(\theta) = \frac{V_m^-}{V_m^+} = \frac{\sum_{n=1}^{N} S_{mn}\ e^{-j(n-1)u}}{e^{-j(m-1)u}} = \sum_{n=1}^{N} S_{mn}\ e^{-j(n-m)u}. \tag{2.12}$$

The ARC is a bridge between the physical characteristics of the array or aperture and the intrinsic parameters of the antenna element. It can be used to predict how the excited array would perform under different operational conditions (i.e., across frequency, angular scanning position, etc.). According to Eq. 2.12, the ARC can be found by adding the mutual coupling terms (i.e., S_{mn} terms for $m \neq n$) with the self-reflections (S_{mn} where $m = n$) of the "mth" element. Now, let us consider the active element pattern (AEP) for the "mth" element in which we set all other neighboring generators to 0 (i.e., $V_n^+ = V_0$

for $m = n$ and $V_n^+ = 0$ for $m \neq n$ while $V_n^- = S_{nm}V_0$). Using Eq. 2.4 and substituting directed and reflected voltages, the AEP for the "mth" element is written as

$$E_m^e(r,\theta) = f(\theta)\frac{e^{-jkr}}{r}\ V_0\left[e^{j(m-1)u} + \sum_{n=1}^{N} S_{nm}\ e^{j(n-1)u}\right]. \tag{2.13}$$

In the case in where all elements are passive (i.e., $S_{mn} = S_{nm}$), we can rewrite the ARC from Eq. 2.12 as

$$\Gamma_m(-\theta) = e^{-j(m-1)u}\sum_{n=1}^{N} S_{nm}\ e^{j(n-1)u}, \tag{2.14}$$

thus, allowing the AEP to be rewritten in terms of the ARC as

$$E_m^e(r,\theta) = f(\theta)\frac{e^{-jkr}}{r}\ V_0\left[1 + \Gamma_m(-\theta)\right]e^{j(m-1)u}. \tag{2.15}$$

Notice that all of the previous discussions have assumed $f(\theta)$ as the dominant component of radiation or electric fields. Following a similar procedure as for E_m^e, the magnetic fields for the "mth" element can be written for a normalized feed line characteristic impedance (i.e., $I_m^+ + I_m^- = V_m^+ - V_m^-$) as

$$H_m^e(r,\theta) = f(\theta)\frac{e^{-jkr}}{r}\ \frac{V_0}{\eta_0}\left[1 - \Gamma_m(-\theta)\right]e^{j(m-1)u}, \tag{2.16}$$

where η_0 is the intrinsic impedance of the medium. Using Eqs. 2.15 and 2.16, [53] shows the gain of the embedded element pattern

$$G_m^e(\theta) = G_o(\theta)[1 - |\Gamma_m(-\theta)|^2], \tag{2.17}$$

where $G_o = 4\pi f^2(\theta)/\eta_0$. If the array was infinitively large or had a large number of elements, where the center one is considered, a symmetric condition is established and $\Gamma_m(-\theta)$ can be replaced by $\Gamma(\theta)$ allowing Eq. 2.17 to be rewritten as

$$G_m^e(\theta) = G_o(\theta)[1 - |\Gamma(\theta)|^2]. \tag{2.18}$$

Eq. 2.18 shows the ARC and the AEP being two sides of the same coin. One can measure the AEP of an element near the center of the array and through Eq. 2.18 find the ARC. Alternatively, one can measure the S-parameters of the phased array using a network analyzer to find the ARC from Eq. 2.12 and calculate the AEP through Eq. 2.18. For the fully excited array, the magnetic fields are written in terms of currents, and combined with the electric fields from Eq. 2.7, allows the gain of the aperture to be expressed as [51]

$$G^a(\theta) = NG_m^e(\theta). \tag{2.19}$$

It can be seen from Eq. 2.19 that the radiation pattern of a fully excited array is only a function of the number of elements in the aperture and the AEP. Thus, the radiation characteristics of a phased array can only be found by finding the ARC or AEP. One important aspect of this result, is the assumption of the array having a large number of elements. As it was previously discussed, the ARC is highly dependent on the physical characteristics of the antenna that makes an array. If a linear array with a large number of elements is considered, the interactions between antennas would only occur along one dimension. Even though an ARC exists for such array, its result would not truly reflect the performance of a planar array due to truncated interactions of mutual coupling in the orthogonal dimension.

2.2.3 Planar Phased Arrays

The radiation characteristics of a planar array are obtained by expanding the familiar linear array into two dimensions and making appropriate allocation of the space factor for each antenna element. From [47], [53], the two-dimensional (2D) active reflection coefficient for the "*mn*th" element in an array on the *xy*-plane is given by

$$\Gamma_{m,n}(\theta,\phi)=\sum_{P=-p}^{P}\sum_{Q=-q}^{Q}S_{mn,pq}\;e^{-j(p-m)u}e^{-j(q-n)v}, \tag{2.20}$$

where θ is the angle made from the z-axis to the xy-plane, ϕ the angle made from the x- to the y-axis, u the space factor along the x-axis given by $kd_x\sin\theta\cos\phi$, v the space factor along the y-axis given by $kd_y\sin\theta\sin\phi$, and p,q refers to the physical position of the elements on the array. For the radiation characteristics of the planar array, the 2D AEP as a function of the ARC is given by

$$G^{e}(\theta,\phi)=\frac{4\pi ab}{\lambda^2}[1-|\Gamma(\theta,\phi)|^2]\cos\theta, \tag{2.21}$$

with a and b corresponding to the width and the length of the antenna unit cell. Lastly, the active aperture pattern (AAP) is given by

$$G^{a}(\theta,\phi)=NG^{e}(\theta,\phi). \tag{2.22}$$

Although no mention on how to characterize dual-polarized antennas has been made, work from [54] show that low coupling between horizontal and vertical channels has little influence in the estimation of the ARC. For this

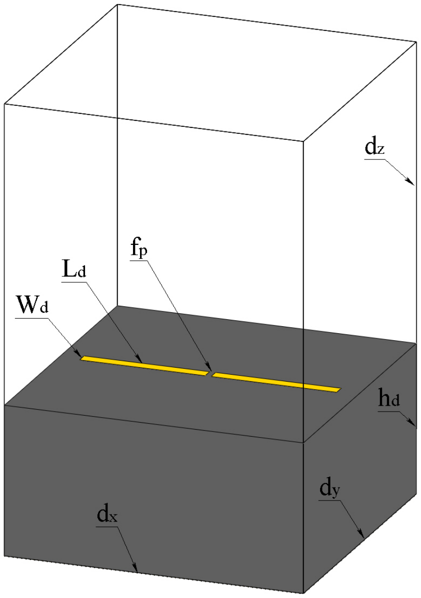

Figure 2.4: Printed dipole antenna unit cell using periodic boundary conditions and floquet port excitations in HFSS. The dimensions of the antenna are as follows: unit cell size $d_x = d_y = 50$ mm, extension of unit cell from the top face of the dielectric $d_z = 50$ mm, dipole width $W_d = 2$ mm, dipole length $L_d = 42$ mm, and dielectric height $h_d = 25$ mm with $\epsilon_r = 2.2$. A lumped port with an impedance of 73 + j42.5 Ω was used between the two dipole arms.

reason, the H- and V-channels of dual-polarized phased array antennas designed in this work are characterized independently from one another. In Section 2.3, an antenna element is analyzed using Ansys HFSS [55] to show a variety of antenna metrics including: realized gain, bandwidth, mutual coupling, ARC, and AEP. The analysis shows that Eqs. 2.20 - 2.22 are not necessarily accurate when characterizing finite arrays from infinite array simulations. The analysis also serves as a guide for presenting the results of the antenna elements designed and shown in chapters 4 and 5.

2.3 Phased Array Antenna Modeling

Infinite and finite array designs are simulated here using a full wave electromagnetic solver called High-Frequency Structure Simulator (HFSS, a product from Ansys)[55]. HFSS uses floquet port analysis as its basis for modeling infinite arrays, which allows for the direct calculation of the AEP and the ARC of an antenna unit cell. HFSS also provides modeling guidelines for antenna unit cells on a variety of configurations. Hereinafter, all guidelines regarding unit cell size, floquet port excitations, and boundary conditions are followed for infinite and finite arrays.

2.3.1 Infinite Array Analysis

A printed dipole antenna unit cell was setup in HFSS using the geometry shown in Fig. 2.4, with the purpose of extracting its frequency response (at boresight) and scanning capabilities at center frequency (3 GHz). It can be seen in Fig. 2.5a that the antenna has a boresight ARC below -10 dB (or 0.3162 in linear scale) across 296 MHz. This threshold (ARC $\leq$ -10 dB) is usually referred in the literature as the bandwidth (BW) of the antenna, and in this case, the printed dipole exhibits a BW of 296 MHz or fractional bandwidth of 10% (i.e., $BW/(f_{max} - f_{low})/2$). The boresight realized gain can be calculated using the ARC shown in Fig. 2.5a in combination with Eq. 2.21, for $\theta = \theta_o = 0°$. Fig. 2.5b shows the boresight realized gain for the printed dipole compared to the theoretical gain of an antenna with the same unit cell dimensions. The theoretical gain has a positive slope across frequency and is always greater than the realized gain. This result will hold true for any antenna on a planar configuration (i.e., theoretical $>$ realized gain).

Moving over to scanning capabilities, Fig. 2.5c shows the ARC for the

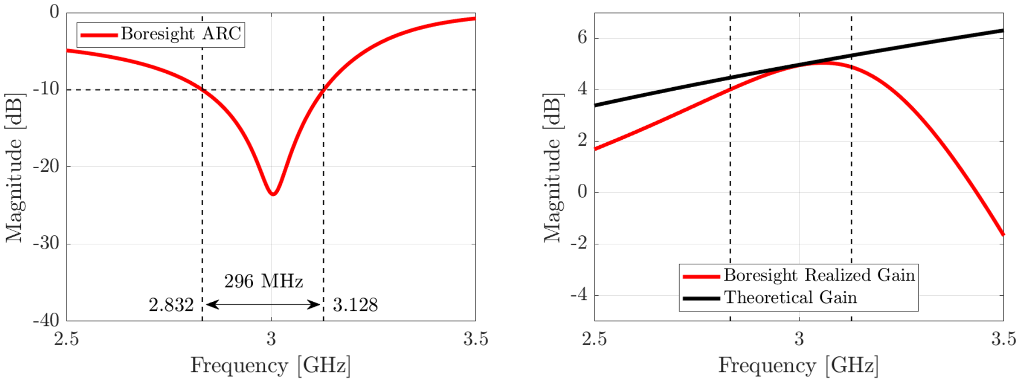

(a) ARC at Boresight

(b) Realized Gain at Boresight

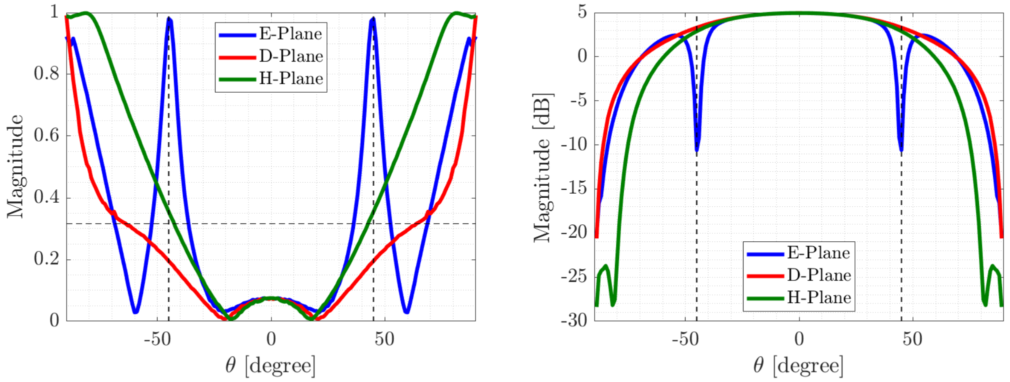

(c) ARC Cuts

(d) AEP Cuts

Figure 2.5: Characterization of an infinite array made out of printed dipole antennas using the unit cell shown in Fig. 2.4. a) Active reflection coefficient at boresight. b) Theoretical and realized gain at boresight. c) Active reflection coefficient cuts for *E*-, *D*-, and *H*-plane. b) Active element pattern cuts for *E*-, *D*-, and *H*-plane.

printed dipole as it is scanned along the E- (along the antenna polarization cut), D- (between the polarization and the orthogonal cut), and H-plane (orthogonal to the antenna polarization cut) in linear scale at 3 GHz. It is evident that the antenna can sustain an ARC below 0.3162 (or $\leq$ -10 dB) for the D- as well as most of the H-plane. However, as the antenna is scanned in the E-plane, it exhibits an ARC of 1 near $\pm$ 45°. This condition is known as a scan blindness and it produces a null in the radiation pattern of the antenna, as shown in Fig. 2.5d. This blindness is a byproduct of the dielectric coated ground in the printed dipole antenna through a surface wave, and it can be predicted using transcendental equations, as shown in Section 4.2. In the next section, the performance of the printed dipole antenna on an infinite array is approximated by finite array simulations.

2.3.2 Finite Array Analysis

HFSS provides the finite array Domain Decomposition Method (DDM) which reuses the antenna unit cell meshed geometry to estimate the performance of a finite array. A simulation was setup in HFSS using DDM for a finite 15 x 15 array made from printed dipoles, integrating the geometry shown in Fig. 2.4. In contrast to the infinite array, finite array simulations using DDM produce the S-parameters matrix of the array which carries the mutual coupling interactions between elements. This feature allows the user to retrieve the array performance metrics in two dimensions (i.e., for all θ and ϕ) by only meshing one geometry and using Eqs. 2.20 - 2.22. This is a significant reduction in simulation time from an infinite array, for which every pointing angle must be solved independently.

Fig. 2.6a and Fig. 2.6b shows the mutual coupling in the array using the

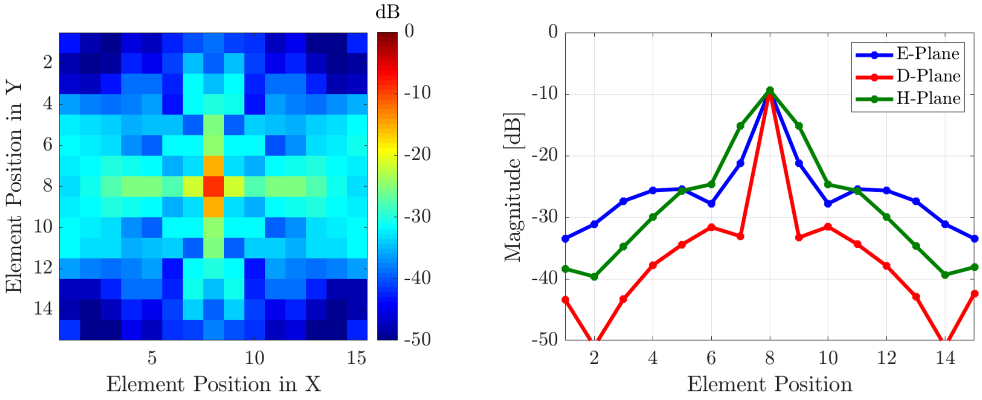

(a) 2D Mutual Coupling (b) Mutual Coupling Cuts

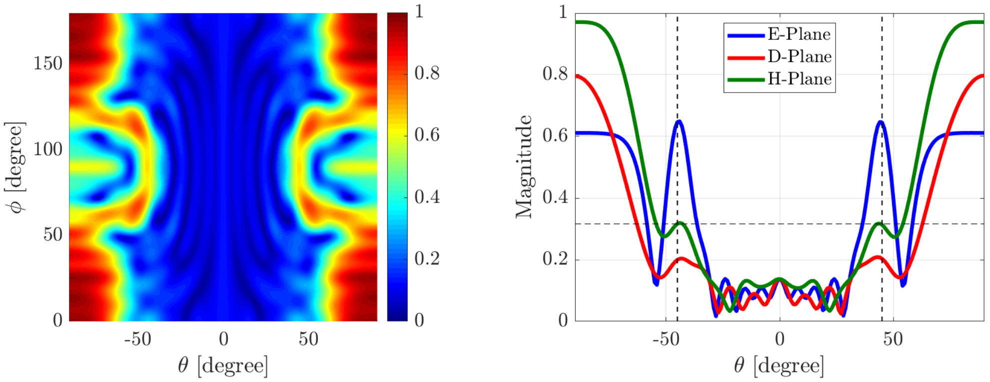

(c) 2D ARC (d) ARC Cuts

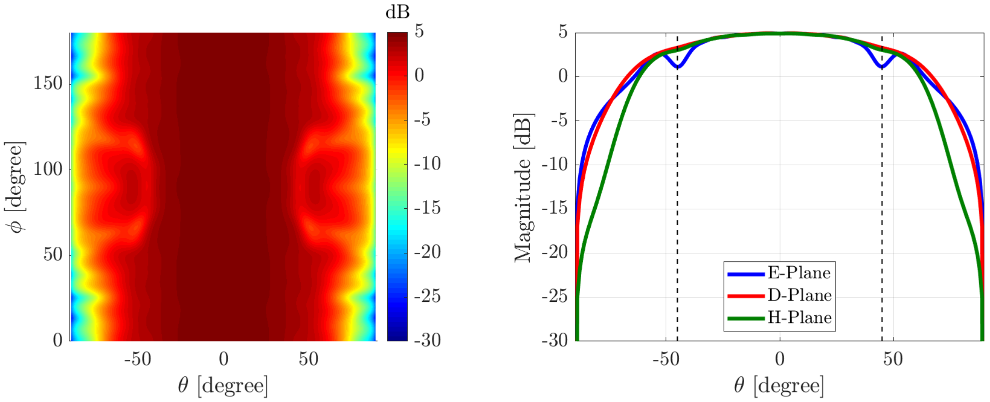

(e) 2D AEP (f) AEP Cuts

Figure 2.6: Characterization of a finite 15 x 15 printed dipole antenna array. a) Two-dimensional coupling terms with the center element as a reference. b) Mutual coupling cuts along horizontal, vertical, and diagonal cuts. c) Active reflection coefficient for the center element based on the 2D couplings. d) Active reflection coefficient cuts for the *E*-, *D*-, and *H*-plane. e) Active element pattern for the center element based on the 2D ARC. f) Active element pattern cuts for the *E*-, *D*-, and *H*-plane.

center element as a reference. It can be seen that the center element has a self-reflection close to -10 dB with consistently higher couplings in the E-plane after the third element (see Fig. 2.6b). This self-reflection is not the same as the ARC of the element, which includes the mutual coupling interactions. To estimate the ARC, the S-parameters matrix of the array is used in combination with Eq. 2.20. In Fig. 2.6c and 2.6d the ARC for the center element in the printed dipole array is shown; with passive reflections dropping from -9.35 dB (see Fig. 2.6b) to -17.24 dB (0.1374 linear, see Fig. 2.6d) at boresight, when the element is active. When compared to the infinite array, the finite array simulation fails to show scan blindness (ARC = 1) in the E-plane at angles close to $\theta = \pm\ 45°$. This result is part of the limitations of simulating or measuring finite arrays, with a small amount of elements, to try and predict the performance of an infinite array. This divergence can only be mitigated by measuring or simulating bigger finite arrays to approximate infinite array performance. Finally, the AEP for the finite array is calculated using Eq. 2.21 and the ARC results shown in Fig. 2.6c. It is now more evident from Fig. 2.6e and 2.6f that the AEP through finite array simulation shows only a 4 dB dip in radiation intensity from boresight, which does not accurately represent a theoretical scan blindness condition.

2.4 Summary

All relevant fundamentals used through this work have been discussed in this chapter. Section 2.1 discussed the differences between planar, cylindrical, and spherical phased array geometries. Additionally, we advocated that planar phased array geometries serve as efficient solutions for current and future multi-function PAR projects. In Section 2.2, planar phased array performance metrics such as ARC and AEP were described. It was proved that the ARC and the AEP are related by the same mathematical construct thus, one can be derived from the other. The aforementioned, were only defined for phased array antennas with large number of elements. It is only through these metrics that the true radiation characteristics of a planar array are predicted. Section 2.3 explored the limitations of the ARC and the AEP through infinite and finite array simulations and a strong divergence between the results was found. It was stated that this divergence can be mitigated by measuring or simulating bigger finite arrays. In chapter 3, design trade-offs for planar phased array antennas are discussed, with special emphasis on different elements and their performance.

Chapter 3

Planar Phased Array Antenna Design Trade-offs

There are many factors to consider when designing a phased array such as bandwidth, scanning range, and radiation patterns but, as it was proved in chapter 2, the phased array performance is mainly dictated by the antenna element that makes the array. Hence, this chapter focuses in understanding the characteristics of typical antenna elements used today in planar phased arrays. These characteristics are analyzed through the co- and cross-polarized radiation patterns which can influence phased array calibration and have a direct link to polarimetric weather requirements of the antenna. Section 3.1 covers antenna polarization fundamentals including Ludwig definitions of polarization, weather radar polarization, and the intrinsic cross-polarization. Section 3.2 discusses phased array antenna calibration and how it relates to intrinsic cross-polarization. Sections 3.3 through 3.5 estimates the radiation characteristics of wire, aperture, and microstrip patch antennas using formulations based on electromagnetic theory and simulating tools (i.e., HFSS).

3.1 Antenna Polarization

Antenna polarization refers to the curve traced by the instantaneous electric field radiated by the antenna in a plane perpendicular to the radial direction [28]. The orientation of these fields depend on a coordinate system where the antenna polarization is evaluated [56]. For this reason, there has been some controversy regarding antenna polarization definitions and the appropriate coordinate system to perform weather measurements. The widely accepted definitions of polarization used for describing radiated fields orientation in antennas are discussed in the following section.

3.1.1 Ludwig Definitions of Polarization

Ludwig [57] defines three definitions of polarization for antenna measurements based on different coordinate systems: *L1 or first* - two unit vectors in a rectangular coordinate system; *L2 or second* - spherical unit vectors tangential to a spherical surface, and *L3 or third* - co- and cross-polarization as "what one measures when antenna patterns are taken in the usual manner," with their geometries shown in Fig. 3.1. In most antenna applications, the first definition of polarization leads to innacuracies, because the radiated fields of an antenna in the far-field region are tangential to the surface of sphere, when the antenna is located at its center. Ludwig's second definition of polarization or L2-I is defined for a y-polarized infinitesimal electric dipole where co- and cross-polarization patterns are given by,

$$u_{co}^{L2-I} = \frac{E_\theta \cos\theta \sin\phi + E_\phi \cos\phi}{\sqrt{1 - \sin^2\theta \sin^2\phi}}, \tag{3.1}$$

and

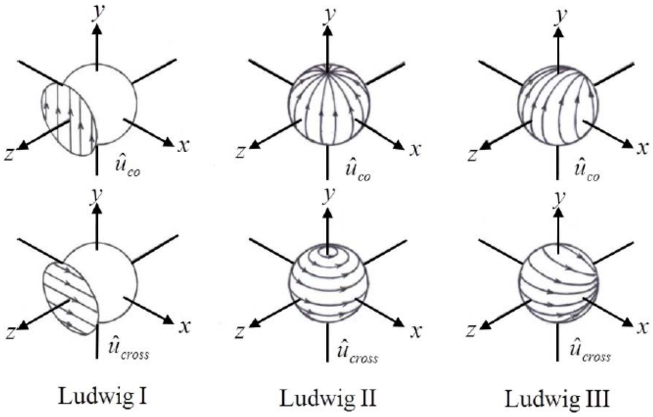

Figure 3.1: Definitions of co-polarization and cross-polarization for the three definitions of Ludwig [57]. Reprinted from [56] © 2018 IEEE.

$$u_{cross}^{L2-I} = \frac{E_\theta \cos\phi - E_\phi \cos\theta \sin\phi}{\sqrt{1 - \sin^2\theta \sin^2\phi}}, \tag{3.2}$$

where θ defines the angle from the z-axis to the xy-plane, ϕ the angle from the x- to y-axis, E_θ the electric field component along the $\hat{\theta}$ direction, and E_ϕ the electric field component along the $\hat{\phi}$ direction. The coordinate system associated with this definition is Azimuth/Elevation (AZ/EL) and its components are given by [58],

$$AZ = \tan^{-1}(\cos\phi \tan\theta) \tag{3.3}$$

and

$$EL = \sin^{-1}(\sin\theta \sin\phi). \tag{3.4}$$

An extension on Ludwig's second definition of polarization is L2-II, as shown in [56]. L2-II considers an x-polarized infinitesimal electric dipole with co- and cross-polarization defined as,

$$u_{co}^{L2-II} = \frac{E_\theta \cos\theta \cos\phi - E_\phi \sin\phi}{\sqrt{1-\sin^2\theta\cos^2\phi}}, \tag{3.5}$$

and

$$u_{cross}^{L2-II} = \frac{E_\theta \sin\phi + E_\phi \cos\theta \cos\phi}{\sqrt{1-\sin^2\theta\cos^2\phi}}. \tag{3.6}$$

The coordinate system associated with L2-II is Elevation/Azimuth (EL/AZ) and its components are given by [58],

$$AZ = \sin^{-1}(\sin\theta\cos\phi) \tag{3.7}$$

and

$$EL = \sin^{-1}\left(\frac{\sin\theta\sin\phi}{\cos AZ}\right). \tag{3.8}$$

The previous equations for co- and cross-polarization in Ludwig's 2-I and 2-II show that the radiation components from these dipoles are not orthogonal with each other. In fact, the dot product operation of the co- and cross-polarization unit vectors (neglecting sign changes) leads to,

$$\hat{u}^{L2-I} \cdot \hat{u}^{L2-II} = \frac{\cos\phi\sin\phi\sin^2\theta}{\sqrt{\cos^2\theta + 0.25\sin^4\theta\sin^2 2\phi}}. \tag{3.9}$$

This non-orthogonality condition suggests that the radiation patterns for each dipole are different and not simple 90° rotated copies of one another. To better illustrate this result refer to Fig. 3.2. It can be seen that for the coordinate system AZ/EL, the y-polarized dipole in L2-I produces co-polarized radiation nulls in EL $= \pm 90°$ with no cross-polarization (see Fig. 3.2a and 3.2b). In the other hand, L2-II requires a different coordinate system (i.e., EL/AZ) to produce the expected radiation nulls of the dipole at AZ $= \pm 90°$ with no cross-polarized radiation (see Fig. 3.2c and 3.2d). It is now evident that the polarization definitions L2-I and L2-II are not equal and they describe two non-orthogonal polarization bases. In contrast to L2-I and L2-II, Ludwig's third definition of polarization allows for interchanging the co- and cross polarization patterns by rotating the antenna 90° using the spherical coordinate system Theta/Phi (θ/ϕ).

Ludwig's third definition of polarization is defined using two antennas at far-field: an antenna under test (AUT) and a measuring single-polarized probe. For E- and H-plane, the aligned polarizations would yield the same results for co- and cross-polarization found in either L2-I or L2-II. However, as the AUT is rotated outside of the principal planes, angular dependencies are introduced in the measurement making the probe sample cuts that are non-constant over the radiation sphere of the AUT. Fig. 3.3 shows the co- and cross-polarization radiation patterns for infinitesimal electric dipoles polarized in x- and y-axis using L3. It can be seen that the co- and cross-polarization components are equal regardless of the dipole's orientation using the spherical coordinate system θ/ϕ. Ludwig's third definition of polarization produces cross-polarization for the infinitesimal electric dipoles when compared to L2-I or L2-II. This presents the question, which polarization basis and coordinate system should be used for polarimetric weather radars?

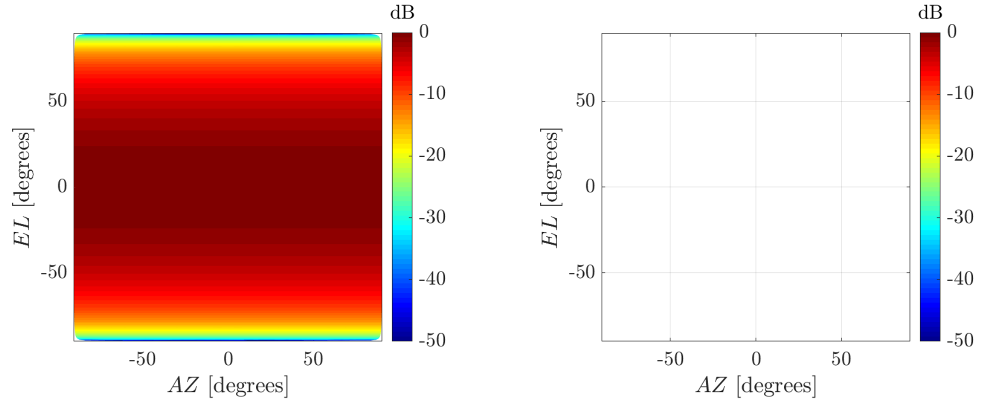

(a) Co-polarization L2-I

(b) Cross-polarization L2-I

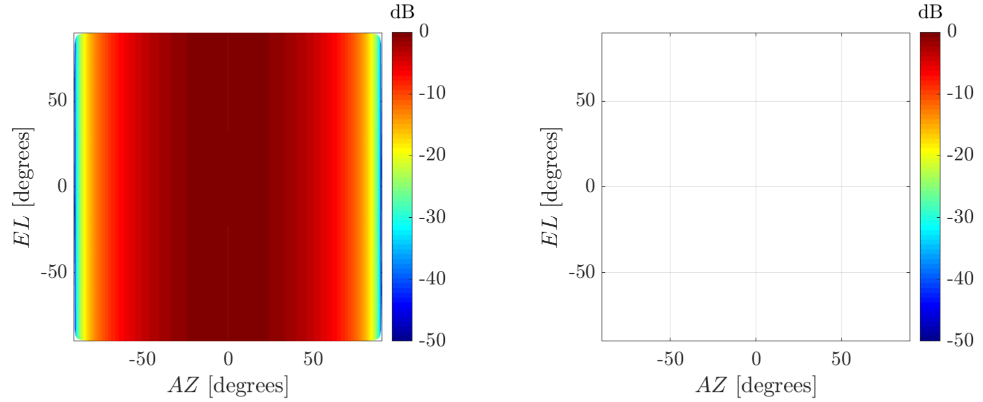

(c) Co-polarization L2-II

(d) Cross-polarization L2-II

Figure 3.2: Co- and cross-polarization radiation patterns based on Ludwig's second definitions for infinitesimal electric dipole antennas. a) Co-polarized radiation pattern for a y-polarized dipole. b) Cross-polarized radiation pattern for a y-polarized dipole. c) Co-polarized radiation pattern for an x-polarized dipole. d) Cross-polarized radiation pattern for an x-polarized dipole.

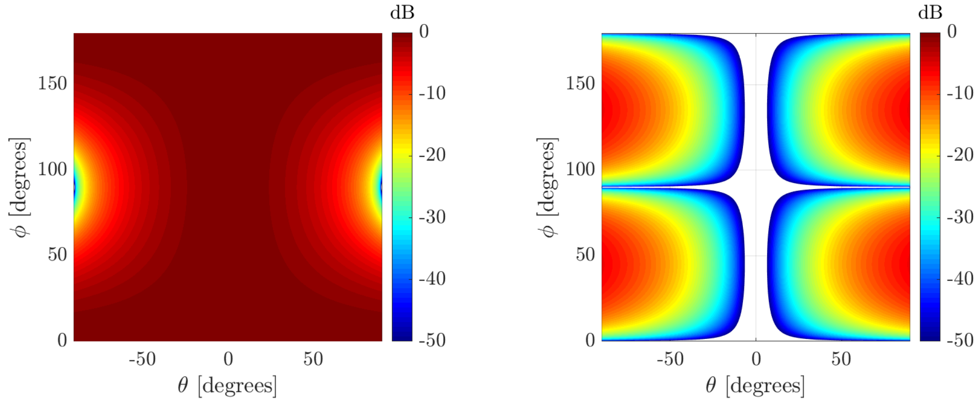

(a) Co-polarization L3-Y

(b) Cross-polarization L3-Y

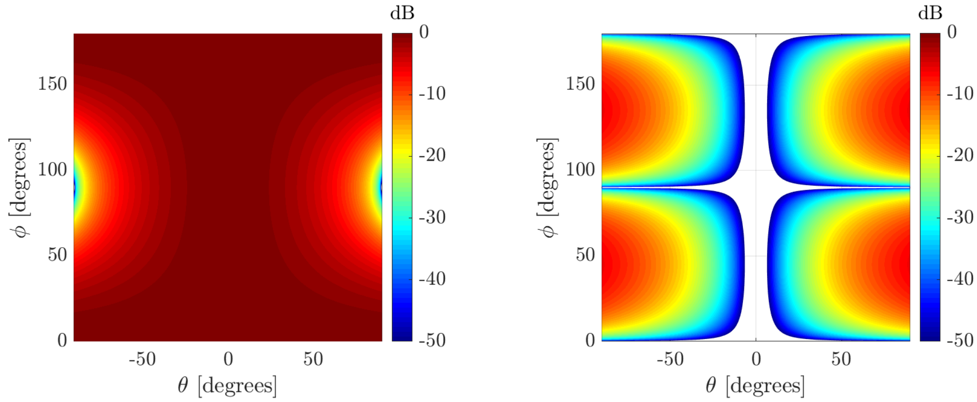

(c) Co-polarization L3-X

(d) Cross-polarization L3-X

Figure 3.3: Co- and cross-polarization radiation patterns based on Ludwig's third definition for an infinitesimal electric dipole antenna. a) Co-polarized radiation pattern for a y-polarized dipole. b) Cross-polarized radiation pattern for a y-polarized dipole. c) Co-polarized radiation pattern for an x-polarized dipole. d) Cross-polarized radiation pattern for an x-polarized dipole.

3.1.2 Polarization of Weather Radars

Traditional weather polarimetry directly correlates the radar polarimetric measurements with hydrometeor properties such as size and canting angle [59]. This results in the antenna having H-polarization lying in a plane parallel to the surface of the Earth and V-polarization approximately perpendicular to the aforementioned plane [60]. In this configuration (i.e., H/V), traditional weather polarimetry follows the coordinate system defined by Ludwig's second definition of polarization, more specifically, L2-I. The result of using this polarization basis is the presence of undesirable measurement biases that can be much larger than the intrinsic values of the measured polarimetric variables [60]. These biases then need to be removed by simulateusly adjusting the amplitude and phase of the dual-polarized elements in the array [49]. To overcome these issues, some authors have proposed the use of Ludwig's third definition of polarization for weather measurements [61]. Weather measurements using L3 would allow for better co-planar beam matching and lower biases due to cross-polarization. Another benefit that stems from L3 as polarization basis for weather measurements is that each polarization can be synthesized individually, which would make polarized beam synthesizing process easier and more flexible [61]. It does not mean that there is no biases introduced using L3 instead of L2, but it brings up a fundamental question: which polarization definition is more suited for weather measurements? This question is not answered here because there is not enough evidence in the literature to justify one or the other. However, in this work we propose the use of intrisic cross-polarization to characterize dual-polarized antennas for polarimetric weather radars.

3.1.3 Intrinsic Cross Polarization

The intrinsic cross-polarization (IXR) is a figure of merit (FoM) that does not rely in a coordinate system to characterize co- and cross-polarization in dual-polarized antennas [18]. The IXR quantifies the total relative error of a fully calibrated dual-polarized antenna in the presence of system noise and channel cross-coupling. Mathematically, IXR is defined as,

$$IXR = \left(\frac{\kappa(\mathbf{J}) + 1}{\kappa(\mathbf{J}) - 1} \right)^2 \tag{3.10}$$

where $\kappa(\mathbf{J})$ refers to the spectral condition number [62] of the Jones matrix. The Jones matrix is part of the transfer function that relates the incident fields of arbitrary polarization (i.e., E_u and E_v) to the output voltages (i.e., v_1 and v_2) in a dual-polarized receiver and it is expressed as,

$$\begin{bmatrix} v_1 \\ v_2 \end{bmatrix} = \begin{bmatrix} J_{11} & J_{12} \\ J_{21} & J_{22} \end{bmatrix} \begin{bmatrix} E_u \\ E_v \end{bmatrix}. \tag{3.11}$$

To better illustrate IXR as a FoM for dual-polarized antennas, let us consider the examples of the infinitesimal electric dipoles shown in Figs. 3.2 and 3.3. It is clear that the cross-polarization levels between L2-I or L2-II compared to L3 differ significantly from one another because they are defined for different coordinate systems (i.e., L2-I and L2-II uses AZ/EL and EL/AZ while L3 - θ/ϕ). Fig. 3.3 also shows that the y-polarized dipole produces no cross-polarization based on L2-I polarization which introduces no bias (i.e., cross-polarization bias) if used for polarimetric weather measurements in AZ/EL. In the other hand, on L3, the dipole produces cross-polarization with a maximum of -16.68 dB in the *D*-plane (i.e., $\theta = \phi = \pm\ 45°$) which translates to some cross-polarization bias in measurements. Now, lets examine a dual-polarized infinitesimal electric dipole antenna located in the xy-plane using IXR.

By substituying J_{11} as the co-polarized component of radiation for the x-polarized infinitesimal electric dipole in L2-I or L3, and J_{21} as the cross-polarized component, leaves J_{12} and J_{22} as the cross- and co-polarized components of radiation for the y-polarized infinitesimal electric dipole. Fig. 3.4 shows the IXR for a dual-polarized infinitesimal electric dipole using the coordinate systems AZ/EL and θ/ϕ and polarization definitions L2-I and L3. In this case, the IXR is equal for both definitions regardless of the reference coordinate system. Even though not shown here, these results extend to L2-II polarization or any other pair of fields defined in an orthogonal basis. For scanning positions near boresight, the IXR takes values higher than 50 dB. This result suggests a higher level of orthogonality between the channels of the dual-polarized dipole antenna with similar co-polarized fields magnitudes. As the antenna is scanned out of boresight, these characteristics are lost (i.e., co-polarized field magnitudes diverge and cross-polarization increases). Notice that IXR is not meant to describe cross-polarization, but rather to measure the leakage out of all possible configurations of the aligned antenna. Thus, an antenna can exhibit cross-polarization levels below -40 dB while simulateneously have worse IXRs (e.g., *E*- and *H*-plane). In this case, the IXR identifies differences between the co-polarized fields in H- and V-polarizations which results on ill-conditioned Jones matrices. However, the main justification for using IXR as a FoM to characterize polarimetric phased array weather antennas its the direct relation between the condition number of the Jones matrix and the relative errors in the final, calibrated polarimetric measurement.

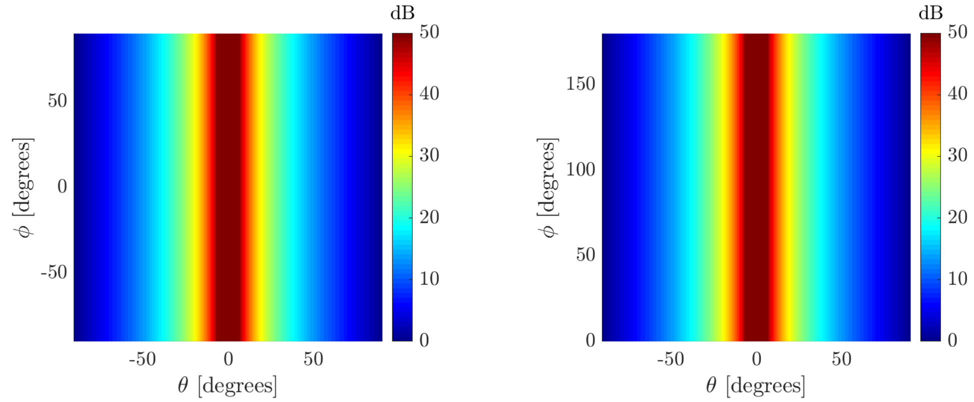

(a) IXR L2-I θ/ϕ (b) IXR L3 θ/ϕ

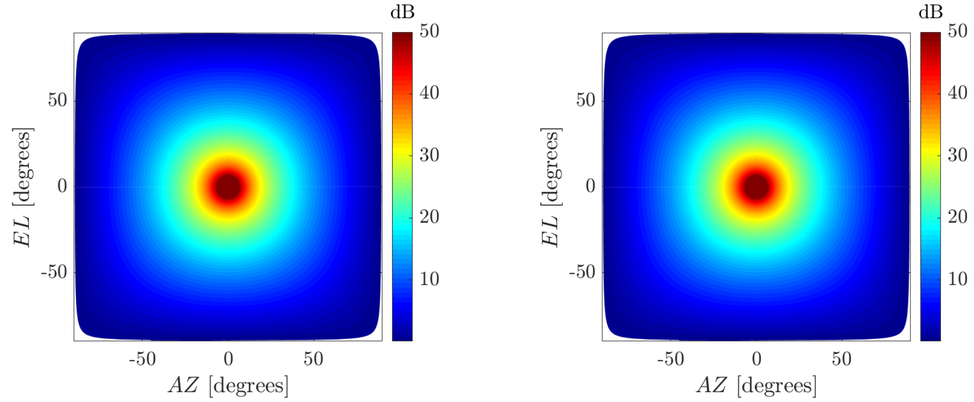

(c) IXR L2-I AZ/EL (d) IXR L3 AZ/EL

Figure 3.4: Intrinsic cross-polarization (IXR) for a dual-polarized infinitesimal electric dipole antenna. a) IXR using co- and cross-polarization based on L2-I using θ/ϕ as the coordinate system. b) IXR using co- and cross-polarization based on L3 using θ/ϕ as the coordinate system. c) IXR using co- and cross-polarization based on L2-I using AZ/EL as the coordinate system. b) IXR using co- and cross-polarization based on L3 using AZ/EL as a coordinate system.

3.2 Phased Array Antenna Calibration

It has been proved so far that co- and cross-polarization patterns are highly dependant on coordinate systems. This dependency makes antenna engineers focus on designing radiating elements with low cross-polarization for different coordinate systems, disregarding the effects that the coordinate system has on cross-polarization. Phased array calibration in the context of this work is the procedure in which cross-polarization biases are removed by simulateously changing the excitations on the antenna. It also refers to the beam matching procedure that takes place when the antenna is scanned out of boresight. Currently, this type of phased array antenna calibration is performed assuming a polarization basis. Here we propose the use of IXR to characterize the performance of polarimetric phased array weather antennas. The IXR relates to the total relative error in a fully calibrated phased array antenna in the presence of system noise and channel cross-coupling. These errors are found from [18],

$$\frac{\|\Delta \mathbf{e}\|}{\|\mathbf{e}\|} \lessapprox \left(1 + \frac{2}{\sqrt{IXR}} + \dots\right)\left(\frac{\|\Delta \mathbf{J}\|}{\|\mathbf{J}\|} + \frac{\|\Delta \mathbf{f}\|}{\|\mathbf{f}\|}\right), \tag{3.12}$$

where $\|\Delta \mathbf{J}\|/\|\mathbf{J}\|$ refers to the total relative error introduced in the calibration through the Jones matrix, $\|\Delta \mathbf{f}\|/\|\mathbf{f}\|$ to the reciprocal of the signal-to-noise ration (SNR), and $\|\Delta \mathbf{e}\|/\|\mathbf{e}\|$ to the error found in the measured fields. To understand the significance of this result, let us consider dual-polarized antennas with IXRs of 10, 20, 30, and 40 dB with fixed $\|\Delta \mathbf{J}\|/\|\mathbf{J}\|$ and $\|\Delta \mathbf{f}\|/\|\mathbf{f}\|$. In these examples, the IXR magnifies the errors by $2/\sqrt{IXR}$, which corresponds to an error amplification of 63%, 20%, 6.3%, and 2%. Thus, higher values of IXR are more desirable for dual-polarized antennas which ultimately refers to better antenna calibratability [63]. In the next sections we'll explore different antennas used traditionally in phased arrays with the goal of finding the lowest cross-polarization elements with the highest IXRs.

3.3 Polarization in Wire Antennas

Hereinafter, the electric fields of wire antennas are found using a current distribution polarized in the y-axis and operating at 3 GHz. It is assumed that the antennas are center-fed with current vanishing at the end points of the wires [28]. A coordinate system transformation [64] is used to calculate the x-polarized electric field components from the theoretically derived y-polarized expressions. Predicted co- and cross-polarization radiation patterns using L3 polarization are shown and HFSS simulations are used to validate these results. Lastly, the IXR is calculated using the derived y-polarized field expressions and the x-polarized components calculated through the coordinate system transformation.

3.3.1 Dipole Antenna in Free Space

Fig. 3.5 shows the infinitesimal wire dipole antenna geometry with electric fields E_θ and E_ϕ given by [28],

$$E_\theta = \frac{-j\omega\mu_0 I_0 l e^{-jk_0 r}}{4\pi r}\cos\theta\sin\phi, \tag{3.13}$$

and

$$E_\phi = \frac{-j\omega\mu_0 I_0 l e^{-jk_0 r}}{4\pi r}\cos\phi. \tag{3.14}$$

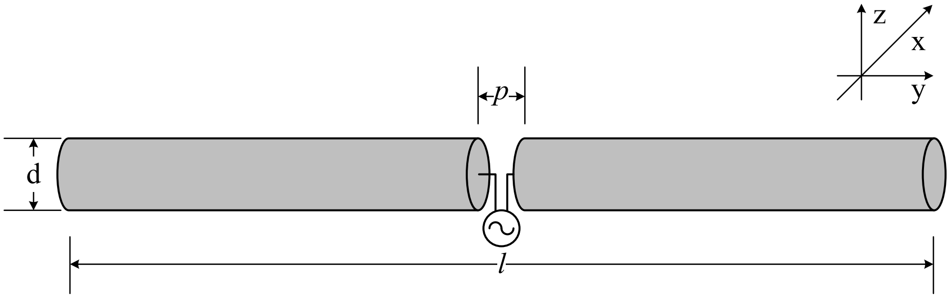

Figure 3.5: Wire dipole antenna geometry used for modeling and simulations where d = 10 mils is the dipole arms diamater, l = 50 mm its full length, and p = 1 mm the lumped port excitation length with Z_o = 73 + j42.5 Ω.

The co- and cross-polarization components using L3 polarization definition are calculated using the spherical coordinate system defined by $-180° \leq \theta \leq 180°$ and $0° \leq \phi \leq 180°$ assuming $-j\omega\mu_0 I_0 l e^{-jk_0 r}/4\pi r$ as a constant. These results are shown in Fig. 3.6. The only difference between Figs. 3.6a and 3.6b to the results shown in Fig. 3.2 is the extension of the radiation sphere below the the xy-plane. This extension shows cross-polarization levels equal to the co-polarization in z-axis direction (i.e., $\theta = 180°$), evidently presented for theoretical and simulated results in Fig. 3.6c. In the same direction, the calculated IXR shown in Fig. 3.6d is in the excess of 50 dB. These results present the complexity when analyzing IXR. In this example, the dipole produces high cross-polarization in the $\theta = 180°$ which in theory is bad for polarimetric measurements. However, this high cross-polarization is accompanied by a high IXR indicating that the dipole has the potential of receiving signals from that direction with great isolation if the excitations of the receiver are properly tuned.

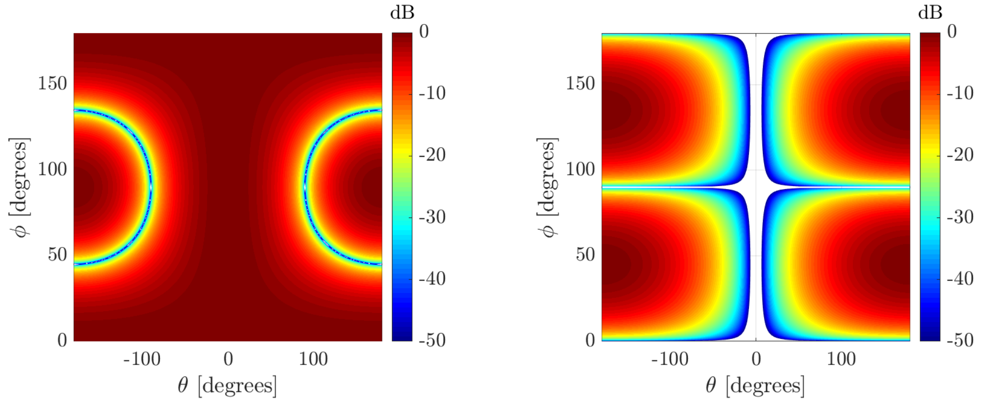

(a) Co-polarization (b) Cross-polarization

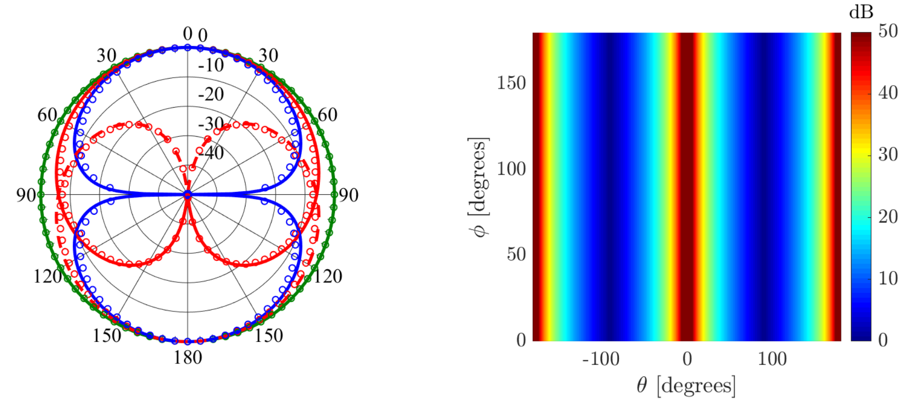

(c) Co- and Cross-polarization Cuts (d) Intrinsic Cross-polarization

Figure 3.6: Radiation characteristics for a wire dipole antenna based on Ludwig's third definition of polarization. a,b) Modeled co- and cross-polarized radiation patterns. c) Modeled (solid lines) and simulated (circle) co- and cross-polarized radiation patterns cuts for E-(blue), D-(red), and H-plane (green). d) Modeled IXR for a dual-polarized wire dipole antenna.

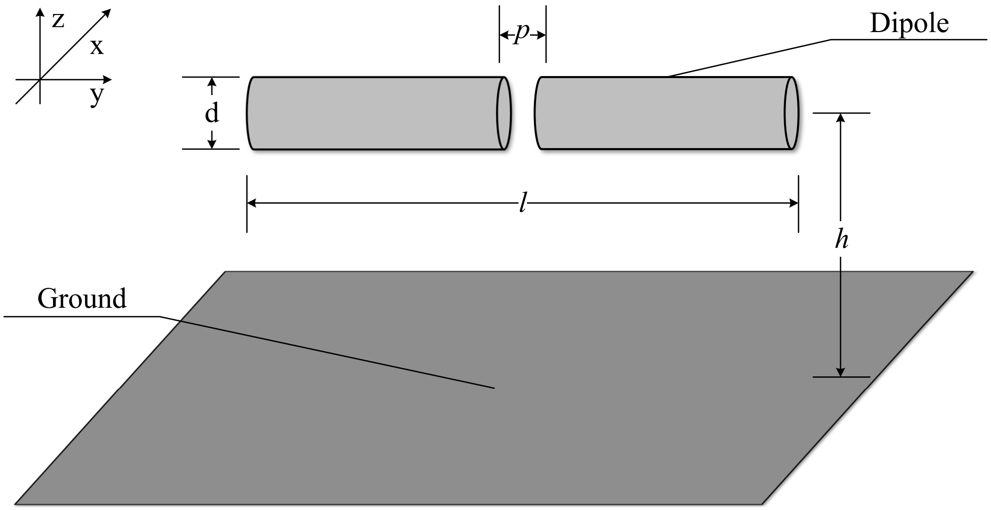

Figure 3.7: Horizontal wire dipole antenna geometry used for modeling and simulations where $d = 0.5$ mils is the dipole arms diameter, $l \approx 50$ mm its full length, $h \approx 25$ mm the distance from the infinite ground, and $p = 1$ mils the lumped port excitation length with $Z_o = 90 + \mathrm{j}75\ \Omega$.

3.3.2 Horizontal Dipole over Ground

Fig. 3.7 shows the infinitesimal horizontal wire dipole antenna over a perfect electric conductor ground that extends to infinity. The electric fields E_θ and E_ϕ are found from image theory [28] as,

$$E_\theta = \frac{-j\omega\mu_0 I_0 l e^{-jk_0 r}}{4\pi r} \cos\theta \sin\phi \ AF, \tag{3.15}$$

and

$$E_\phi = \frac{-j\omega\mu_0 I_0 l e^{-jk_0 r}}{4\pi r} \cos\phi \ AF, \tag{3.16}$$

where the “AF” term refers to the array factor or superpositioned image of the fields under the ground and its given by,

$$AF = 2j \sin(k_0 h \cos\theta). \tag{3.17}$$

The co- and cross-polarization components using L3 polarization definition are calculated using the spherical coordinate system defined by $-90^\circ \leq \theta \leq 90^\circ$ and $0^\circ \leq \phi \leq 180^\circ$ assuming $2j\omega\mu_0 I_0 l e^{-jk_0 r}/4\pi r$ as a constant. These results are shown in Fig. 3.8a, 3.8b, and 3.8c for both mathematically derived fields and simulations. In contrast to the wire dipole in free space, the horizontal dipole over ground has radiation fields defined only for z > 0. Even though the co- and cross-polarization are different between the antennas, ultimately they produce the same IXR, as shown in 3.8d. This result could have been predicted since $\hat{E}_\theta$ and $\hat{E}_\phi$ define an orthogonal basis that would make the AF term shown in Eq. 3.17 a constant in the IXR calculation using E_θ and E_ϕ components. Nevertheless, these antennas produce a minimum IXR of 15.3 dB within $-45^\circ \leq \theta \leq 45^\circ$.

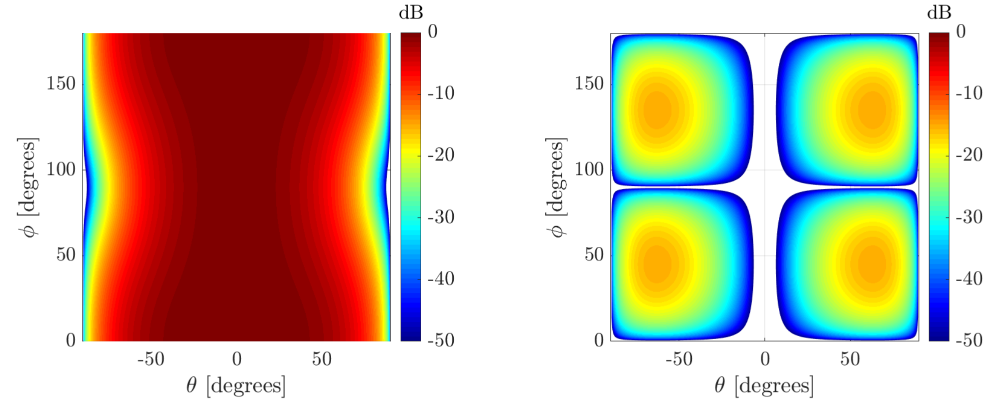

(a) Co-polarization

(b) Cross-polarization

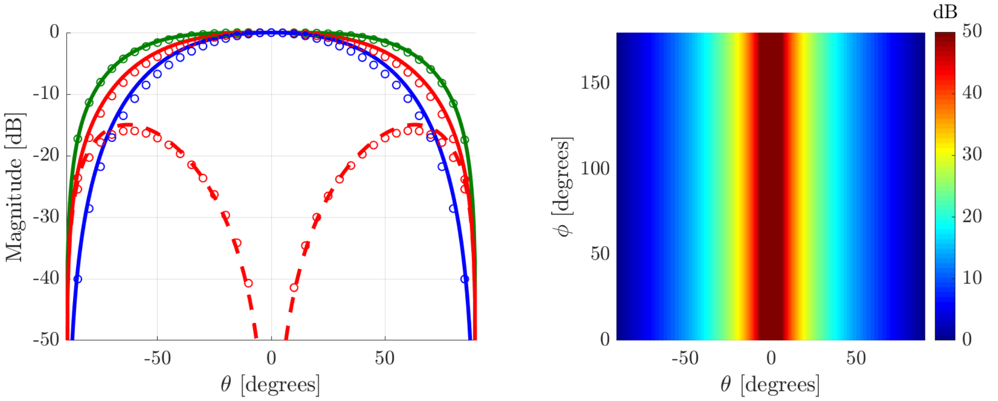

(c) Co- and Cross-polarization Cuts

(d) Intrinsic Cross-polarization

Figure 3.8: Radiation characteristics for a horizontal wire dipole over a ground based on Ludwig's third definition of polarization. a,b) Modeled co- and cross-polarized radiation patterns. c) Modeled (solid lines) and simulated (circle) co- and cross-polarized radiation patterns cuts for E-(blue), D-(red), and H-plane (green). d) Modeled IXR for a dual-polarized, horizontal wire dipole over a ground.

3.4 Polarization in Aperture Antennas

Hereinafter, the electric fields of aperture antennas are found using a equivalent current distribution polarized in the y-axis and operating at 3 GHz. It is assumed that the antennas are center-fed or have a dominant mode excitation [28]. A coordinate system transformation [64] is used to calculate the x-polarized electric field components from the theoretically derived y-polarized expressions. Predicted co- and cross-polarization radiation patterns using L3 polarization definition are shown and HFSS simulations are used to validate these results. Lastly, the IXR is calculated using the derived y-polarized field expressions and the x-polarized components calculated through the coordinate system transformation.

3.4.1 Waveguide Antenna

Fig. 3.9 shows the open-ended waveguide antenna geometry in a ground that extends to infinity with electric fields E_θ and E_ϕ given by [28],

$$E_\theta = j\frac{abkE_0e^{-jkr}}{2\pi r}\left[\sin\phi\left(\frac{\sin X}{X}\right)\left(\frac{\sin Y}{Y}\right)\right], \tag{3.18}$$

and

$$E_\phi = j\frac{abkE_0e^{-jkr}}{2\pi r}\left[\cos\theta\cos\phi\left(\frac{\sin X}{X}\right)\left(\frac{\sin Y}{Y}\right)\right], \tag{3.19}$$

where X and Y define the far-zone fields for a spherical coordinate system defined as,

$$X = \frac{ka}{2}\sin\theta\cos\phi, \tag{3.20}$$

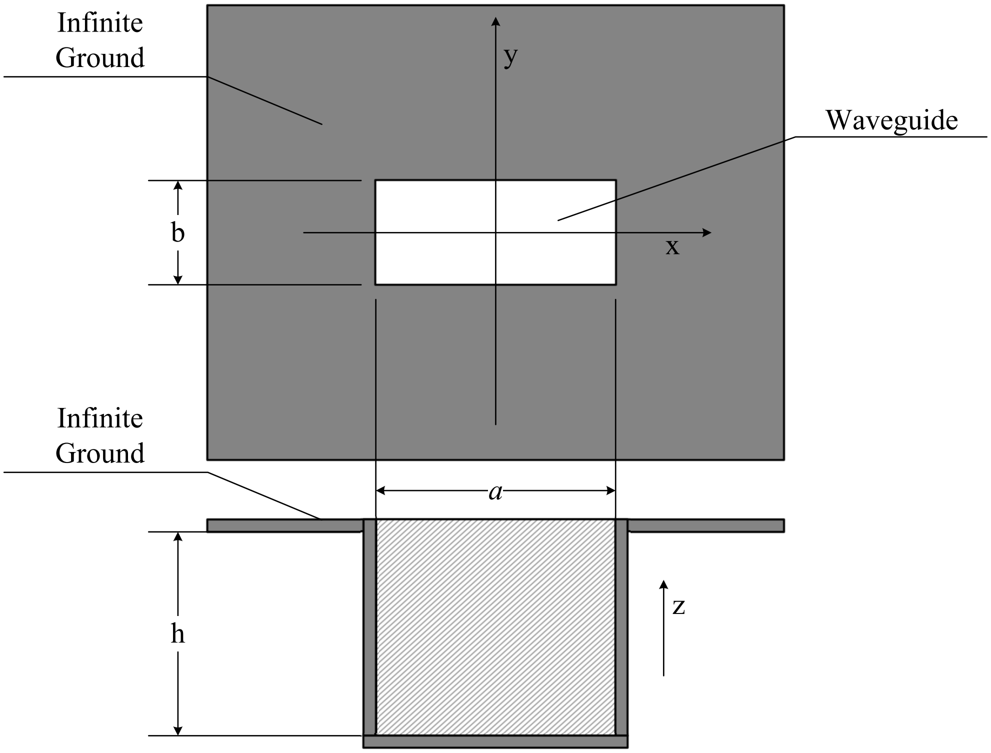

Figure 3.9: Waveguide antenna geometry used for modeling and simulations where $a = 72.136$ mm is the width of the waveguide, $b = 34.036$ mm its height, and $h = 100$ mm its length.

and

$$Y = \frac{kb}{2} \sin\theta \sin\phi. \tag{3.21}$$

The co- and cross-polarization components using L3 polarization are calculated using the spherical coordinate system defined by $-90^\circ \leq \theta \leq 90^\circ$ and $0^\circ \leq \phi \leq 180^\circ$ assuming $jabkE_0e^{-jkr}/2\pi r$ as a constant. These results are shown in Fig. 3.10a, 3.10b, and 3.10c for both mathematically derived fields and simulations. It can be seen that the waveguide produces a cross-polarization that resembles the one found in the wire dipole in free space and horizontal dipole over a ground. However, it produces highly different co-polarized radiation pattern cuts for E- and H-plane. The reason for this result is the boundary condition established for the principal planes where E-plane would only vanish if the dimension of the waveguide b was a multiple of a wavelength. Fig. 3.10d shows the hypothetical IXR calculated for a dual-polarized waveguide antenna. It is a hypothetical calculation because the design of a dual-polarized waveguide antenna in this calculation would require the overlap between H/V polarizations. Nevertheless, a hypothetical dual-polarized waveguide produces a minimum IXR of 12.2 dB within $-45^\circ \leq \theta \leq 45^\circ$.

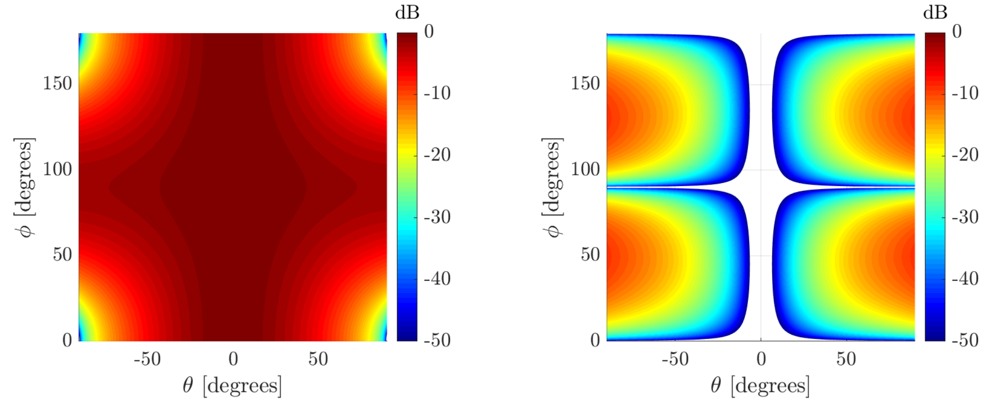

(a) Co-polarization

(b) Cross-polarization

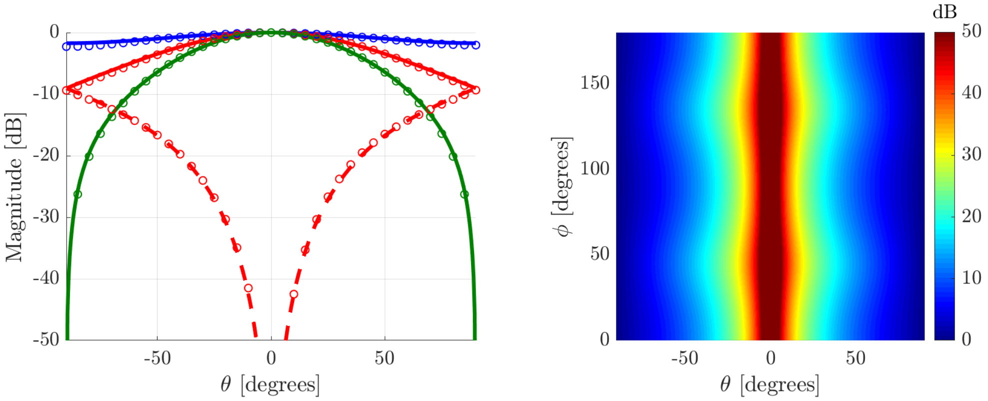

(c) Co- and Cross-polarization Cuts

(d) Intrinsic Cross-polarization

Figure 3.10: Radiation characteristics for the open-ended waveguide antenna on an infinite ground based on Ludwig's third definition of polarization. a,b) Modeled co- and cross-polarized radiation patterns. c) Modeled (solid lines) and simulated (circle) co- and cross-polarized radiation patterns cuts for *E*-(blue), *D*-(red), and *H*-plane (green). d) Modeled IXR for a hypothetical dual-polarized waveguide antenna on an infinite ground.

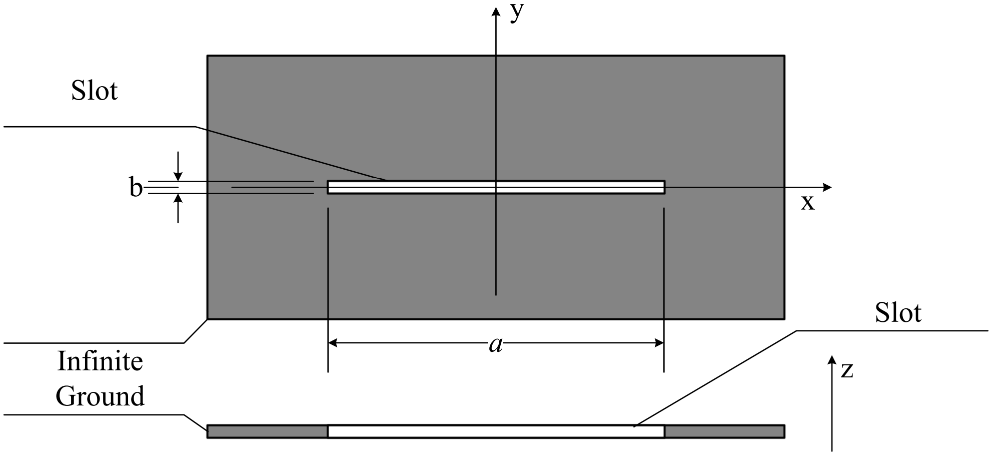

Figure 3.11: Slot antenna geometry used for modeling and simulations where a = 50 mm is the width of the slot and b = 10 mils its height. The slot is fed at the center with a lumped port that has an impendance Z_o = 362.95 - j211.31 Ω.

3.4.2 Slot Antenna

Fig. 3.11 shows the slot antenna geometry in an infinite perfect electric conductor ground plane. The slot fields are calculated using the expressions derived for the waveguide antenna. The only difference between these two calculated fields is the height of the aperture b, which for the slot is usually only fractions of its length. For simulations, the slot requires a lumped port as excitation due to its resonant nature which is different from the waveguide model that requires a waveport. Fig. 3.12a, 3.12b, and 3.12c shows the co- and cross-polarization for both mathematically derived fields and simulations. As expected, there is not a lot of difference between the polarization of the slot and the waveguide antenna. However, it is clear is that the slot exhibits a uniform E-plane with a slower roll-off in all other planes. Fig. 3.12d shows the IXR for a dual-polarized slot antenna producing a minimum of 12.8 dB within $-45° \leq \theta \leq 45°$.

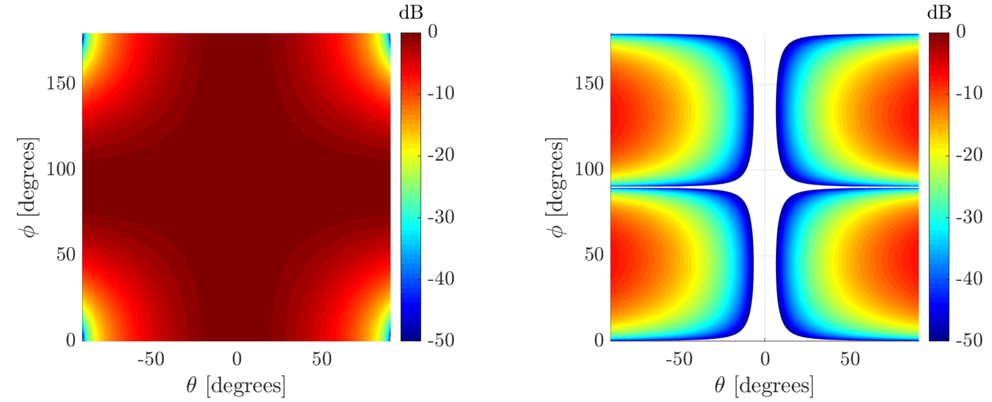

(a) Co-polarization (b) Cross-polarization

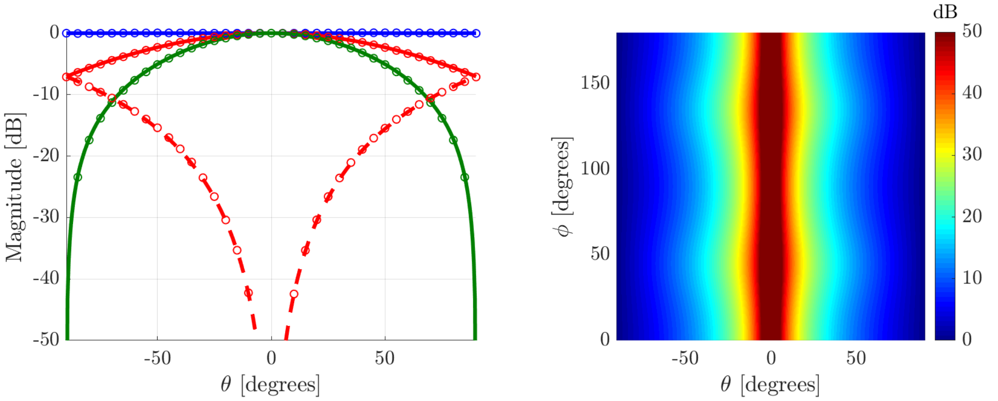

(c) Co- and Cross-polarization Cuts (d) Intrinsic Cross-polarization

Figure 3.12: Radiation characteristics for a slot antenna on an infinite perfect electric conductor ground based on Ludwig's third definition of polarization. a,b) Modeled co- and cross-polarized radiation patterns. c) Modeled (solid lines) and simulated (circle) co- and cross-polarized radiation patterns cuts for E-(blue), D-(red), and H-plane (green). d) Modeled IXR for a dual-polarized slot antenna.

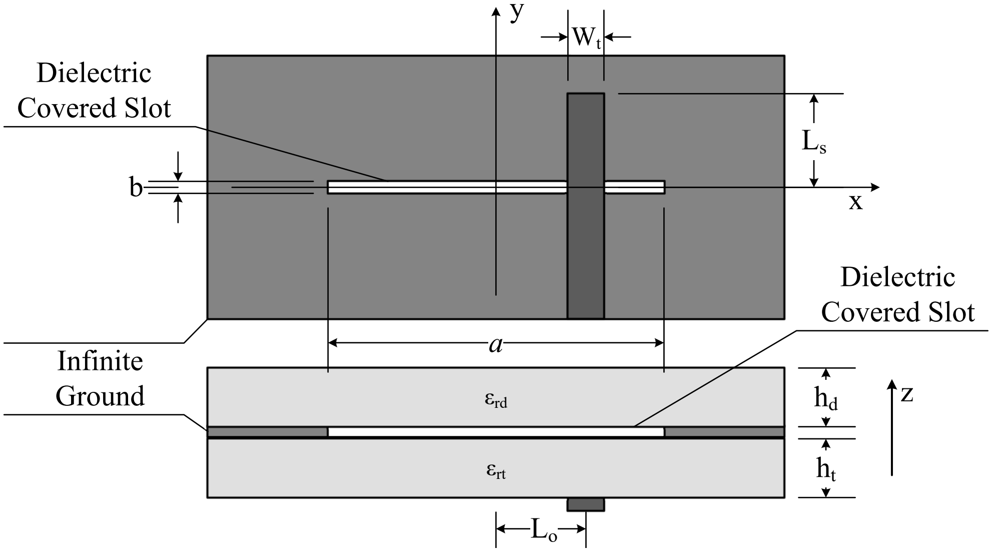

Figure 3.13: Dielectric-covered slot antenna geometry used for modeling and simulations where a and b are the width and the height of the slot. The slot is covered with a substrate that has a dielectric constant ϵ_{rd} and thickness h_d. It is fed with a 50 Ω transmission line that has a width W_t, stub length L_s, and is offset from the center by L_o. The substrate supporting the transmission line has a dielectric constant ϵ_{rt} and thickness h_t. The predicted theoretical radiation patterns and simulation model used the following dimensions: a = 50.5 mm, b = 3 mm, ϵ_{rd} = 2.2, and h_d = 60 mils, ϵ_{rt} = 3.66, h_t = 30 mils, W_t = 1.68 mm, L_s = 12 mm, and L_o = 11.22 mm.

3.4.3 Dielectric-Covered Slot Antenna

Fig. 3.13 shows the dielectric-covered slot antenna geometry which has ground plane and substrates extending to infinity. The electric fields E_θ and E_ϕ are derived through spectral techniques and are given by [28],

$$E_\theta(r,\theta,\phi) = f(\theta)E_\theta^0(r,\theta,\phi), \tag{3.22}$$

and

$$E_\phi(r,\theta,\phi) = g(\theta)E_\phi^0(r,\theta,\phi), \tag{3.23}$$

where $E_\theta^0(r,\theta,\phi)$ and $E_\phi^0(r,\theta,\phi)$ refer to the uncovered slot fields shown in Section 3.4.2. The dielectric effects in the radiation pattern are taken into account through $f(\theta)$ and $g(\theta)$ which are found from,

$$f(\theta) = \frac{e^{jk_0 h \cos\theta}}{\cos\psi + jZ_h \sin\psi}, \tag{3.24}$$

and

$$g(\theta) = \frac{e^{jk_0 h \cos\theta}}{\cos\psi + jZ_e \sin\psi}, \tag{3.25}$$

where ψ, Z_e, and Z_h refers to the surface impedance or spatial ground reflection coefficient contributions given by,

$$\psi = k_0 h \sqrt{\epsilon_r - \sin^2\theta}, \tag{3.26}$$

$$Z_e = \frac{\cos\theta}{\sqrt{\epsilon_r - \sin^2\theta}}, \tag{3.27}$$

and

$$Z_h = \frac{\sqrt{\epsilon_r - \sin^2\theta}}{\epsilon_r \cos\theta}. \tag{3.28}$$

These field expressions are limited to a slot antenna covered by one dielectric substrate alone. Thus, the radiation on the other side of the slot is not taken into account which makes the expressions only valid for $-90° \leq \theta \leq 90°$. Any kind of perturbation introduced by the TL substrate in the radiation patterns are considered in simulations. Fig. 3.14a, 3.14b, and 3.14c shows the theoretically derived and simulated co- and cross-polarization radiation patterns in L3 using the dimensions shown in Fig. 3.13. It is clear that there assymetries between the simulated and theoretically derived co-polarized radiation patterns. These assymetries are the result of exciting the slot outside of its center without a balanced feed. In contrast to the uncovered slot antenna, the E-plane radiation cut of the dielectric-covered antenna shows a null at $\theta = \pm 90^\circ$ which is introduced by the surface impedance of the modified ground. Moreover, the dual-polarized dielectric-covered slot shows a mimum IXR of 11.2 dB within $-45^\circ \leq \theta \leq 45^\circ$ which reflects a reduction of 1.6 dB from the uncovered slot antenna.

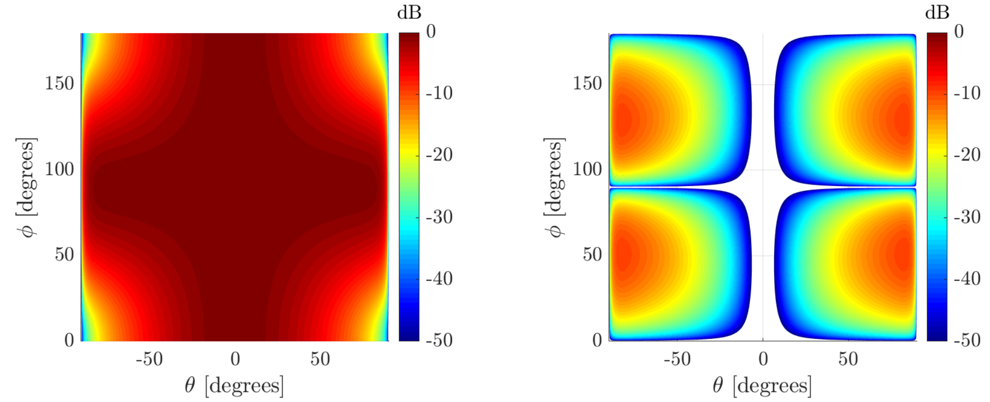

(a) Co-polarization (b) Cross-polarization

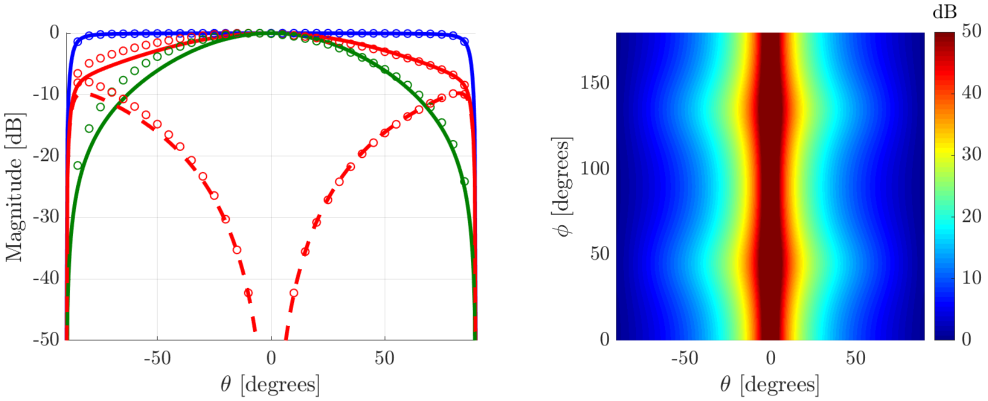

(c) Co- and Cross-polarization Cuts (d) Intrinsic Cross-polarization

Figure 3.14: Radiation characteristics for a dielectric-covered slot antenna on an infinite ground based on Ludwig's third definition of polarization. a,b) Modeled co- and cross- polarized radiation patterns. Modeled (solid lines) and simulated (circle) co- and cross-polarized radiation patterns cuts for E-(blue), D-(red), and H-plane (green). d) Modeled IXR for a dual-polarized dielectric-covered slot antenna.

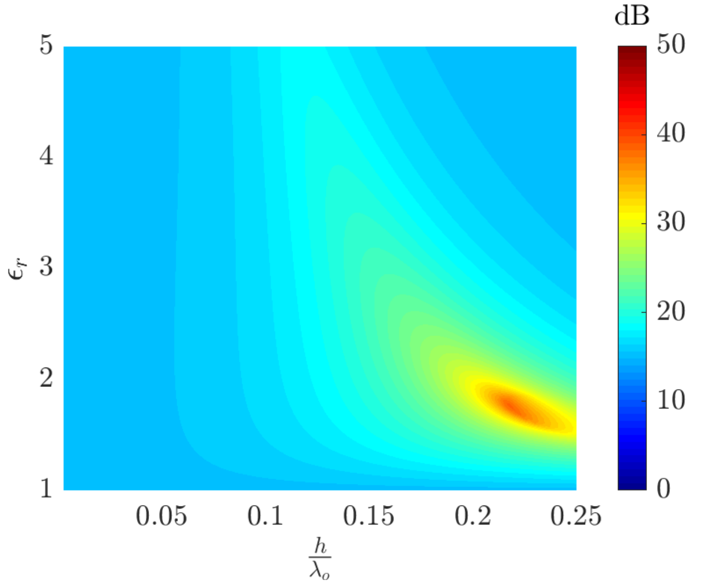

Figure 3.15: Maximum XPD of a dielectric-covered slot antenna in the region $-45^\circ \leq \theta \leq 45^\circ$ and $0^\circ \leq \phi \leq 180^\circ$.

3.4.4 Ultra-Low Cross Polarization Dielectric-Covered Slot Antenna

The Ultra-Low Cross-Polarization Dielectric-Covered Slot Antenna (ULCP-DCSA) stems from the field expressions given by the dielectric-covered slot antenna previously discussed. As it was hypothesized in chapter 1, the reflections of the dielectric-covered ground interact with the radiation characteristics of the antenna which is proved by the difference between the minimum IXR found for the covered and uncovered slots. Here, an algorithm was written to find the maximum co- to cross-polarization difference or Cross-Polarization Discrimination (XPD) within $-45^\circ \leq \theta \leq 45^\circ$. The XPD is calculated for different dielectric constants and thicknesses covering the slot. The algorithm assumes a fixed length and width for the slot which should not have a significant impact in the overall radiation characteristics.

Fig. 3.15 shows the results of such algorithm finding an ultra-low cross-polarization condition for a substrate with dielectric constant of ≈ 1.72 and thickness of $\approx 0.2175\lambda$. In theory, these dielectric characteristics should allow the design of an ULCP-DCSA. Fig. 3.16a, 3.16b, and 3.16c show the theoretically derived and simulated co- and cross-polarization radiation patterns in L3 using the dimensions from Fig. 3.16. As well as in the regular dielectric-covered slot antenna, the ULCP-DCSA shows the same co-polarized assymetries which are the result of exciting the aperture outside of its center with an unbalanced feed. However, the ULCP-DCSA shows E- and H-plane co-polarized fields that are closer together which is a desired characteristic for dual-polarized antennas. Fig. 3.16d shows the IXR for the dual-polarized ULCP-DCSA exhibiting a minimum of 19.8 dB within $-45^\circ \leq \theta \leq 45^\circ$. In spite of these results, neither the simulated model or the mathematically derived fields account for the presence of surface waves. Thus, a practical phased array antenna following on these results will require the elimination of surfaces from the design or their account with improved models, as shown in [65].

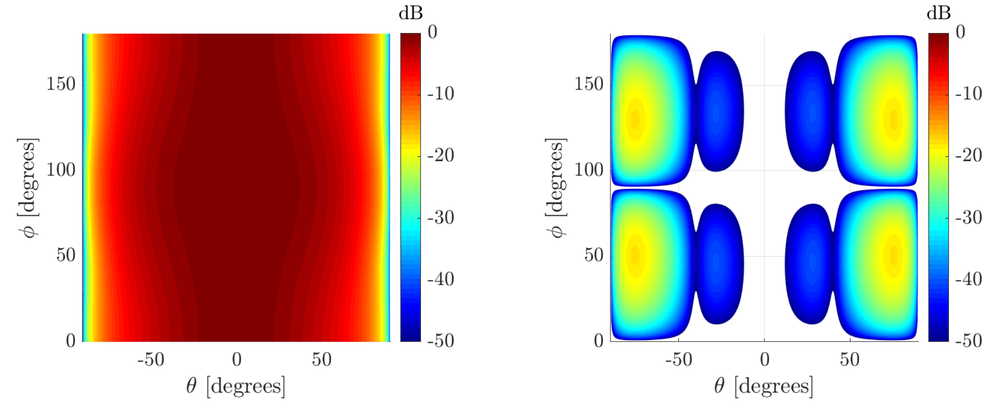

(a) Co-polarization (b) Cross-polarization

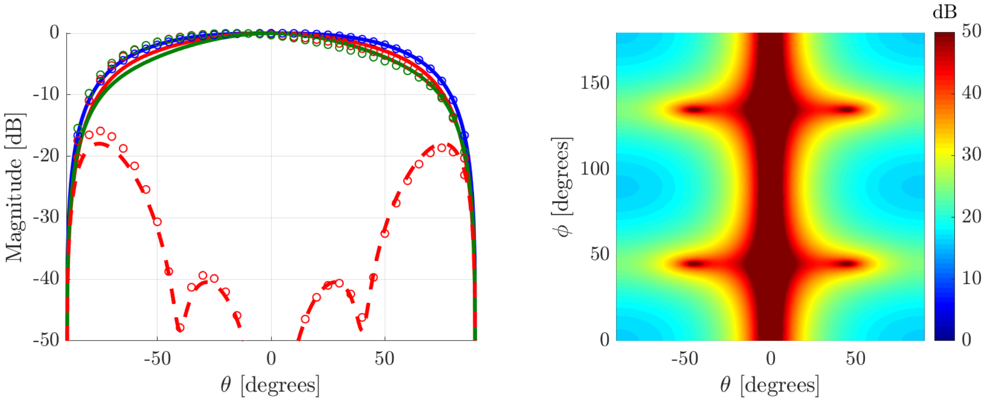

(c) Co- and Cross-polarization Cuts (d) Intrinsic Cross-polarization

Figure 3.16: Radiation characteristics for a dielectric-covered slot antenna with ultra-low cross-polarization characteristics based on Ludwig's third definition of polarization. a,b) Modeled co- and cross-polarized radiation patterns with a = 49 mm, b = 3 mm, $\epsilon_{rd} = 1.72$, and $h_d = 21.75$ mm. Modeled (solid lines) and simulated (circle) co- and cross-polarized radiation patterns cuts for E-(blue), D-(red), and H-plane (green) where the simulation uses: a = 49 mm, b = 3 mm, $\epsilon_{rd} = 2.2$, and $h_d = 21.75$ mm, $\epsilon_{rt} = 3.66$, $h_t = 30$ mils, $W_t = 1.68$ mm, $L_s = 12$ mm, and $L_o = 10.88$ mm. d) Modeled IXR for a dual-polarized dielectric-covered slot antenna with ultra-low cross-polarization characteristics.

3.5 Polarization in Microstrip Patch Antennas

The fields of microstrip patch antennas are usually derived in the literature by employing the magnetic current model [66], [67] or the electric current model [30], [68]. In the former, the equivalence principle is applied to a surface sorrounding the patch geometry. Perfect magnetic walls are assumed for the cavity made by the patch and the ground which makes the radiation viewed as arising from magnetic currents at the edges of the patch. The application of this approch usually ignores the effects of the dielectric underneath the patch while the magnetic currents are assumed to radiate above the ground plane in free space [69]. The electric current model calculates the radiation directly from the currents flowing on top of the patch which is based on the direct Green's function concept [69]. This method in principle allows for a rigorous calculation of the radiation fields with no approximations if the currents in top of the patch are known exactly. The electric current model is used in this work because it already includes the contributions of radiation from the dielectric underneath the patch. Assuming radiation of the dominant mode TM_{10} for the x-polarized microstrip patch antenna shown in Fig. 3.17, the electric fields E_θ and E_ϕ are given by,

$$E_i(r,\theta,\phi) = E_i^{hex}(r,\theta,\phi)\left(\frac{\pi\ WL}{2}\right)\left[\frac{\sin\left(\frac{k_yW}{2}\right)}{\left(\frac{k_yW}{2}\right)}\right]\left[\frac{\cos\left(\frac{k_xL}{2}\right)}{\left(\frac{\pi}{2}\right)^2-\left(\frac{k_xL}{2}\right)^2}\right] \tag{3.29}$$

where the subscript i refers to the θ or ϕ components of the Hertzian electric dipole source found from,

$$E_\theta^{hex}(r,\theta,\phi) = E_0\cos\phi\ G(\theta), \tag{3.30}$$

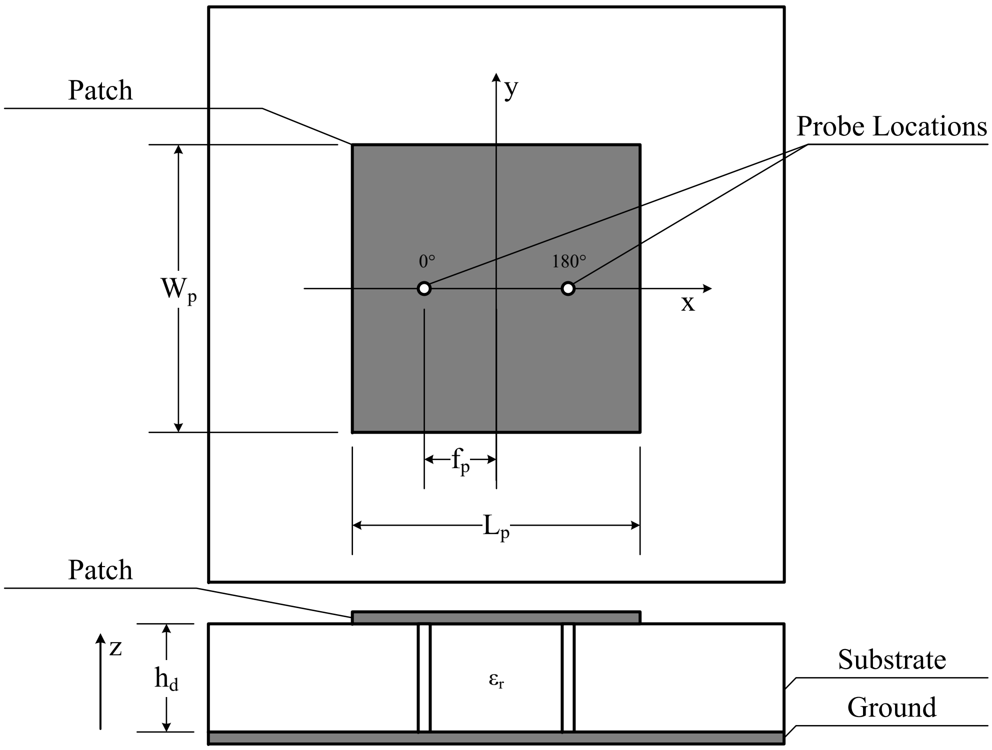

Figure 3.17: Microstrip patch antenna geometry used for modeling and simulations where W_p is the width of the patch, L_p its length, and f_p the feeding location for the lumped ports with impedance $Z_o = 50\ \Omega$. The subtrate supporting the microstrip patch has a dielectric constant ϵ_r and a thickness h_d.

$$E_\phi^{hex}(r,\theta,\phi) = -E_0 \sin\phi\ F(\theta), \tag{3.31}$$

and

$$E_0 = \left(\frac{-j\omega\mu_0}{4\pi r}\right)e^{-jk_0 r}. \tag{3.32}$$

As well as in the dielectric-covered slot, the effects in radiation coming from the dielectric are taken into account by the F(θ) and G(θ) functions given by,

$$F(\theta) = 1 + \Gamma^{TE}(\theta) = \frac{2\tan(k_0 h N(\theta))}{\tan(k_0 h N(\theta)) - jN(\theta)\sec\theta} \tag{3.33}$$

and

$$G(\theta) = 1 + \Gamma^{TM}(\theta) = \frac{2\tan(k_0 h N(\theta))\cos\theta}{\tan(k_0 h N(\theta)) - j\frac{\epsilon_r}{N(\theta)}\cos\theta}, \tag{3.34}$$

where the far-zone fields are defined as,

$$k_x = k_0 \sin\theta\cos\phi \tag{3.35}$$

and

$$k_y = k_0 \sin\theta\sin\phi, \tag{3.36}$$

with the auxiliary function N(θ) given by,

$$N(\theta) = \sqrt{\epsilon_r - \sin^2\theta}. \tag{3.37}$$

Fig. 3.18a, 3.18b, and 3.18c show the theoretically derived and simulated co- and cross-polarization radiation patterns in L3 using the dimensions referenced in Fig. 3.17 and discussed in Fig. 3.18. The microstrip patch produces the lowest cross-polarization in L3 between the dipole in free space, dipole over a ground, waveguide, uncovered slot, and dielectric-covered slot, only second to the ULCP-DCSA. In terms of co-polarization, an excellent agreement is found between the modeled and simulated results with great overlap between E- and H-plane cuts. To calculate the IXR, a coordinate system transformation [64] is used to estimate the y-polarized electric field components from the theoretically derived x-polarized expressions. Fig. 3.18d shows the IXR for a dual-polarized microstrip patch antenna producing a minimum of 24.2 dB within $-45^\circ \leq \theta \leq 45^\circ$, representing an improvement of 4.4 dB over the ULCP-DCSA.

3.5.1 Ultra-Low Cross-Polarization Microstrip Patch Antenna

The Ultra-Low Cross-Polarization Dielectric Microstrip Patch Antenna (ULCP-MPA) stems from the field expressions given by the electric current model previously discussed. As it was hypothesized in chapter 1, the reflections of the dielectric-covered ground interact with the overall radiation characteristics of the antenna. Here, an algorithm was written to find the maximum co- to cross-polarization within $-45^\circ \leq \theta \leq 45^\circ$ for different dielectric constants and thicknesses underneath the microstrip patch. The dimensions of the patch are calculated through the transmission line model [28] assuming $L_p = W_p$.

Fig. 3.19 shows the results of such algorithm finding an ultra-low cross-polarization condition for a substrate with dielectric constant of ≈ 1.72 and

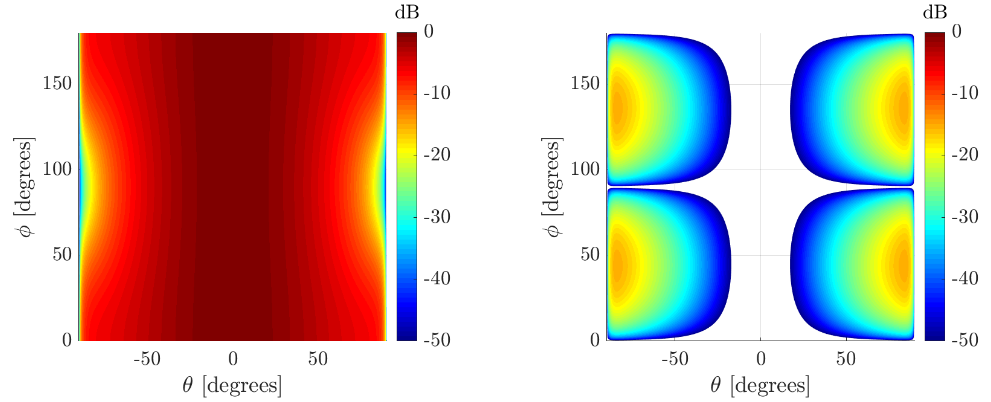

(a) Co-polarization (b) Cross-polarization

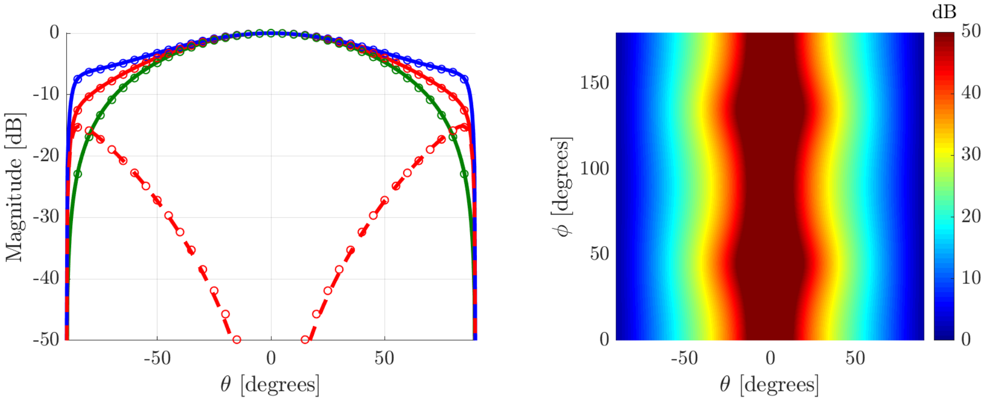

(c) Co- and Cross-polarization Cuts (d) Intrinsic Cross-polarization

Figure 3.18: Radiation characteristics for a microstrip patch antenna on an infinite ground based on Ludwig's third definition of polarization operating at 3 GHz. a) Modeled microstrip patch antenna in HFSS with $f_p = 3.5$ mm, $L_p = W_p = 32.25$ mm, $h_d = 60$ mils, and $\epsilon_{rd} = 2.2$. b) Modeled co-polarized radiation pattern. c) Modeled cross-polarized radiation pattern. d) Modeled (solid lines) and simulated (circle) co- and cross-polarized radiation patterns cuts for E-(blue), D-(red), and H-plane (green). e) Modeled IXR for a dual-polarized microstrip patch antenna.

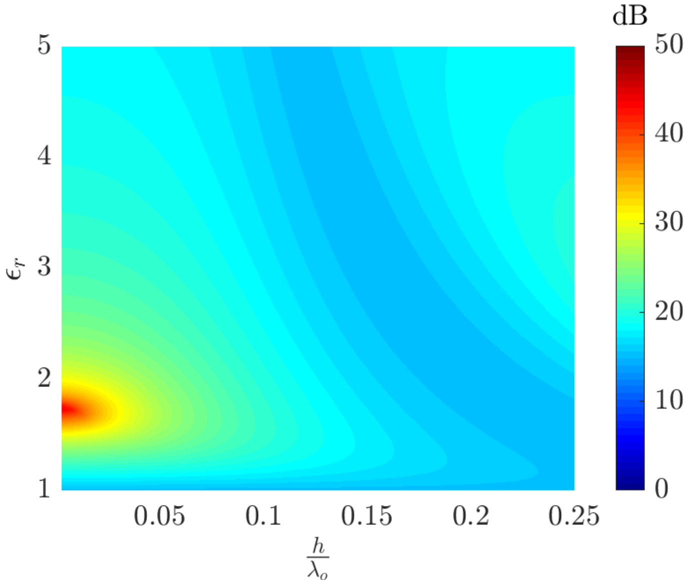

Figure 3.19: Maximum co- to cross-polarization difference of a square microstrip patch antenna derived from the electric current model in the region $-45° \leq \theta \leq 45°$ and $0° \leq \phi \leq 180°$ operating at 3 GHz.

thickness of $\approx 0.01\lambda_o$. In theory, these dielectric characteristics should allow the design of an ULCP-MPA. Fig. 3.20a, 3.20b, and 3.20c show the theoretically derived and simulated co- and cross-polarization radiation patterns in L3 using the dimensions mentioned in Fig. 3.20. When compared to the regular microstrip patch antenna, the ULCP-MPA shows even closer co-polarized radiation cuts with cross-polarization levels below -40 dB within $-48° \leq \theta \leq 48°$. Fig. 3.20d shows the IXR for the dual-polarized ULCP-MPA exhibiting a minimum of 33.8 dB within $-45° \leq \theta \leq 45°$, representing an improvement of 9.6 dB over the regular microstrip patch antenna. Even though the ULCP-DCSA and ULCP-MPA require different dielectric thicknesses, it is curious that both antennas require the same dielectric constant to achieve ultra-low cross-polarization characteristics.

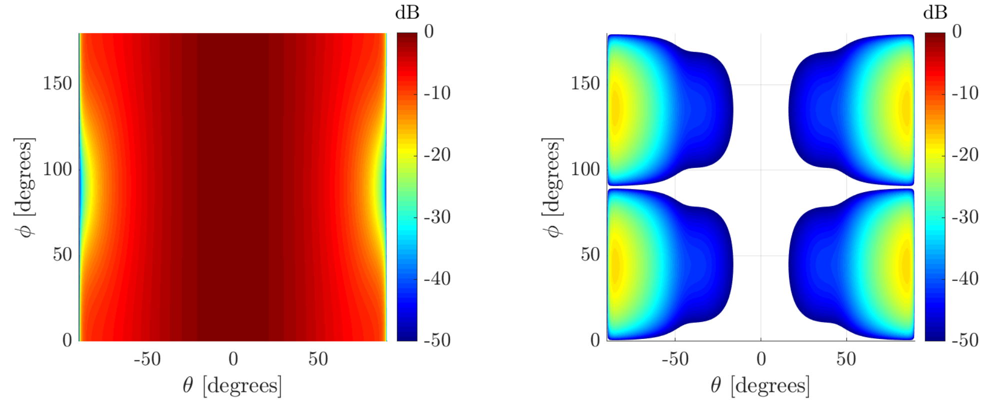

(a) Co Polarization (b) Cross Polarization

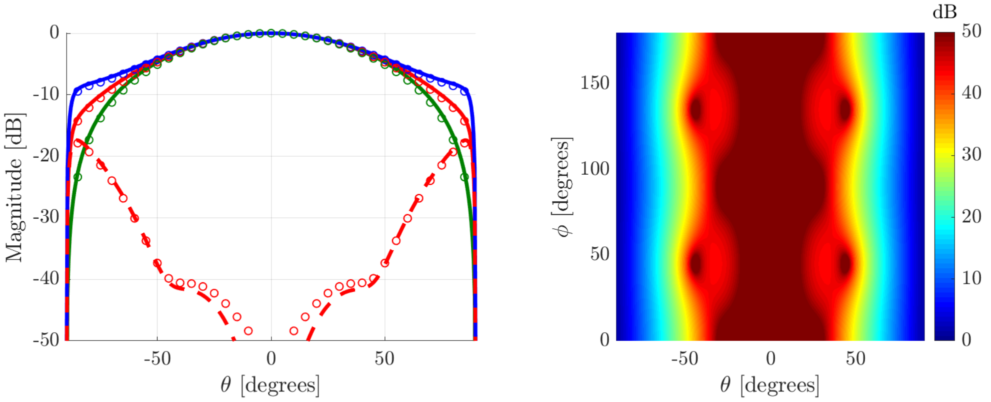

(c) Co and Cross Polarization Cuts (d) Intrinsic Cross Polarization

Figure 3.20: Radiation characteristics for a microstrip patch antenna on an infinite ground based on Ludwig's third definition of polarization. a) Modeled microstrip patch antenna in HFSS with $f_p = 3.7$ mm, $L_p = W_p = 36.25$ mm, $h_d = 60$ mils, and $\epsilon_{rd} = 1.72$. b) Modeled copolarized radiation pattern. c) Modeled crosspolarized radiation pattern. d) Modeled (solid lines) and simulated (circle) co and crosspolarized radiation patterns cuts for E-(blue), D-(red), and H-plane (green). e) Modeled IXR for a dual-polarized microstrip patch antenna.

3.6 Summary

All relevant fundamentals regarding antenna polarization were discussed in this chapter. Section 3.1 covered the widely accepted definitions of antenna polarization, the required polarization of polarimetric weather radars, and the dual-polarized intrinsic cross polarization (IXR). It was shown that co- and cross-polarization depend on a coordinate system which makes some antennas radiate cross-polarization when aligned with a particular axis (i.e., y-dipole vs. x-polarized dipole in L2-I). The IXR was proposed as a convenient FoM to extract the coordinate systems dependencies of polarization in dual-polarized weather antennas. Moreover, it was shown that the IXR relates to the final, calibrated polarimetric measurement errors making it a better metric to characterize dual-polarized weather antennas. Armed with these knowlege, multiple antenna architectures (i.e, dipole, horizontal dipole over ground, waveguide, slot, dielectric-covered slot, and microstrip patch antennas) commonly used today in phased arrays were evaluated in terms of cross-polarization and IXR. It was found that microstrip patch antennas provide the highest IXR, making them the most convenient antenna element for polarimetric weather radars.

Chapter 4

Dual-Polarized Microstrip Patch Antennas for Polarimetric Weather Radars

4.1 Introduction

It has been shown so far that microstrip patch antennas exhibit the lowest cross-polarization levels in L3 polarization accompanied by the highest IXRs among dipole, horizontal dipole, waveguide, slot, and dielectric-covered slot antennas. Unfortunately, microstrip patch antennas can exhibit narrow bandwidths, surface waves, and low efficiencies. These disadvantages, however, can be compensated through improved design. This chapter covers microstrip patch antenna design trade-offs with the goal of manufacturing practical dual-polarized radiating apertures. Section 4.2 focuses on understanding the most important shortcomings present in the design of microstrip patch antennas and the trade-offs that can be made depending on project requirements. Section 4.3 discusses the results of the designed Horus, Horus-ONR, and PAIR antennas with simulated models and measurements.

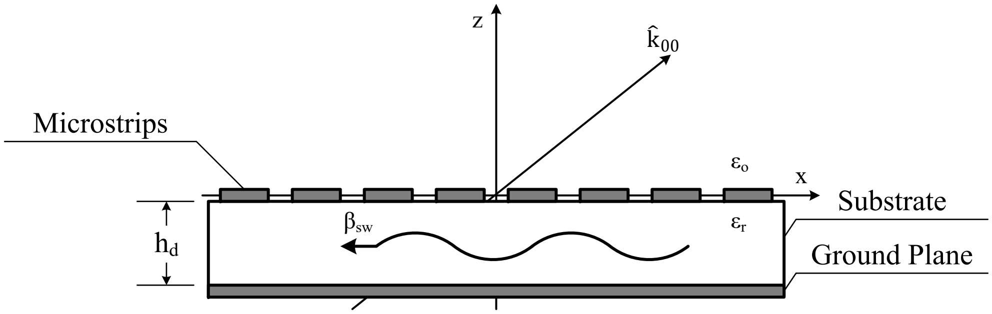

Figure 4.1: Grounded dielectric substrate with infinite extension along y- and x-axis where β_{sw} is the propagation constant of the grounded dielectric substrate, ϵ_r its relative permittivity, and h_d its thickness. $\hat{k_{00}}$ refers to the free space propagation constant.

4.2 Microstrip Patch Antenna Design Trade-Offs

4.2.1 Surface Waves

A surface wave is an example of a non-uniform plane wave excited in planar dielectric-coated grounds [51]. Surface waves are characterized by having amplitude variations along z-axis with propagation in the x-direction and y-direction, as shown in Fig. 4.1. Surface waves have the potential of introducing scan blindness in arrays, as it was shown for a printed dipole antenna in Section 2.3.1. Their prescense depend on the thickness of the substrate and its dielectric constant. Scan blindnesses due to surface waves in planar phased arrays are predicted in uv-space by [54], [70],

$$\left(\frac{\beta_{sw}}{k_0}\right)^2 = \left(\frac{p}{d_x/\lambda} + u\right)^2 + \left(\frac{q}{d_y/\lambda} + v\right)^2, \tag{4.1}$$

where p and q refer to the integer Floquet mode indexes, d_x and d_y to the antenna unit-cell dimensions along $x-$ and $y-$axis, and β_{sw} and k_0 to the dielectric surface wave and free space propagation constants. The propagation constant of the surface wave is found through a graphical method where the characteristic TE and TM mode equations are simulatenously solved enforcing field continuity in the air/dielectric interface. The TE and TM mode equations are given by,

$$k_c h_d \tan k_c h_d = \epsilon_r h h_d, \tag{4.2}$$

$$-k_c h_d \cot k_c h_d = h h_d, \tag{4.3}$$

where k_c and h represent the cutoff wave numbers for the dielectric and the air region, respectively. The graphical method is accomplished through field continuity by,

$$(k_c h_d)^2 + (h h_d)^2 = (\epsilon_r - 1)(k_0 h_d)^2, \tag{4.4}$$

with TM and TE mode cutoff frequencies given by,

$$TM_n : f_c = \frac{n c_0}{2 h_d \sqrt{\epsilon_r - 1}}, \quad n = 0, 1, 2... \tag{4.5}$$

$$TE_n : f_c = \frac{n c_0}{4 h_d \sqrt{\epsilon_r - 1}}, \quad n = 1, 2, 3... \tag{4.6}$$

where c_0 is the speed of light in a vacuum. Eqs. 4.2 and 4.3 are tangent functions that intersect the circle defined by Eq. 4.4. These intersections then represent a possible solution of k_c. Eqs. 4.5 and 4.6 provide information about the cutoff frequencies of the modes and their ordering. Once k_c is found, the surface wave propagation is calculated from,

$$\beta_{sw} = \sqrt{\epsilon_r k_0^2 - k_c^2}. \tag{4.7}$$

Fig. 4.2 shows the surface wave mode propagation analysis and the planar phased array grating lobe diagram for the printed dipole antenna discussed in Section 2.3.1. The simulated printed dipole model has $\epsilon_r = 2.2$ and $h_d =$ 25 mm for which two scan blindnesses were found in E-plane at $\approx 45°$ and in H-plane at $\approx = 81°$, as shown in Fig. 4.2a. These scan blindnesses are predicted using the graphical method derived from Eqs. 4.2 - 4.7. Fig. 4.2b shows the TM (red) and TE (blue) mode tangent curves solved for hh_d (i.e., Eqs. 4.2 and 4.3) intersecting the circle with radius $\sqrt{\epsilon_r - 1}(k_0 h_d)$ drawn with Eq. 4.4. The TM_0 and TE_1 mode intersections lead to $\beta_{sw} = 1.28$ and 1.01, respectevily.

Fig. 4.2c shows the grating lobe diagram (black) for the dipole array with $\lambda_o/2$ spacing and its modified counterpart (blue) including the propagation constant $\beta_{sw} = 1.28$. It is clear that no grating lobes are excited when $d_x = d_y = \lambda_o/2$ (i.e., no overlap between black circles). However, when $\beta_{sw} = 1.28$, the black circles are modified to overlay the surface wave mode with a radius equal to the propagation constant (blue circles). In this particular case, the modified grating lobe enters the visible region of the array predicting a scan blindness at $\pm$ 45.89°. Following the same procedure for mode TE_1 leads to a scan blindness at $\pm$ 81.73°. Although both TM_0 and TE_1 modes intersect both u- and v-axes in the visible region of the array, their blindnesses occur along their respective polarizations. For TM_0 mode, the blindness is co-polarized with the E-plane while for TE_1 manifests along the H-plane. These results prove that surface waves could be predicted before starting an antenna design.

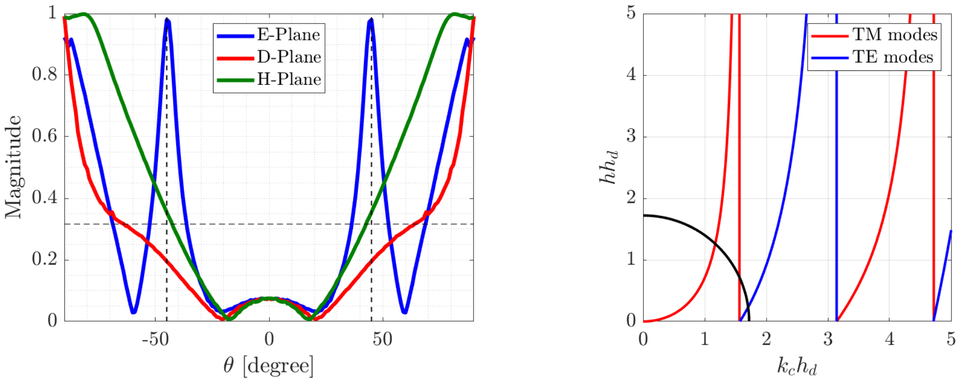

(a) Simulated Dipole from Section 2.3.1 (b) Surface Wave Propagation Analysis

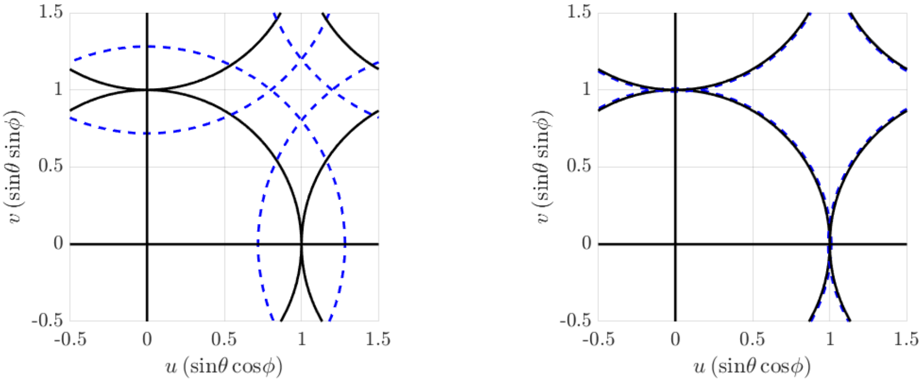

(c) Grating Lobe Diagram for TM_0 (d) Grating Lobe Diagram for TE_1

Figure 4.2: Surface wave propagation constant analysis and grating lobe diagrams for a substrate with a dielectric constant of $\epsilon_r = 2.2$ and $h_d = 25$ mm. a) Simulated dipole geometry from Section 2.3.1. b) Surface wave propagation constant analysis for TE and TM modes. c) Grating lobe diagram considering mode TM_0 where its moved from 90° to 45.89°. d) Grating lobe diagram considering mode TE_1 where its moved from 90° to 81.73°.

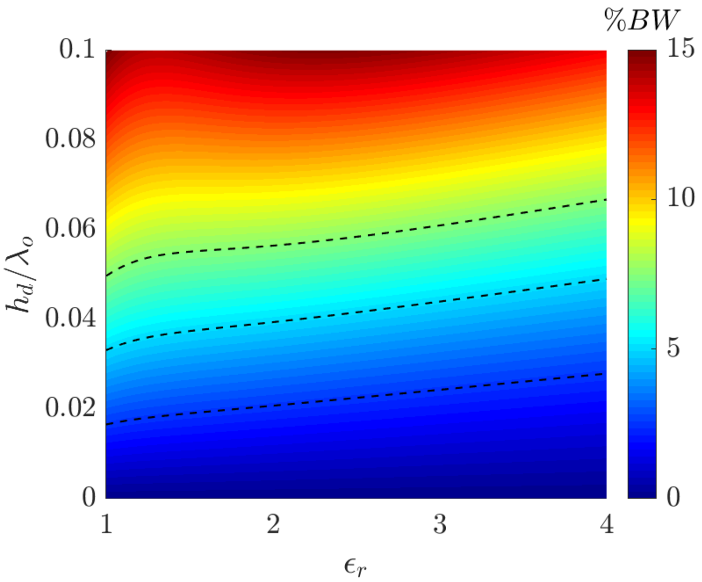

Figure 4.3: Bandwidth capabilities of a square microstrip patch antenna as a function of dielectric constant and substrate thickness using TL model [69]. Note, dashed lines represent contours bandwidth percentages of 2.5, 5, and 7.5%.

4.2.2 Bandwidth

Possibly the main drawback of using microstrip patch antennas in phased arrays is their limited impedance bandwidth [31], [67], [71]. Usually, using a thick substrate material with a low dielectric constant is enough for overcoming this issue. However, surface waves can propagate as the thickness of the dielectric substrate is increased. Fig. 4.3 shows the bandwidth capabilities of a square microstrip patch antenna as a function of substrate thickness and dielectric constant using the TL model [30]. It can be seen that to achieve a bandwidth of 10% with a dielectric constant of 2.2, a thickness of $\approx 0.075\lambda_o$ (i.e., $\approx$ 295 mils at 3 GHz) is required. This example shows a clear constraint found in practical microstrip patch antenna arrays designed for low frequencies, given that these thicknesses exceed manufacturing industry standards.

One way to avoid the use of thick materials, which improves bandwidth, is using multisection matching networks (MMN). However, unit-cell size constraint (i.e., $d_x = d_y = 0.5\lambda_o$) makes MMN difficult to integrate in planar phased arrays [31]. Another famous approach to improve the bandwidth is the stacked patch, which offers increased aperture efficiency when compared to a single patch [72]. This technique allows for a reduction in the dielectric thickness required to achieve the same bandwidth that a single patch offers while simulatneously reducing the possibility of surface waves. Therefore, the stacked patch technique was incorporated in all next-generation weather antennas presented in this work.

4.2.3 Isolation and Cross-Polarization

The isolation and cross-polarization levels in microstrip patch antennas are determined by the presence of unwanted excited modes, which relate to the physical characteristics of the radiating element such as: substrate dielectric constant and thickness, width/length of the patch, and patch feeding network [73], [74]. Cross-polarization mitigation techniques have been discussed in the literature for antenna elements (i.e., antenna element cross-polarization) and arrays (i.e., cross-polarization of the array). In the latter, mirroring of the array elements in the aperture have lowered array cross-polarization through field cancelation of neighboring elements [75]. In this work, we make use of mirroring techniques at the array level to further improve low cross-polarization array capabilities. Moreover, we introduce small subarray gaps with continuous ground planes to reduce the possibility of subarray grating lobes [76] and edge-diffracted cross-polarization [77].

At the element, dual-polarized microstrip antenna requires for the patch to have equal or nearly equal length and width. This requirement makes the cross-polarization levels to depend mostly in the characteristics of the feeding network and the dielectric constant underneath the microstrip patch (as proved in Section 3.5.1). As discussed in chapter 1, the balanced probe-fed and aperture couple technique are preferred when exciting microstrip patches because of their low-cross polarization capabilities. However, the aperture coupled techinique is more suited for low frequency applications or those requiring higher bandwidths. In this work, we make use of symmetry and balanced feeding techiniques to cancel near-field interactions that increase cross-polarization levels in the embedded element radiation patterns.

4.2.4 Efficiency

As well as for the bandwidth, the radiation efficiency of microstrip patch antennas is mostly dictated by the electrical properties of the supporting dielectric substrate in the absence of a feeding network. Fig. 4.4 shows the expected radiation efficiency (i.e., efficiency as a percentage) of a square microstrip patch antenna as a function of the substrate thickness and dielectric constant using the TL model [30]. It can be seen that lower dielectric constants and substrate thickness lead to higher antenna efficiencies. In this work we make use of low dielectric constants to maximize antenna radiation efficiency while incorporating reasonably thick substrates to satisfy the bandwidth requirements of all phased array projects.

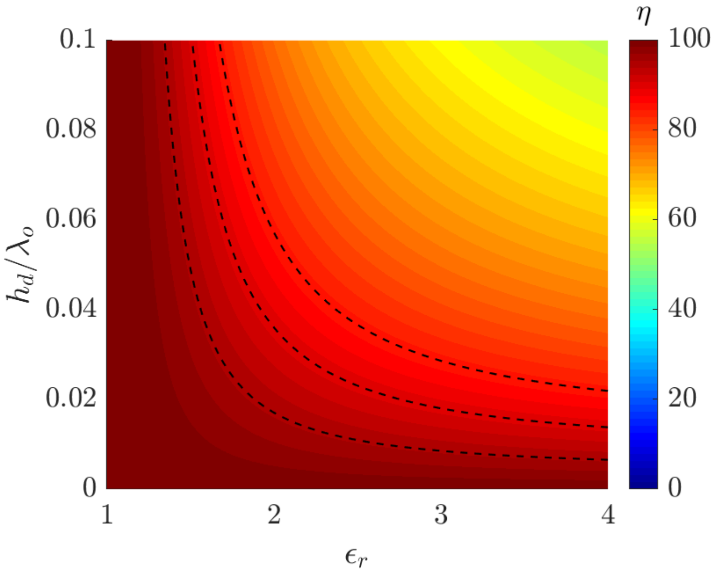

Figure 4.4: Efficiency capabilities of a square microstrip patch antenna as a function of dielectric constant and substrate thickness using TL model [69]. Note, dashed lines represent contour efficiency percentages of 85, 90, and 95%.

4.3 Next-Generation Phased Array Radar Antennas

4.3.1 The Horus Antenna

The Advanced Radar Research Center (ARRC) has been working with NOAA's National Severe Storms Laboratory (NSSL) on an all-digital polarimetric phased array radar for multi-mission surveillance called Horus [10], [78]. As an all-digital polarimetric phased array radar with multi-mission capabilities, Horus requires an antenna element with very well-matched co-polarized radiation patterns and low cross-polarization, for all frequencies between 2.7 and 3.1 GHz, in a field of view of ± 45°. Due to its wide operational bandwidth and low cross-polarization requirements, the best suited antenna for Horus is an aperture coupled microstrip patch.

A dual-polarized aperture coupled microstrip antenna requires a ground plane with crossed-slots for H- and V-polarization excitation, as shown in chapter 1, Fig. 1.6. In this configuration, four metallic layers are required. However, the Horus antenna must include a layer (i.e., metallic layer) for a parasitic microstrip patch and three for its feeding network. The parasitic microstrip patch is responsible for increasing the antenna bandwidth while the three extra layers for the feeding network allow continuous planar integration and unique element excitation. Fig. 4.5 shows the finalized Horus antenna unit-cell and Fig. 4.6 shows the antenna stackup for manufacturing. The antenna stackup is divided in two sub-assemblies to allow independent manufacturing of the feeding network and radiating sources. One of the main advantages of this configuration is the flexibility to build-up thick substrate stackups for the microstrip patches without the need of via plating. The Horus stackup is made from a combination of low loss dielectric substrates and adhesives to maximize antenna efficiency and minimize surface wave excitation. The electrical properties of the used materials are shown in Table 4.1.

Each antenna element is excited by a pair of 50 Ω SMP-Max connectors (i.e., one for H-polarization and one for V-polarization). From these connectors, the signal goes through a coplanar waveguide in series to via V1, establishing connection to the H/V TL layer L5, as shown in Fig. 4.6. L5 consists of length-matched 50 Ω TLs distributed to excite each individual element and polarization. The signal then connects to via V3 or V5 to excite the horizontal (L3) or vertical (L1) $\lambda_{eff}/4$ power divider transformer. The transformers excite the apertures on L2 which then are responsible of exciting the microstrip patches in L1 and L2 in sub-assembly 2. Vias V3 and V5 are backdrilled at the end of production of sub-assembly 1 to break their connection with L1 (H-polarization) and L6 (H- and V-polarization), leaving a short stub considered in simulations. Vias V2 and V4 are used throughout the unit-cell to improve

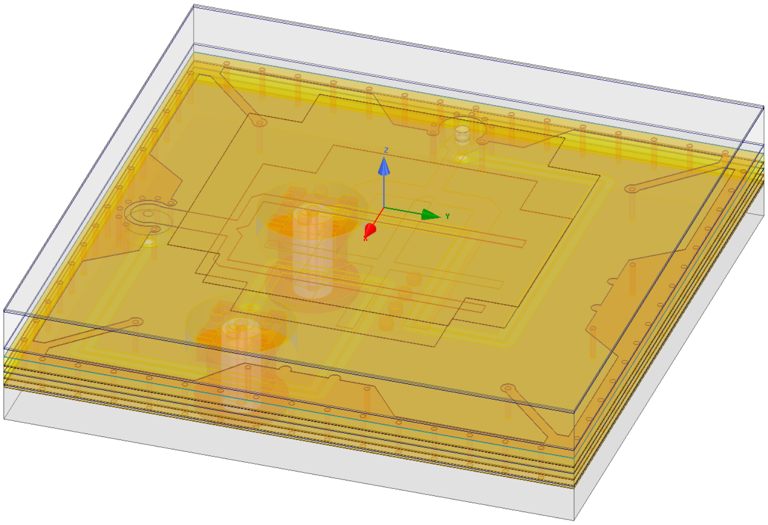

(a) Horus Antenna Unit-cell

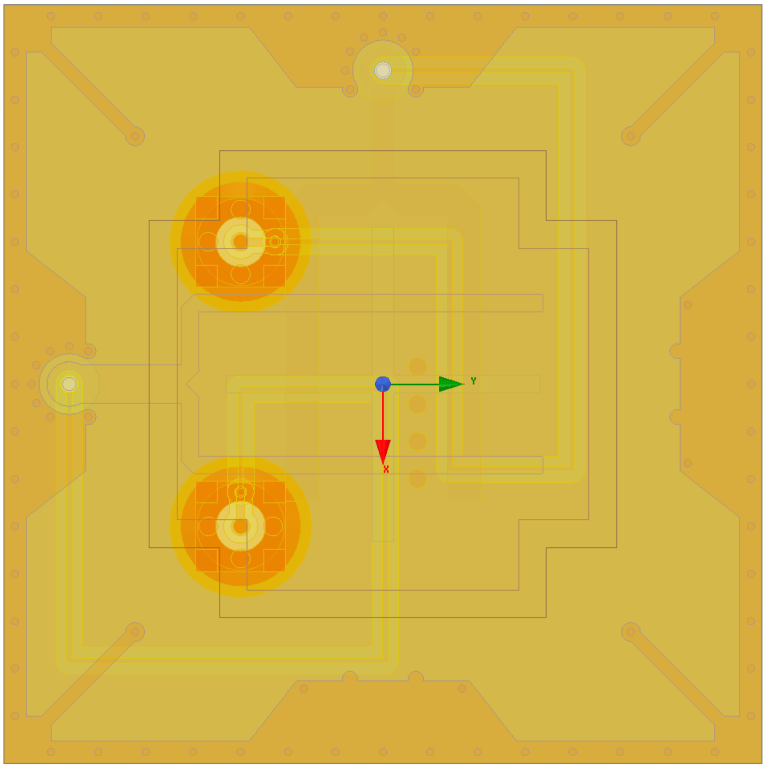

(b) Horus Antenna Top View

Figure 4.5: Simulated Horus antenna unit-cell used for simulations in Ansys HFSS. a) Horus antenna 3D model. b) Horus antenna top view.

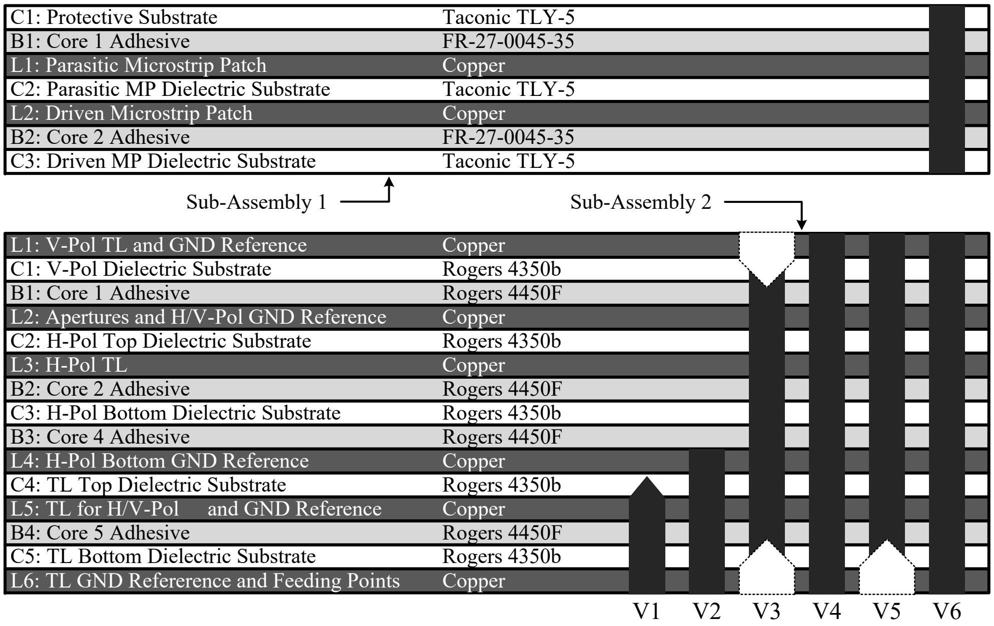

Figure 4.6: Horus antenna stackups and via configuration with the following substrate thicknesses (all in mils). Sub-assembly 1: C1 - 5, B1 - 6.2, L1 - 1.4, C2 - 140, L2 - 1.4, B2 - 6.2, C3 - 30. Sub-assembly 2: L1 - 2, C1 - 30, B1 - 4, L2 - 1.4, C2 - 20, L3 - 1.4, B2 - 4, C3 - 20, B3 - 4, L4 - 1.4, C4 - 20, L5 - 1.4, B4 - 4, C5 - 6.6, L6 - 2 . Note 1: C = Substrate Core, B = Bondply or Prepreg, and L = Copper Layer. Note 2: V1 - controlled depth signal via, V2 - controlled depth GND via, V3 - backdrilled via for H-pol, V4 - through GND via, V5 - V-pol backdrilled via, V6 - non-plated via for antenna mounting.

Table 4.1: Substrates integrated in the Horus antenna design and their respective electrical properties.

Material	**Dielectric Constant** (ϵ_r)	**Tangent Loss** ($\tan\delta$)
Taconic TLY-5	2.2	0.0009
FR-27-0045-35	2.74	0.0014
Rogers 4350B	3.66	0.0037
Rogers 4450F	3.52	0.004

H/V isolation while vias V6 serve for sub-assembly alignment and antenna mounting. Please refer to Appendix B.1 for antenna element mirroring and excitation in the manufactured array.

Simulated Results at Boresight

The Horus antenna unit-cell follows design guidelines of aperture coupled microstrip patch antennas shown in [79]–[81]. However, due to the complexity of the unit-cell, it is not practical to offer the reader a comprehensive list of the via positions, lengths and widths of each TL segment, or dimensions for clearances around the feeding network. It is rather more insightful to discuss some important design guidelines considered in the antenna.

- Radiating dielectric substrates - We designed a total of three antenna revisions: one version using Rogers 5880LZ [42] and two using Taconic TLY-5. The use of Rogers 5880LZ (i.e., a substrate with $\epsilon_r = 2.0$ over Taconic TLY-5 with $\epsilon_r = 2.2$) allows the exposed V-polarization geometry over the ground plane to introduce more sporious radiation at grazing angles. This radiation is expected to lower at the array through antenna element mirroring. However, multiple PCB manufacturers preferred us to use glass microfiber reinforced PTFE composites due to their mechanical advantages. It is encouraged to use either Rogers 5880 or Taconic TLY-5 in combination with a higher dielectric constant material such as Rogers 4350B for the feeding network.

- Aperture or slot coupling - It is important to mantain the nature of the apertures non-radiating because they can introduce spurious radiation. This can be accomplished by setting a limit on the overall length of the slot to be less than $\lambda_{eff}/3$.
- Coupling vias - Note the four symmetrical vias located at the end of the grounded transmission lines, exiting from the corners of the unit cell shown in Fig. 4.5b. These vias are responsible of controlling the coupling of the apertures to the microstrip patches. Thus, these vias must be kept constant while tuning each polarization.
- Microstrip patch geometry - It is encouraged to use a cross geometry for the microstrip patches. The cross geometry offers an extra coupling variable that allows for frequency tuning while can also reduce the number of excited modes [82].

Surface wave analysis for the unit-cell considering dielectric substrates above ground layer L3 in sub-assembly 1 yields a $\beta_{sw} = 1.0233$ for $dx = dy = 50.8$ mm, which translates to scan blindness at 61.84°, as shown in Fig. 4.7. These results show that no scanning blindness are introduced in the antenna field of view through surface waves. Fig. 4.12a and Fig. 4.12b show the simulated active S-parameters and realized gain at boresight for H- and V-polarizations using infinite array approach in HFSS. It is clear that both polarizations exhibit very similar ARC results with an overall %BW of 15.4% while their isolation

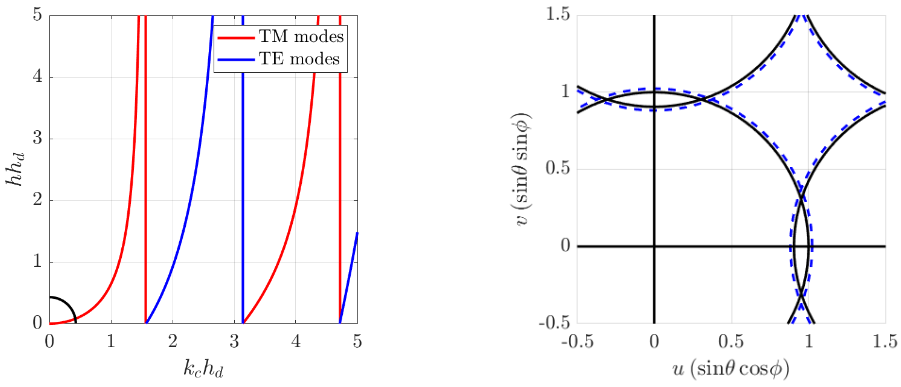

(a) Surface Wave Propagation Analysis (b) Grating Lobe Diagrams

Figure 4.7: Surface wave propagation constant analysis and grating lobe diagrams at 3.1 GHz for the Horus antenna stackup where $\epsilon_r \approx 2.43$ and $h_d \approx 217.4$ mils. a) Surface wave propagation constant analysis where ϵ_r is calculated based on a weighted average. b) Grating lobe location is moved from 64.82° to 61.84°.

is lower than -55 dB, as shown in Fig. 4.12a. These same results conduce to highly efficient realized gains at boresight when compared to the theoretical gain of the unit-cell shown in Fig. 4.12b.

Simulated Results when Scanning

The Horus antenna unit-cell is evaluated across multiple scanning directions to extract the ARC and radiation patterns at a frequency of 2.9 GHz. Note that every desired scanning beam requires a different simulation. Fig. 4.9a and Fig. 4.9b show the scanning ARC for *E*-, *D*-, and *H*-plane for H- and V-polarization for $\theta = \pm\, 60°$ with a resolution of 5°. The antenna is capable of scanning at this frequency up to ± 45° in all planes and for both polarizations, maintaining an ARC below -10 dB. In fact, the Horus antenna could continue scanning on the *E*- and *D*-plane further than $\theta = 45°$ at the expense of a reduced realized gain.

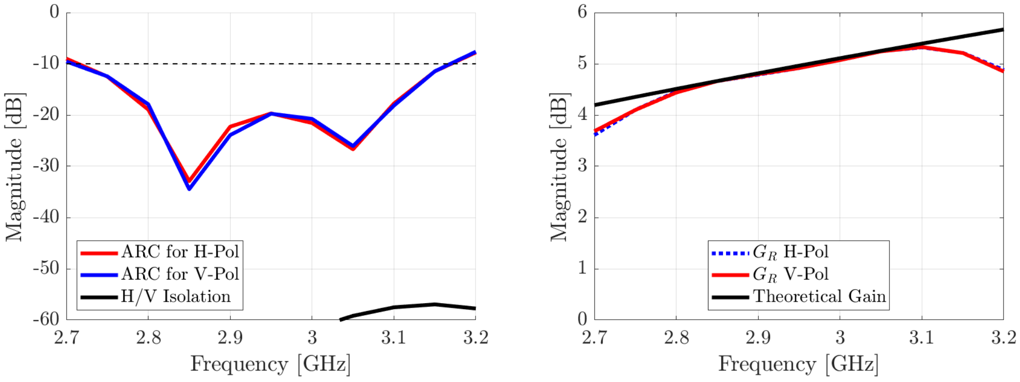

(a) Active S-Parameters (b) Realized Gain

Figure 4.8: Simulated active S-parameters and realized gain at boresight based on infinite array analysis in HFSS. a) Active S-parameters for H- and V-polarization. b) Realized gain for H- and V-polarization.

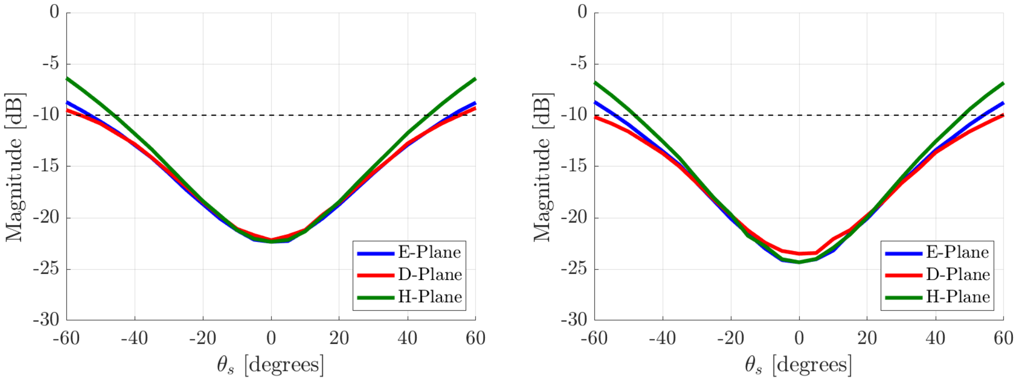

(a) H-Pol ARC (b) V-Pol ARC

Figure 4.9: Simulated active reflection coefficient cuts for *E*-, *D*-, and *H*-plane at 2.9 GHz. a) H-polarization ARC. b) V-Polarization ARC.

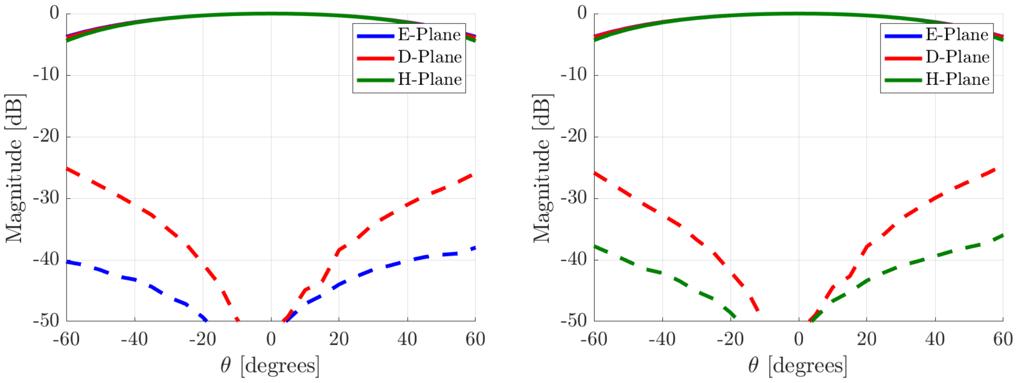

(a) H-Pol Radiation Pattern Cuts (b) V-Pol Radiation Pattern Cuts

Figure 4.10: Simulated normalized radiation pattern cuts for *E*-, *D*-, and *H*-plane based on Ludwig's third definition of polarization at 2.9 GHz. a) H-polarization radiation patterns cuts. b) V-Polarization radiation pattern cuts.

Fig. 4.10 shows the normalized radiation patterns in Ludwig's third definition of polarization for *E*-, *D*-, and *H*-plane. As well as in the ARC, the co-polarization patterns for H- and V- are very similar, with a co-polarized radiation pattern difference lower than 0.08 dB between *E*-, *D*-, and *H*-plane in $\theta = \pm 45°$. In terms of cross-polarization, *E*- and *H*-plane show levels of -40 dB in most of the region of $\theta = \pm 45°$. The *D*-plane in the other hand shows cross-polarization of -29 dB. These cross-polarization levels are expected to be lower at the array due to the use of element mirroring in the aperture. According to these results, the Horus antenna satisfies the phased array requirements of co-polarized beam matching for polarimetric measurements but not the cross-polarization for simultaneous transmit and receive (STSR). However, as it was discussed in chapter 3, the IXR of microstrip patches is the highest between all commonly used antenna architectures in phased arrays making the Horus antenna one of the highest calibratable elements for weather measurements.

Measured Results at Boresight

The performance of the Horus antenna is validated through the mutual coupling measurements of a central element in the array discussed in Section 2.2.2. The manufactured antenna is made from 64 elements distributed on an 8 x 8 grid. However, a 16 x 16 array was made for measurements using four manufactured units. The element reference for these measurements is [8,8], where the first number in the brackets indicates column position and the second, row position. The antenna was setup in a small anechoic chamber and measurements were gathered with a 2-port network analyzer. One port of the network analyzer was left connected throughout the course of the measurements to a reference polarization (i.e., H- or V-polarization) while the other was moved to measure the couplings to all other elements. Fig. 4.11 shows the results of these measurements for H- and V-polarization at 2.9 GHz. Note that for the reference element, the shown coupling is for the passive self-reflection of the measured polarization. Each set of measurements exhibits similar results with higher couplings present along their respective polarization directions.

Fig. 4.12 shows the ARC at boresight as well as the realized gain for both polarizations, using the coupling measurements shown in Fig. 4.11. The calculated ARC through the mutual coupling measurements show fair agreement with the simulated unit-cell. It is unclear at this point if the discrepancies between H- and V-polarization in the ARC are due to measurement errors (i.e., cable phase and calibration stability throughout the measurements) or intrinsic differences in the manufactured geometry.

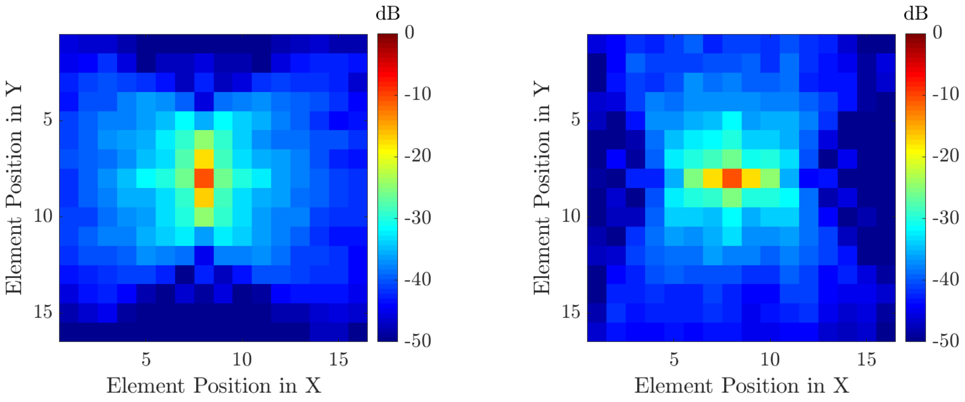

(a) Mutual Coupling for H-Pol

(b) Mutual Coupling for V-Pol

Figure 4.11: Mutual coupling measurements for H- and V-polarizations for element [8,8] in the 16 x 16 Horus antenna array at 2.9 GHz. a) Mutual coupling measurements for H-polarization. b) Mutual coupling measurements for V-polarization.

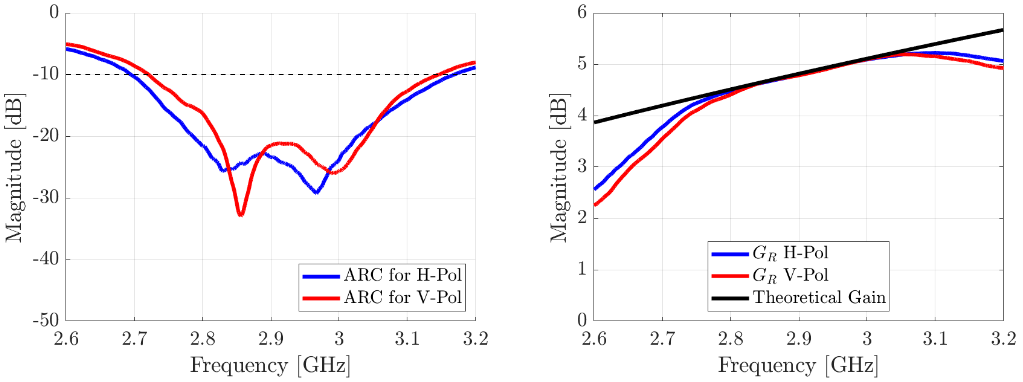

(a) Active S-Parameters

(b) Realized Gain

Figure 4.12: Measured ARC and realized gain at boresight for element [8,8] in the 16 x 16 Horus antenna array based on the mutual coupling measurements shown in Fig. 4.11. a) Active S-parameters for H- and V-polarization. b) Realized gain for H- and V-polarization.

Measured Results when Scanning

Figs. 4.13 and 4.14 show the scanning ARC for H- and V-polarization as a function of scanning angle θ/ϕ or AZ/EL and operational frequencies using the mutual coupling results shown in Fig. 4.11. The antenna sustains for both polarizations an ARC below -10 dB for most of the required AZ/EL range. Moreover, the antenna also sustains an ARC below -10 dB for all designed frequencies in ϕ cuts 0°, 45°, and 90°. However, some of these results might prove misleading to the reader.

Figs. 4.13d and 4.14b show ARCs lower than -10 dB for $\theta = \pm 90°$ in frequency ranges around 2.7 GHz. These results are misleading because the antenna couplings are truncated to the size of the measured array (i.e., 16 x 16) which results in anomalies in the calculated ARC for grazing angles. To obtain more accurate results for angles near grazing, the size of the array has to be increased. Unfortunately, at the time of this work there was no plans on measuring a bigger array because the obtained results were sufficient to validate the performance of the antenna against simulations.

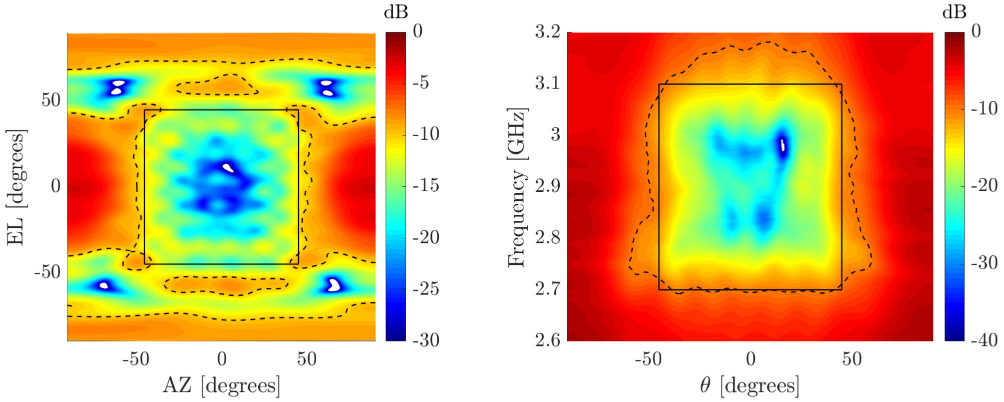

(a) ARC at 5.4 GHz

(b) ARC Across Frequencies for $\phi = 0°$

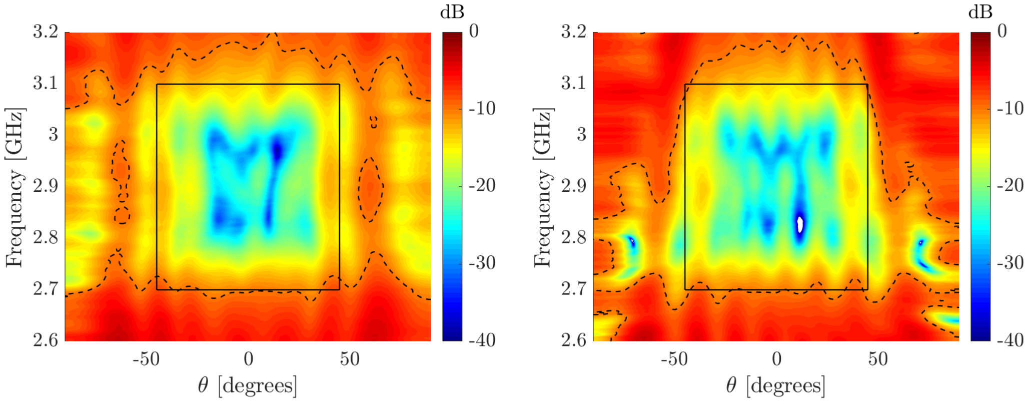

(c) ARC Across Frequencies for $\phi = 45°$

(d) ARC Across Frequencies for $\phi = 90°$

Figure 4.13: Measured H-polarization active reflection coefficient for element [8,8] in the 16 x 16 Horus antenna array based on the mutual coupling measurements shown in Fig. 4.11. a) Active reflection coefficient in AZ/EL at 2.9 GHz. b) Active reflection coefficient for $\phi = 0°$ across frequencies. c) Active reflection coefficient for $\phi = 45°$ across frequencies. d) Active reflection coefficient for $\phi = 90°$ across frequencies. Note: Dash lines represent a contour of -10 dB and the square box the simulated or expected scanning bandwidth.

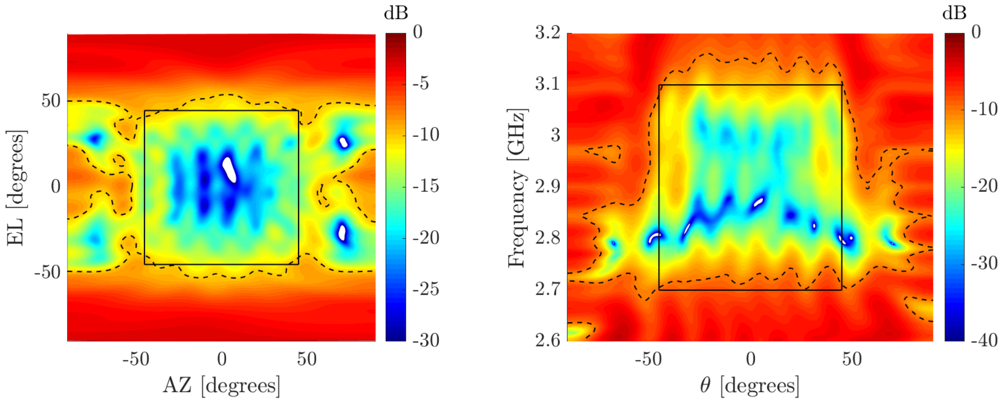

(a) ARC at 5.4 GHz (b) ARC Across Frequencies for $\phi = 0°$

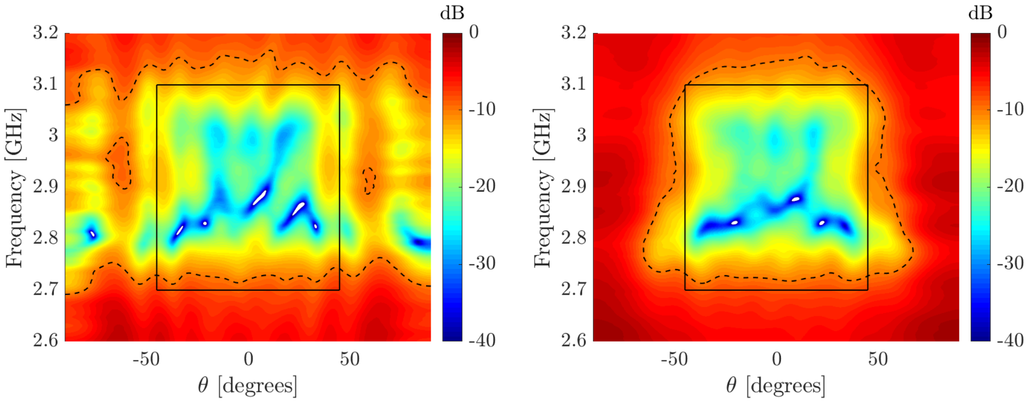

(c) ARC Across Frequencies for $\phi = 45°$ (d) ARC Across Frequencies for $\phi = 90°$

Figure 4.14: Measured V-polarization active reflection coefficient for element [8,8] in the 16 x 16 Horus antenna array based on the mutual coupling measurements shown in Fig. 4.11. a) Active reflection coefficient in AZ/EL at 2.9 GHz. b) Active reflection coefficient for $\phi = 0°$ across frequencies. c) Active reflection coefficient for $\phi = 45°$ across frequencies. d) Active reflection coefficient for $\phi = 90°$ across frequencies. Note: Dash lines represent a contour of -10 dB and the square box the simulated or expected scanning bandwidth.

4.3.2 The PAIR Antenna

The NSF awarded the ARRC a five-year beamforming array project including design, fabrication, and commission of a next generation mobile polarimetric imaging phased array radar [43]. This revolutionary radar platform called PAIR will serve as a scientific tool for studying severe weather phenomena. As a polarimetric imaging radar, PAIR requires a spoiled antenna beam of 20° in EL and 1.5° in AZ, with low cross-polarization in a field of view of ± 45°, and for all frequencies between 5.3 to 5.5 GHz. Due to its limited operational bandwidth and low cross-polarization requirements, the best suited antenna for PAIR is a balanced probe-fed microstrip patch.

A dual-polarized balanced probe-fed microstrip antenna requires 4 drilled vias connected to the patch and referenced to a ground, as shown in chapter 1, Fig. 1.3. In this configuration, only two metallic layers are required. However, the PAIR antenna must include a layer (i.e., metallic layer) for a parasitic microstrip patch and two layers for its feeding network. The parasitic microstrip patch is responsible for increasing the bandwidth of the antenna while the two extra layers for the feeding network to allow for a continuous ground for planar integration. Fig. 4.15 shows the finalized PAIR antenna unit-cell and Fig. 4.16 shows the antenna stackup for manufacturing. The stackup is made of low loss dielectric substrates and adhesives to maximize antenna efficiency and reduce surface waves. The electrical properties of these materials are shown in Table 4.2.

The antenna is excited by a pair of *pogo pins* (i.e., one for H- and one for V-polarization) which are connected to the RF electronics and become flushed when the antenna is mounted. From the *pogo pins*, the signal goes through via V1 establishing connection to the feeding network in L4, as shown

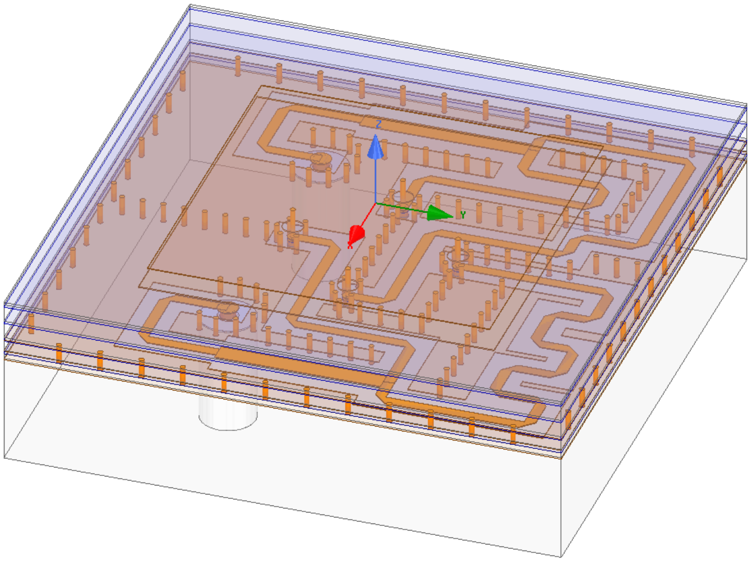

(a) PAIR Antenna Unit-cell

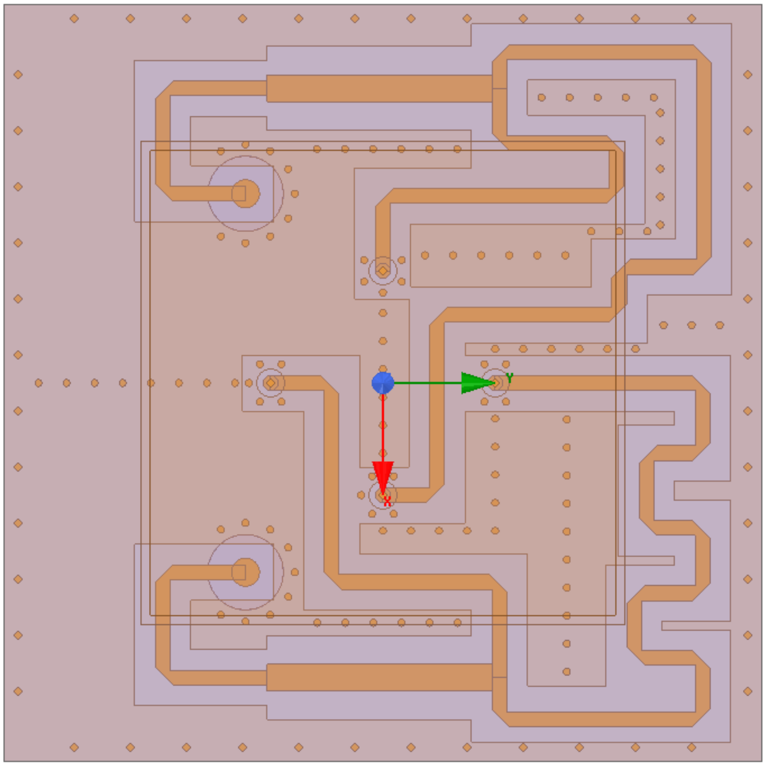

(b) PAIR Antenna Top View

Figure 4.15: Simulated PAIR antenna unit-cell used for simulations in Ansys HFSS. a) PAIR antenna 3D model. b) PAIR antenna top view.

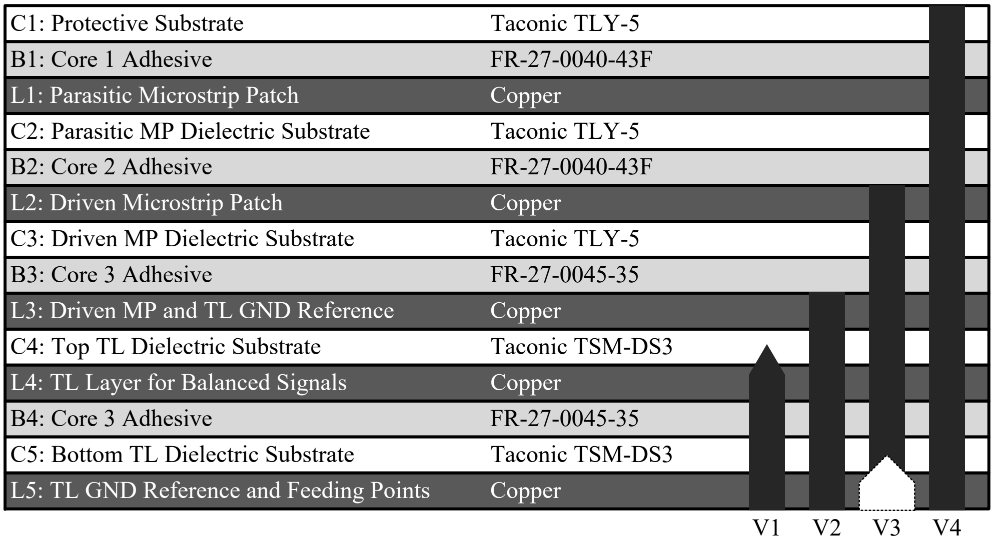

C1: Protective Substrate	Taconic TLY-5
B1: Core 1 Adhesive	FR-27-0040-43F
L1: Parasitic Microstrip Patch	Copper
C2: Parasitic MP Dielectric Substrate	Taconic TLY-5
B2: Core 2 Adhesive	FR-27-0040-43F
L2: Driven Microstrip Patch	Copper
C3: Driven MP Dielectric Substrate	Taconic TLY-5
B3: Core 3 Adhesive	FR-27-0045-35
L3: Driven MP and TL GND Reference	Copper
C4: Top TL Dielectric Substrate	Taconic TSM-DS3
L4: TL Layer for Balanced Signals	Copper
B4: Core 3 Adhesive	FR-27-0045-35
C5: Bottom TL Dielectric Substrate	Taconic TSM-DS3
L5: TL GND Reference and Feeding Points	Copper

Figure 4.16: PAIR antenna stackup and via configuration with the following substrate thicknesses (all in mils): C1 - 5, B1 - 3.5, L1 - 1.4, C2 - 30, B2 - 3.5, L2 - 2, C3 - 30, B3 - 5.6, L3 - 2, C4 - 20, L4 - 1.4, B4 - 5.6, C5 = 10, L5 - 3.1. Note 1: C = Substrate Core, B = Bondply or Prepreg, and L = Copper Layer. Note 2: V1 - controlled depth via, V2 - normal GND via, V3 - backdrilled via for signals, V4 - non-plated via for antenna mounting.

Table 4.2: Substrates integrated in the PAIR antenna design and their respective electrical properties.

Material	**Dielectric Constant** (ϵ_r)	**Tangent Loss** ($\tan\delta$)
Taconic TLY-5	2.2	0.0009
Taconic TSM-DS3	3.0	0.0011
FR-27-0040-43F	2.77	0.0014
FR-27-0045-35	2.74	0.0014

in Fig. 4.16. The feeding network is made from a reactive balun that has an input impedance of 50 Ω. It then goes through a $\lambda_{eff}/4$ transformer which splits into two 50 Ω TLs to produce differential feeding (i.e., 0° and 180° signal references). At the end of these TLs, the signals connect to via V3 which makes the final contact to the driven patch in L2. Via V3 gets backdrilled at the end of production to break their connection with L5 leaving a short stub considered in simulations. Vias V2 are used throughout the unit-cell to improve H/V isolation while vias V4 serve for mounting the antenna to the *pogo pins* plate. Please refer to Appendix B.2 for antenna element mirroring and excitation in the manufactured array.

Simulated Results at Boresight

The PAIR antenna unit-cell follows design guidelines of balanced probe-fed microstrip patch antennas shown in [20], [83], [84]. However, due to the complexity of the unit-cell, is not practical to offer the reader a comprehensive list of the via positions, lengths of each TL segment, dimensions for clearances around the feeding network, or via dimensions. It is rather more insightful to show the dimensions of the antenna radiating sources and unit-cell assuming

Table 4.3: PAIR antenna dimensions.

Dimension	**Variable**	**Length [mm]**
Feeding Position	f_p	4
Parasitic Patch	L_{pp}	16.575
Driven Patch	L_p	17.225
Unit-Cell Size	$d_x = d_y$	27

the feeding network is independently designed from the antenna [20]. Table 4.3 shows the dimensions of the square patches (i.e., parasitic (L_{pp} and driven L_p), the distance of the feeding vias from the center (f_p), and the unit-cell size (d_x and d_y).

Surface wave analysis for the unit-cell considering dielectric substrates above ground layer L3 yields a $\beta_{sw} = 1.0082$, which translates to surface wave scan blindness at 77.28°, as shown in Fig. 4.17. These results show that no scanning blindness are introduced in the antenna's field of view (i.e., $\theta_s = \pm\ 45°$). Fig. 4.22a and Fig. 4.22b show the simulated active S-parameters and realized gain at boresight for H- and V-polarizations using the infinite array approach in HFSS. It is clear that both polarizations exhibit very similar ARC results with an overall %BW of 7.7% while their isolation is lower than -50 dB, as shown in Fig. 4.22a. These same results conduce to highly efficient realized gains at boresight when compared to the theoretical gain of the unit-cell shown in Fig. 4.22b.

Simulated Results when Scanning

The PAIR antenna unit-cell is evaluated across multiple scanning directions to extract the ARC and radiation patterns at a frequency of 5.4 GHz. Note

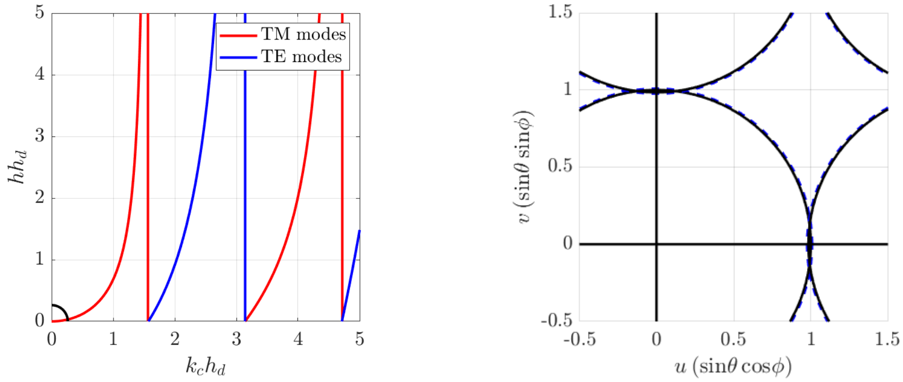

(a) Surface Wave Propagation Analysis (b) Grating Lobe Diagrams

Figure 4.17: Surface wave propagation constant analysis and grating lobe diagrams at 5.6 GHz for the PAIR antenna stackup where $\epsilon_r \approx 2.29$ and $h_d \approx 77.6$ mil. a) Surface wave propagation constant analysis where the ϵ_r calculated based on a weighted average. b) Grating lobe location is moved from 79.78° to 77.28°.

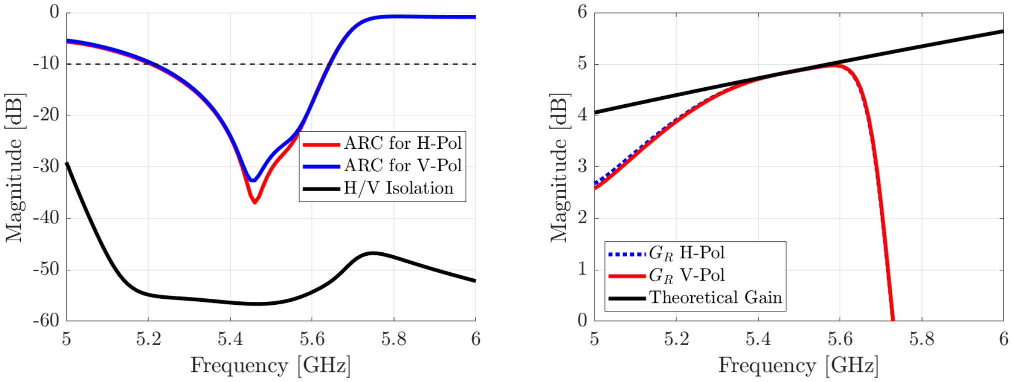

(a) Active S-Parameters (b) Realized Gain

Figure 4.18: Simulated active S-parameters and realized gain at boresight based on infinite array analysis in HFSS. a) Active S-parameters for H- and V-polarization. b) Realized gain for H- and V-polarization.

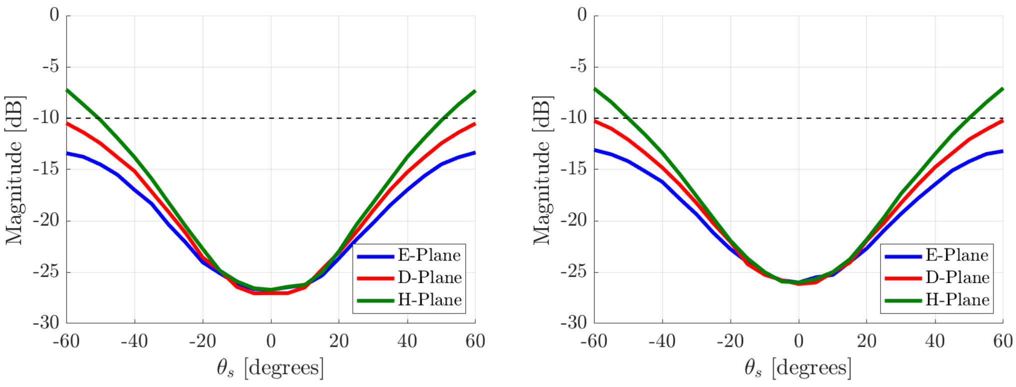

(a) H-Pol ARC

(b) V-Pol ARC

Figure 4.19: Simulated active reflection coefficient cuts for *E*-, *D*-, and *H*-plane at 5.4 GHz. a) H-polarization ARC. b) V-Polarization ARC.

that every desired scanning beam requires a different simulation. Fig. 4.19a and Fig. 4.19b shows the scanning ARC for *E*-, *D*-, and *H*-plane for H- and V-polarization for $\theta = \pm\ 60°$ with a resolution of 5°. The antenna is capable of scanning at this frequency up to ± 50° in all planes and polarizations, maintaining an ARC below -10 dB. In fact, the PAIR antenna could continue scanning on the *E*- and *D*-plane further than $\theta = 50°$ at the expense of a reduced realized gain.

Fig. 4.20 shows the normalized radiation patterns in Ludwig's third definition of polarization for the aforementioned planes. As well as in the ARC, the co-polarization patterns for H- and V- are very similar with co-polarization differences lower than 0.2 dB between *E*- and *H*-plane for $\theta = \pm\ 45°$. In terms of cross-polarization, *E*- and *H*-plane show levels of -40 dB within $\theta = \pm\ 45°$. The *D*-plane in the other hand shows the same cross-polarization for $\theta = \pm\ 20°$. According to these results, the PAIR antenna satisfies the phased array requirements for polarimetric measurements in terms of co- and

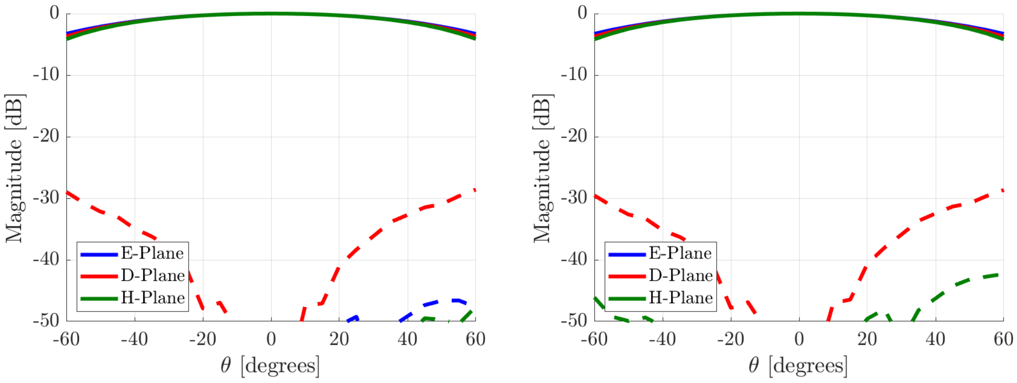

(a) H-Pol Radiation Pattern Cuts (b) V-Pol Radiation Pattern Cuts

Figure 4.20: Simulated normalized radiation pattern cuts for *E*-, *D*-, and *H*-plane based on Ludwig's third definition of polarization at 5.4 GHz. a) H-polarization radiation patterns cuts. b) V-Polarization radiation pattern cuts.

cross-polarization at this frequency.

Measured Results at Boresight

The performance of the PAIR antenna is validated through the mutual coupling measurements of a central element in the array discussed in Section. 2.2.2. The manufactured antenna is made from 64 elements distributed on an 8 x 8 grid. The element reference for these measurements is [4,5], where the first number in the brackets indicate column position and the second, row position. The antenna was setup in a small anechoic chamber and measurements were gathered with a 2-port network analyzer. One port of the network analyzer was left connected throughout the course of the measurements to a reference polarization (i.e., H- or V-polarization) while the other was moved to measure the couplings to all other elements. Fig. 4.21 shows the results of these measurements for H- and V-polarization at 5.4 GHz. Note that for the reference element, the shown coupling is for the passive self-reflection of the measured

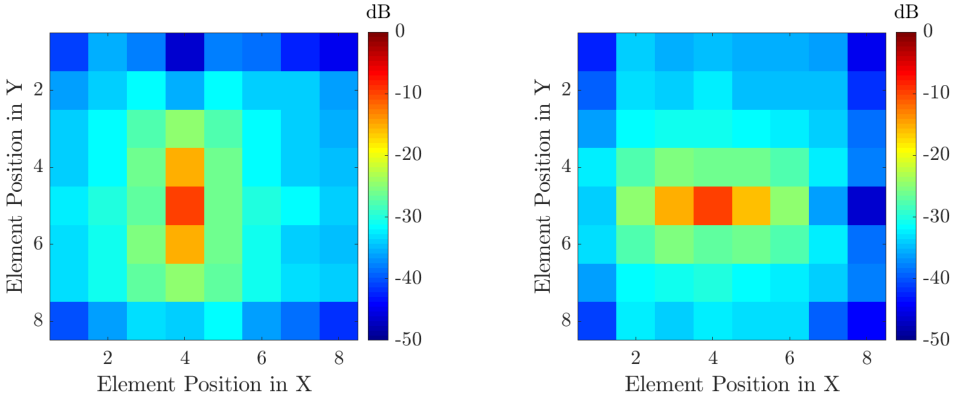

(a) Mutual Coupling for H-Pol (b) Mutual Coupling for V-Pol

Figure 4.21: Mutual coupling measurements for H- and V-polarizations for element [4,5] in the 8 x 8 PAIR antenna array at 5.4 GHz. a) Mutual coupling measurements for H-polarization. b) Mutual coupling measurements for V-polarization.

polarization. Each set of measurements exhibits very similar results with higher couplings present along their respective polarization directions.

Fig. 4.22 shows the ARC at boresight as well as the realized gain for both polarizations, using the coupling measurements shown in Fig. 4.21. The calculated ARC through the mutual coupling measurements shows excellent agreement with the simulated unit-cell. It is unclear at this point if the discrepancies between H- and V-polarization in the ARC are due to measurement errors (i.e., cable phase and calibration stability throughout the measurements) or intrinsic differences in the manufactured geometry.

Measured Results when Scanning

Figs. 4.23 and 4.24 show the scanning ARC for H- and V-polarization as a function of scanning angle θ/ϕ or AZ/EL and operational frequencies using the mutual coupling results shown in Fig. 4.21. The antenna sustains for both polarizations an ARC below -10 dB within the required AZ/EL range.

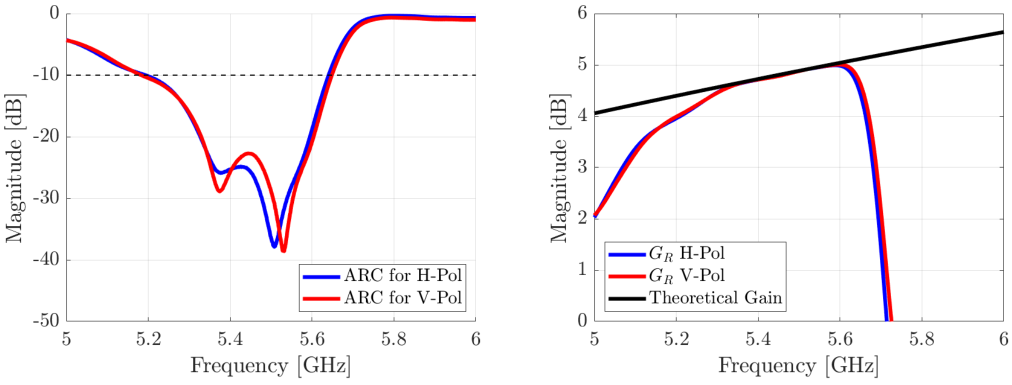

(a) Active S-Parameters (b) Realized Gain

Figure 4.22: Measured ARC and realized gain at boresight for element [4,5] in the 8 x 8 PAIR antenna array based on the mutual coupling measurements shown in Fig. 4.21. a) Active S-parameters for H- and V-polarization. b) Realized gain for H- and V-polarization.

Moreover, the antenna also sustains an ARC below -10 dB for all designed frequencies in ϕ cuts 0°, 10°, and 90°. However, some of these results might prove misleading to the reader.

Figs. 4.23d and 4.24b show ARCs lower than -10 dB for $\theta = \pm\ 90°$ in frequency ranges between 5.5 and 5.6 GHz. These results are misleading because the antenna couplings are truncated to the size of the manufactured array (i.e., 8 x 8) which results in anomalies in the calculated ARC for grazing angles. To obtain more accurate results for angles near grazing, the size of the array has to be increased. Unfortunately, at the time of this work there was no plans on measuring a bigger array because the obtained results were sufficient to validate the performance of the antenna against simulations.

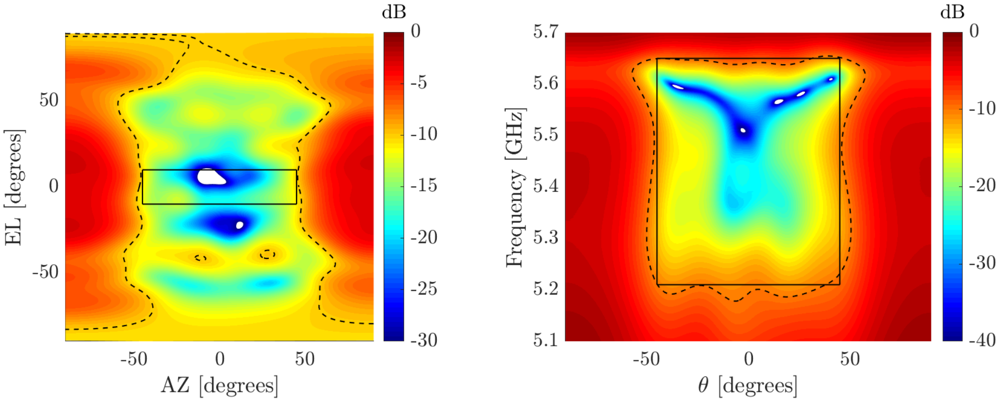

(a) ARC at 5.4 GHz

(b) ARC Across Frequencies for ϕ = 0°

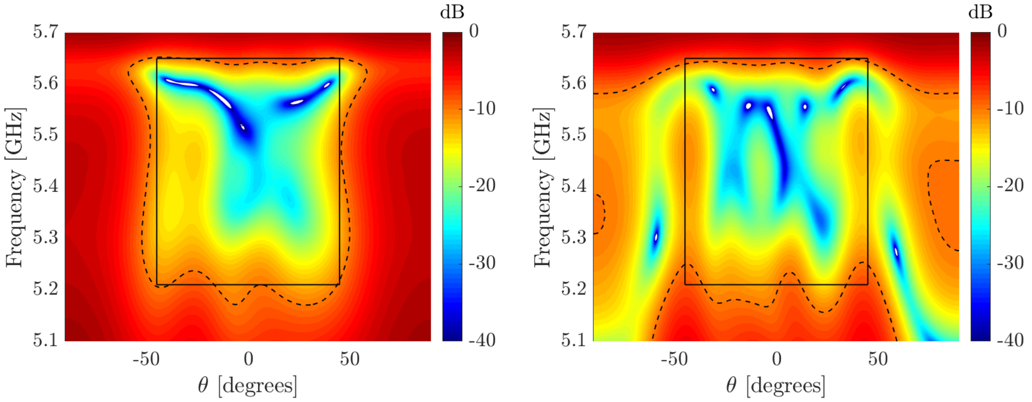

(c) ARC Across Frequencies for ϕ = 10°

(d) ARC Across Frequencies for ϕ = 90°

Figure 4.23: Measured H-polarization active reflection coefficient for element [4,5] in the 8 x 8 PAIR antenna array based on the mutual coupling measurements shown in Fig. 4.21. a) Active reflection coefficient in AZ/EL at 5.4 GHz. b) Active reflection coefficient for $\phi = 0°$ across frequencies. c) Active reflection coefficient for $\phi = 10°$ across frequencies. d) Active reflection coefficient for ϕ = 90° across frequencies. Note: Dash lines represent a contour of -10 dB and the square box the simulated or expected scanning bandwidth..

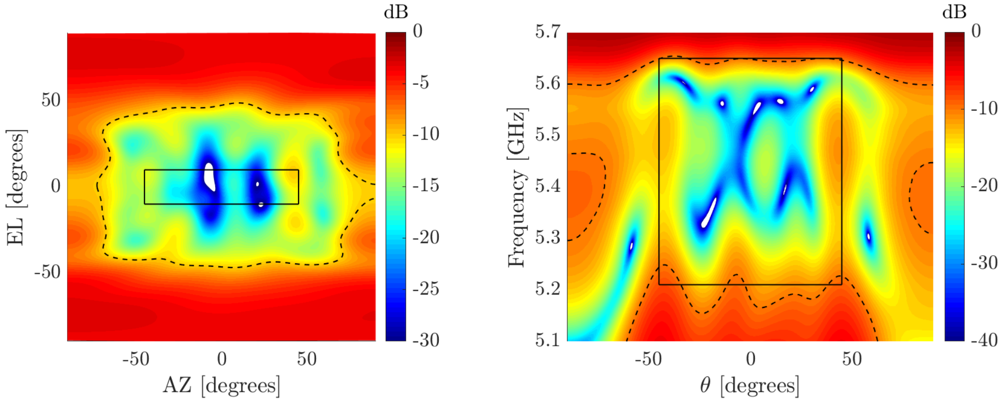

(a) ARC at 5.4 GHz

(b) ARC Across Frequencies for ϕ = 0°

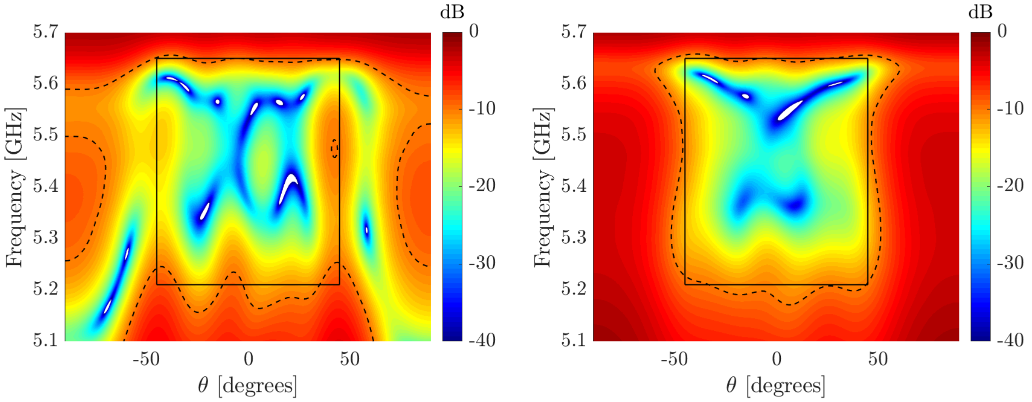

(c) ARC Across Frequencies for ϕ = 10°

(d) ARC Across Frequencies for ϕ = 90°

Figure 4.24: Measured V-polarization active reflection coefficient for element [4,5] in the 8 x 8 PAIR antenna array based on the mutual coupling measurements shown in Fig. 4.21. a) Active reflection coefficient in AZ/EL at 5.4 GHz. b) Active reflection coefficient for ϕ = 0° across frequencies. c) Active reflection coefficient for ϕ = 10° across frequencies. d) Active reflection coefficient for ϕ = 90° across frequencies. Note: Dash lines represent a contour of -10 dB and the square box the simulated or expected scanning bandwidth..

4.3.3 The Horus-ONR Antenna

The Horus-ONR antenna was designed out of a need of higher bandwidth capabilities out of the current Horus system. When compared, the Horus-ONR antenna has both sub-assemblies made from Taconic TLY-5Z and FR-27-0045-35, allowing the dielectric stackup above the antenna ground plane to achieve a lower effective dielectric constant. The result of this approch makes the Horus-ONR antenna achieve larger bandwidths at the expense of higher cross-polarized radiation. The Horus-ONR antenna exhibits a %BW of 24.85%, representing nearly a 10% bandwidth increase over the Horus antenna. Due to the similarities between both antennas, the results of the Horus-ONR antenna are limited here to simulation and measurements at boresight for validation, as shown in Fig. 4.25.

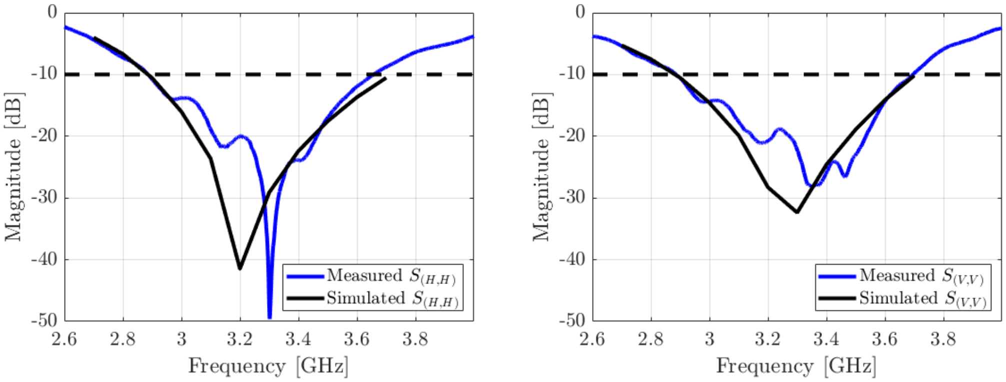

(a) H-Polarization at Boresight

(b) V-Polarization at Boresight

Figure 4.25: Simulated and measured active reflection coefficient at boresight for Horus-ONR antenna. a) H-polarization at boresight. b) V-polarization at boresight.

4.4 Summary

All designed and manufactured antennas for dual-polarized phased array radars requiring low cross-polarization and well-matched co-polarized beams were discussed in this Chapter. Section 4.2 covered all relevant microstrip patch antenna design trade-offs including: surface waves, bandwidth, isolation, cross-polarization, and efficiency. It was shown that surface waves, bandwidth, and efficiency are directly related in the design of microstrip patch antennas and that isolation and cross-polarization can be optimized at the array or element level. Section 4.3 discussed next generation phased array radar antennas including Horus, PAIR, and Horus-ONR antennas. In Section 4.3.1, the design guidelines for the Horus antenna were discussed where simulation and measured results show very good agreement. It was mentioned that even though the Horus antenna do not satisfy the cross-polarization requirements for STSR, its design makes it one of the most calibratable antenna elements for weather polarimetry over the required bandwidth. Section 4.3.2 covered the design of the PAIR antenna for which all imaging phased array requirements were satisfied with nearly equal H/V polarization responses. Lastly, Section 4.3.3 covered the results of the Horus-ONR antenna where the bandwidth capabilities of the Horus Antenna were extended over 10%. This antenna required to trade cross-polarization performance for higher bandwidths leaving the polarimetry to rely more over calibration.

Chapter 5

The Ultra-Low Cross Polarization Microstrip Patch Antenna (ULCP-MPA)

5.1 Introduction

The ULCP microstrip patch antenna design roots from the electric current model discussed in Section 3.5.1. It was proved that microstrip patch antennas have the capability of producing cross-polarization below -40 dB and IXR greater than 33 dB (i.e., in Ludwig's third definition of polarization) in the visible region defined by $-45^\circ \le \theta \le 45^\circ$. To do so, very specific conditions are required for the dielectric supporting the microstrip patch. In this chapter we explore how these theoretical findings can be integrated into a practical phased array antenna design.

5.1.1 ULCP Antenna Requirements

The ULCP microstrip patch antenna requires a substrate with a dielectric constant ≈ 1.7 and thickness less than 0.01λ, to produce cross-polarization levels of -40 dB, as shown in Fig. 5.1. Unfortunately, there is no commercially available substrate with these characteristics. In fact, the lowest dielectric constant in a comercially available substrate is 2.0 and it is made by Rogers

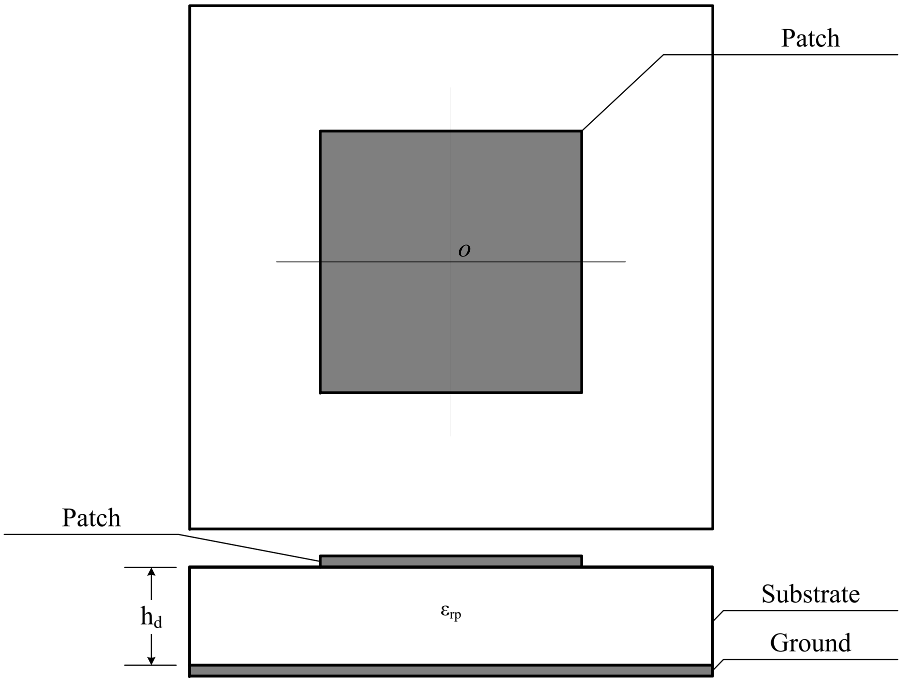

Figure 5.1: Top and side view of the theoretical ULCP microstrip antenna where $h_d \leq 0.01\lambda$ and $\epsilon_{rp} \approx 1.7$ to produce cross-polarization levels of -40 dB. The dielectric covered ground extends horizontally to infinity.

Corporation (Rogers 5880LZ). The ULCP model also assumes no feeding network exciting the microstrip patch. Thus, to design a practical ULCP antenna, one would need to engineer a substrate with a dielectric constant of 1.7 with thickness of 0.01λ and feeding network that does not interact with microstrip patch.

5.1.2 Proposed ULCP Antenna Architecture

Dielectric Substrate

Let us consider the substrate requirement underneath the microstrip patch with dielectric constant of 1.7 and thickness of 0.01λ. This requirement can be

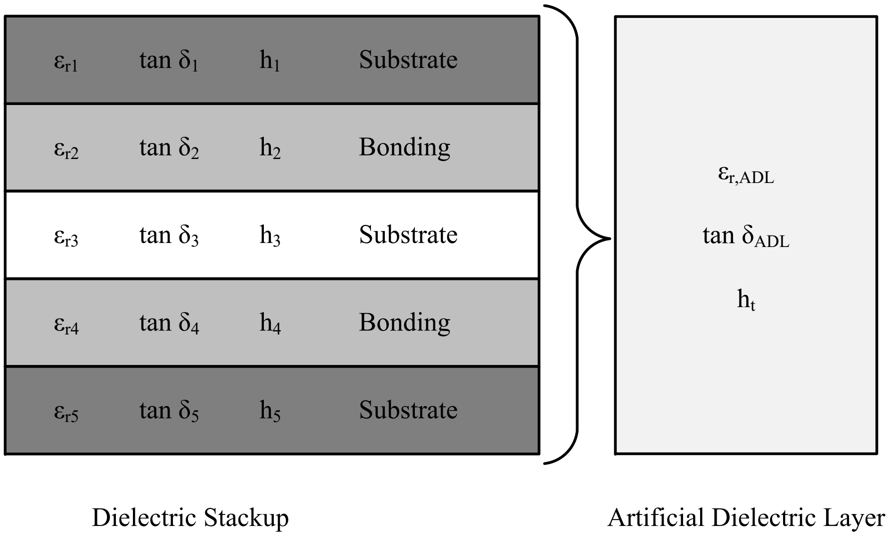

Figure 5.2: Side view of the proposed dielectric stackup to design an ULCP microstrip antenna where ϵ_{rN} refers to the permittivity of the dielectric N, $\tan\delta_N$ to the tangent loss of the dielectric N, and h_N to the height of the dielectric N. For the ADL: $\epsilon_{r,ADL}$ refers to the effective permittivity, $\tan\delta_{ADL}$ to the effective tangent loss, and h_t to the total dielectric height.

satisfied by using an artificial dielectric layer (ADL). The ADL, in the context of this work, is a combination of multiple substrates with different electrical and physical properties that when combined, behaves as a single homogeneous substrate. Its effective electrical properties can be predicted using circuit model equivalents [85], full wave simulations [86], or by simple weighted averages [54]. Fig. 5.2 shows our proposed ADL to satisfy the requirements of the ULCP microstrip patch antenna. The effective electrical characteristics of the ADL are controlled by the thicknesses and electrical properties of the dielectric stackup. The selection process of the materials is mathematically simplified by setting layers 1 and 5 equal as well as layers 2 and 4, which conveniently makes the stackup symmetrical. The effective permittivity and tangent loss for the ADL using a weighted average is found from,

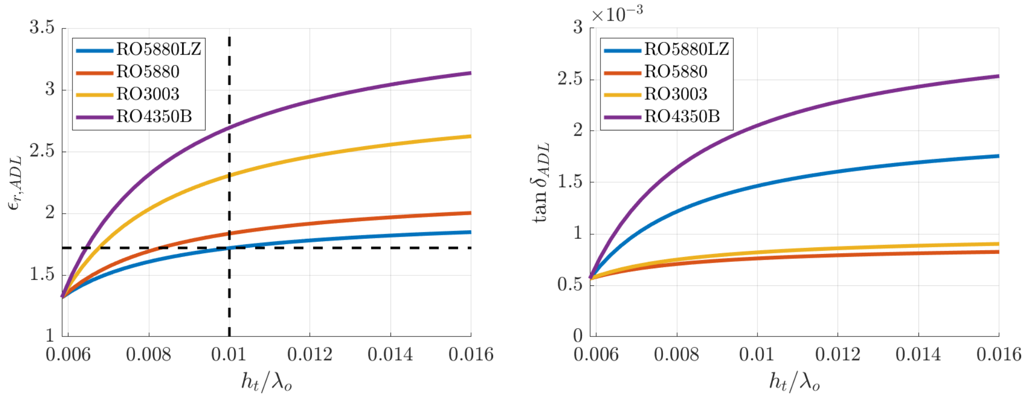

(a) ADL Dielectric Permittivity (b) ADL Tangent Loss

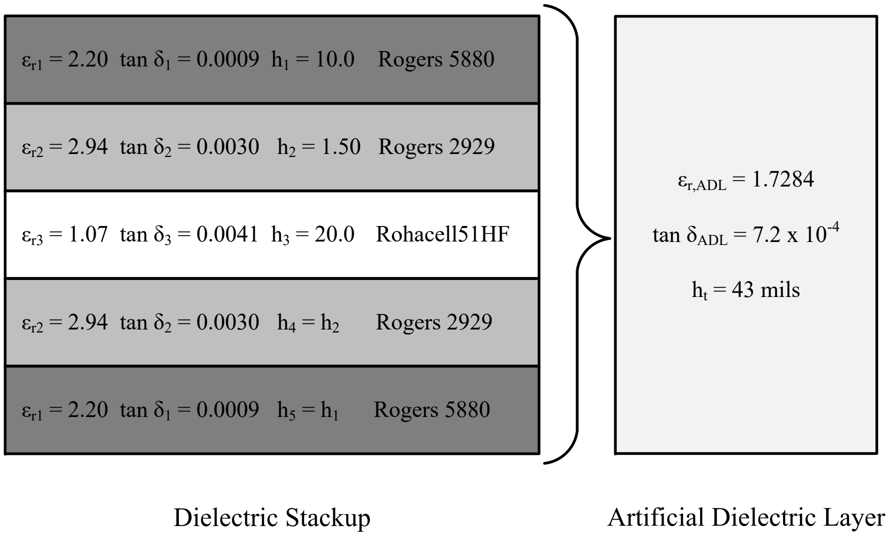

(c) ADL for ULCP Microstrip Patch Antenna

Figure 5.3: Effective electrical properties for the proposed ADL. Calculated effective permittivity (a) and tangent loss (b) for ADLs made out of Rogers 5880LZ, RO5880, RO3003, or RO4350B using Rogers 2929 as bonding and Rohacell 51-HF in the middle core with thicknesseses of 1.5 and 20 mils, respectively. c) Proposed ADL for an ULCP microstrip patch antenna.

$$\epsilon_{r,ADL} = 2\frac{h_1\epsilon_{r1}}{h_t} + 2\frac{h_2\epsilon_{r2}}{h_t} + \frac{h_3\epsilon_{r3}}{h_t}, \tag{5.1}$$

and

$$\tan\delta_{ADL} = 2\frac{h_1\tan\delta_1}{h_t} + 2\frac{h_2\tan\delta_2}{h_t} + \frac{h_3\tan\delta_3}{h_t}, \tag{5.2}$$

where $h_t = 2h_1 + 2h_2 + h_3$. Comercially available, low permittivity dielectrics are chosen for layers 1 through 5. Layer 1, 3, and 5 are made out of solid substrate cores while 2 and 4 are used as bonding layers. To bring the effective permittivity lower than the values provided by commercially available dielectrics used on layers 1 and 2, a layer of high density foam is used in layer 3. Fig. 5.3a and 5.3b show the calculated effective permittivity and tangent loss as a function of substrate height for multiple ADLs made out of commercially available dielectrics (Rogers 5880LZ, Rogers 5880, Rogers 3003, Rogers 4350B) when using 2 bonding layers of Rogers 2929 and foam core of Rohacell 51-HF. It can be seen that all ADLs exhibit dielectric constants of 1.7 but at different substrate heights. RO3003 and RO4350B require thicknesses lower than 4 mils which are not commercially available. RO5880 and RO5880LZ require 10 and 17 mils, respectively, which can be found commercially. For this reason, an ADL made from RO5880 or RO5880LZ is more suitable to simultaneously satisfy the thickness and permittivity requirements of the ULCP microstrip patch antenna. The finalized stackup for the proposed ADL using RO5880 are shown in Fig. 5.3c, where $\epsilon_{r,ADL} = 1.7284$, $\tan\delta_{ADL} = 7.2\times10^{-4}$, and $h_t =$ 43 mils.

Feeding Network

The ULCP antenna model, as shown in Fig. 5.1, has no feeding network exciting the microstrip patch. This requirement can be partially satisfied by using a non-contact microstrip excitatation such as an aperture or proximity coupling. The proximity coupling exposes a TL underneath the microstrip patch that can introduce sporious radiation in the antenna. The aperture coupling technique, in the other hand, introduces a slot in the ground underneath the microstrip patch keeping the fields symmetrical. For this reason, the aperture coupling technique is the proposed feeding mechanism to be used in practical ULCP microstrip patch antennas. For more details about non-contact feeding mechanisms for microstrip patch antennas please refer to Section 1.3.2.

ULCP Microstrip Antenna

The proposed ULCP microstrip patch antenna using an ADL and a non-contact feeding technique is shown in Fig. 5.4, where $\epsilon_{r,ADL}$ refers to the effective dielectric constant of the ADL and h_t to its thickness. The patch and the slot has a length and a width dimensions of L_p/W_p and L_s/W_s. The TL is mounted in a substrate with dielectric constant ϵ_{rf} and thickness h_f. Finally, the TL has a width W_t and stub length L_{stub}. Using the results for the proposed ADL and patch dimensions $L_p = W_p = 38.2$ mm, the ULCP model predicts radiation patterns shown in Fig. 5.5. It can be seen that the model predicts cross-polarization levels below -40 dB for $-49^\circ \leq \theta \leq 49^\circ$. However, the model does not account for the presence of the slot or its radiation, the TL, and real ADL stackup. Nevertheless, these results serve as a guide for comparing the cross-polarization obtained through simulation tools. In Section 5.2, the proposed ULCP microstrip antenna is simulated using Ansys HFSS to

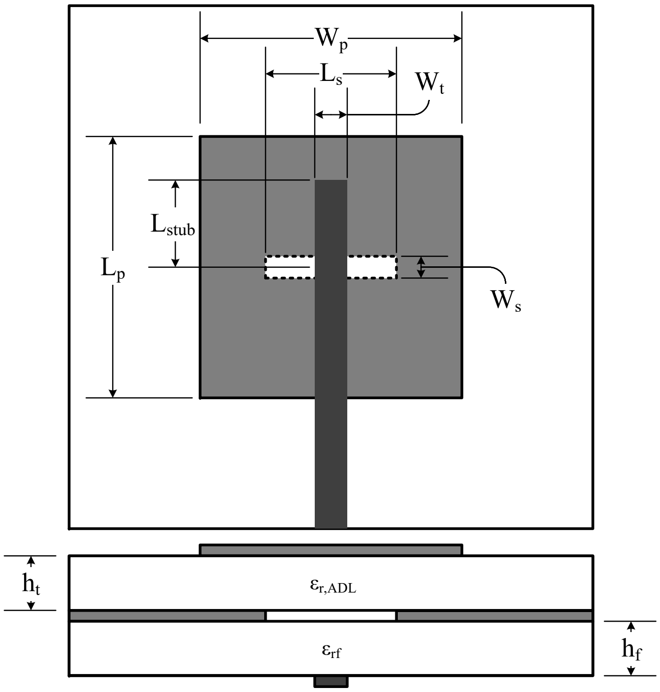

Figure 5.4: Top and side view of the proposed ULCP microstrip patch antenna, where $\epsilon_{r,ADL}$ refers to the effective dielectric constant of the ADL and h_t to its thickness, as shown in Fig. 5.3. L_p and W_p refer to the length and width of the microstrip patch. L_s and W_s refer to the length and the width of the coupling aperture. The feed has a substrate with dielectric constant of ϵ_{rf} and thickness h_f, while the transmission line has width W_t and stub length L_{stub}.

account for the effects of the slot, TL, and real ADL stackup.

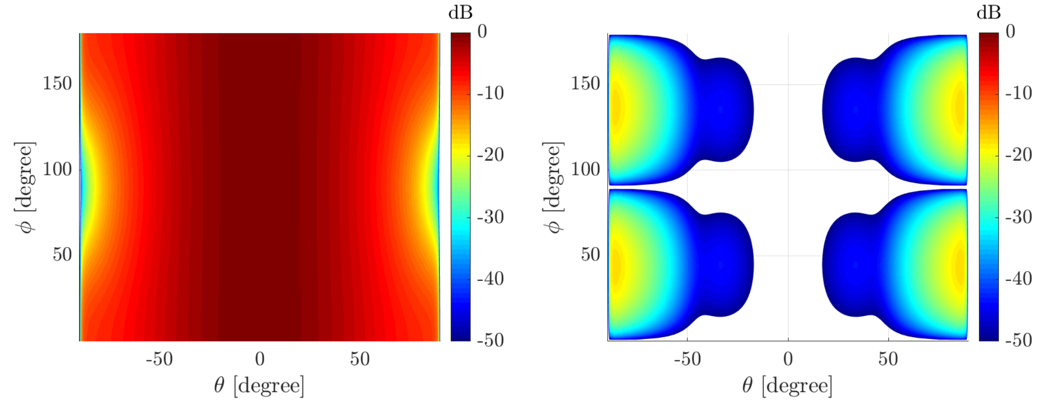

(a) Co-polarization (b) Cross-polarization

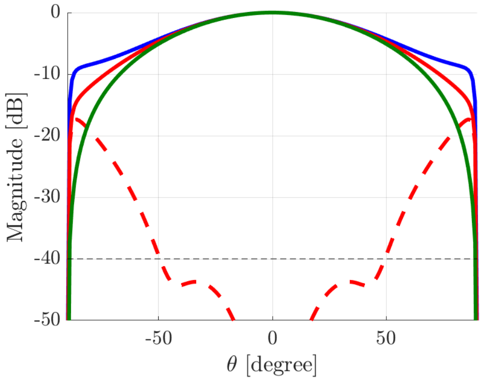

(c) Co- and Cross-polarization Cuts

Figure 5.5: Mathematically modeled ULCP microstrip patch antena radiation patterns based on Ludwig's third definition of polarization. The inputs for the model were: $\epsilon_{r,eff} = 1.7284$, $h_d = 43$ mils, $L_p = W_p = 38.2\ mm$. a) Two-dimensional co-polarized radiation pattern. b) Two-dimensional cross-polarized radiation pattern. c) Co- and cross-polarized radiation pattern cuts for E- (blue), D- (red), and H-plane (green).

5.2 ULCP Antenna Modeling

This section presents the simulated results of the proposed ULCP microstrip patch antenna using Ansys HFSS. In Sections 5.2.1 and 5.2.2, HFSS Method of Moments (MoM) is used for simulations which assumes infinite extension of the dielectric covered ground in the antenna design. Consequentaly, this method serves as a great tool for comparing the results obtained through the mathematical model shown in Section 5.1.2. In Sections 5.2.3 through 5.2.5, HFSS Finite Element Method (FEM), with Infinite Array Approach (IAA) is used for predicting the performance of the antenna in a planar phased array. Hereinafter, all guidelines regarding unit cell size, antenna excitation, floquet port excitations, and boundary conditions are followed for HFSS MoM and IAA.

5.2.1 MoM: Homogeneous Substrate

The ULCP microstrip patch antenna with a homogeneous substrate is setup in HFFS MoM using the dimensions shown in Fig. 5.4, where: $L_p = W_p = 35.9$ mm, $L_s = 9.5$ mm, $W_s = 1$ mm, $W_t = 1.74$ mm, $L_{stub} = 12$ mm, $\epsilon_{rf} = 3.66$, and $h_f = 30$ mils. For substrate stackup details see Fig. 5.6a. Notice that the TL has a characteristic impedance of 50 Ω which allows for the integration of a vertical SMA connector. Fig. 5.6b shows the expected BW of the ULCP microstrip patch antenna. It can be seen that the antenna has a narrow BW of 33 MHz which corresponds to a %BW of 1.1%. In the other hand, the antenna shows sustained cross-polarization levels under -40 dB for $-50° \leq \theta \leq 50°$, as shown in Fig. 5.6c. Unfortunately, is rather difficult to quantify the cross-polarization contribution of the feeding network (i.e., slot, TL, and TL dielectric) to the antenna but, is clear that the boresight null is missing when compared to the mathematical model results (see Fig. 5.5). Nevertheless, the results show that a substrate with a dielectric constant of ≈ 1.7 allows microstrip patch antennas ultra-low cross-polarization characteristics.

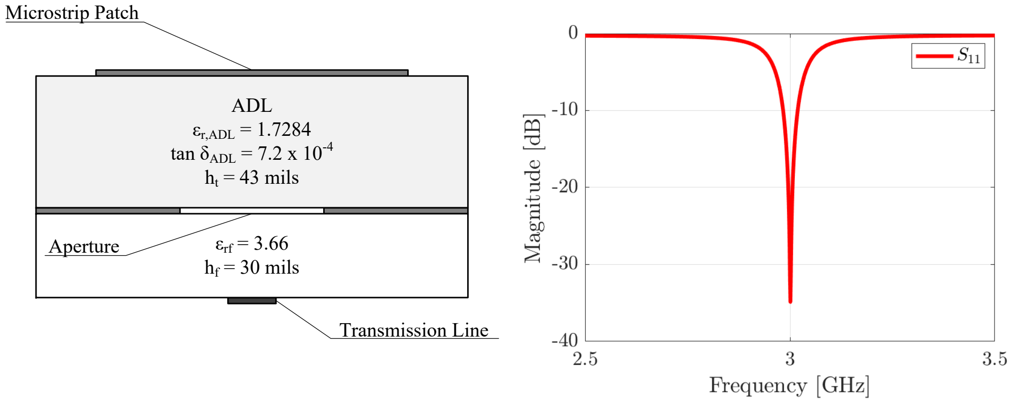

(a) Antenna Stackup Properties

(b) Reflection Coefficient

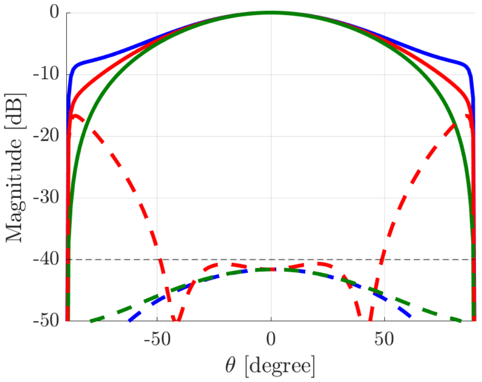

(c) Co- and Cross-polarization Radiation Patterns

Figure 5.6: Simulated (MoM) results for the proposed ULCP microstrip patch antenna using a homogeneous substrate. a) Antenna stackup properties. b) Reflection coefficient of the antenna. c) Co- and cross-polarization radiation patterns based on Ludwig's third definition of polarization for *E*- (blue), *D*- (red), and *H*-plane (green).

5.2.2 MoM: ADL Stackup

The ULCP microstrip patch antenna with the proposed ADL is setup in HFFS using MoM and the dimensions shown in Fig. 5.4, where: $L_p = W_p =$ 38.2 mm, $L_s = 9.5$ mm, $W_s = 1$ mm, $W_t = 1.74$ mm, $L_{stub} = 12$ mm, $\epsilon_{rf} =$ 3.66, and $h_f = 30$ mils. For ADL stackup details see Fig. 5.7a. Notice that the patch size increased by 2.3 mm, but is the only physical property that changed from the previous results (i.e., ULCP Antenna - MoM Homogeneous Substrate). This difference can be explained by the prescence of the low dielectric constant foam. The foam allows for the fringing fields to extend further because the ADL is not electrically homogeneous to the microstrip patch. Fig. 5.7b shows the expected BW of the ULCP microstrip patch antenna. It can be seen that the antenna has a narrow BW of 34 MHz which corresponds to a %BW of 1.1%. In the other hand, the antenna shows sustained cross-polarization levels under -40 dB for $-58^\circ \leq \theta \leq 58^\circ$, as shown in Fig. 5.6c. These results have shown that an ULCP microstrip patch antenna design is possible using an ADL with aperture coupling.

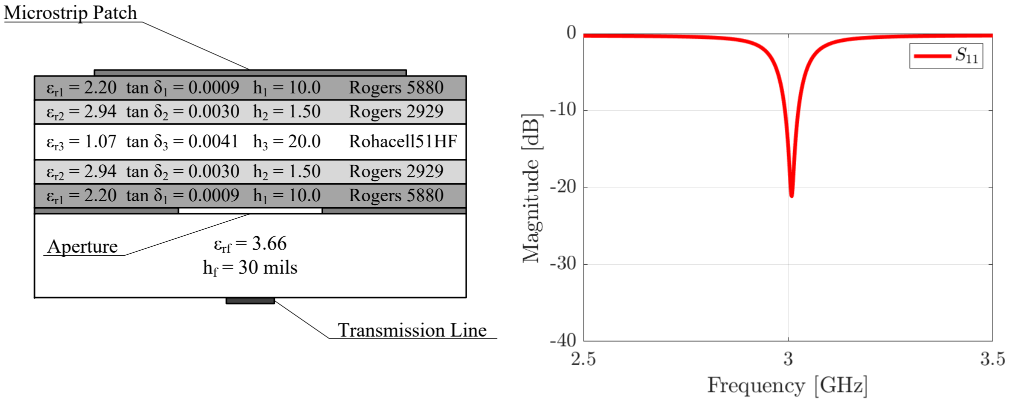

(a) Antenna Stackup Properties

(b) Reflection Coefficient

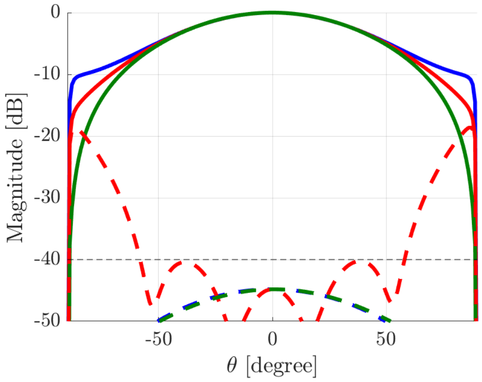

(c) Co- and Cross-polarization Radiation Patterns

Figure 5.7: Simulated (MoM) results for the proposed ULCP microstrip patch antenna using the proposed ADL. a) Antenna stackup properties. b) Reflection coefficient of the antenna. c) Co- and cross-polarization patterns based on Ludwig's third definition of polarization for *E*- (blue), *D*- (red), and *H*-plane (green).

5.2.3 IAA: Homogeneous Substrate

The ULCP microstrip patch antenna with a homogeneous substrate is setup in HFFS FEM using a $\lambda/2$ unit cell and dimensions shown in Fig. 5.4, where: $L_p = W_p = 34.5$ mm, $L_s = 12$ mm, $W_s = 1$ mm, $W_t = 1.74$ mm, $L_{stub} = 12$ mm, $\epsilon_{rf} = 3.66$, and $h_f = 30$ mils. For substrate stackup details see Fig. 5.8a. Notice that the patch size decreased by 1.3 mm and the slot increased by 2.5 mm, when compared to MoM simulated results shown in Section 5.2.1. This difference can be the result of mutual coupling in the infinite array which results in a loading condition affecting the antenna input impedance. Fig. 5.8b shows the expected BW of the ULCP microstrip patch antenna. It can be seen that the antenna exhibits a higher BW of 74 MHz which corresponds to a %BW of 2.5%. This BW increase in the infinite array simulation is another consequence of the mutual coupling which is usually exploited in ultra wideband antenna designs, as shown in [54]. In terms of polarization, the antenna shows sustained cross-polarization levels under -40 dB for $-46° \leq \theta \leq 46°$, with a well-defined null at boresight, as shown in Fig. 5.8c. Finally, the expected scanning performance or active reflection coefficient (ARC) of the antenna is shown in Fig. 5.8d. It is clear that the antenna sustains an ARC below -10 dB for most of $-45° \leq \theta \leq 45°$ range. In conclusion, these results have shown that a substrate with a dielectric constant of ≈ 1.7 allows microstrip patches ULCP characteristics when used in planar phased arrays.

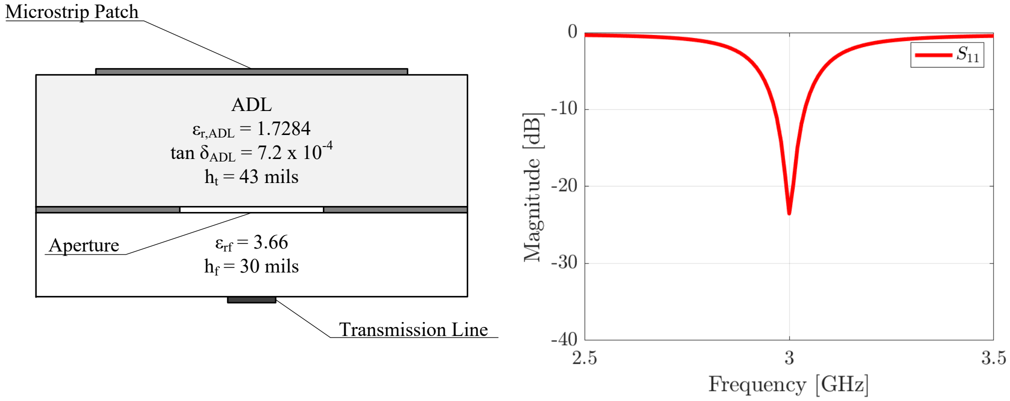

(a) Antenna Stackup Properties (b) ARC at Boresight

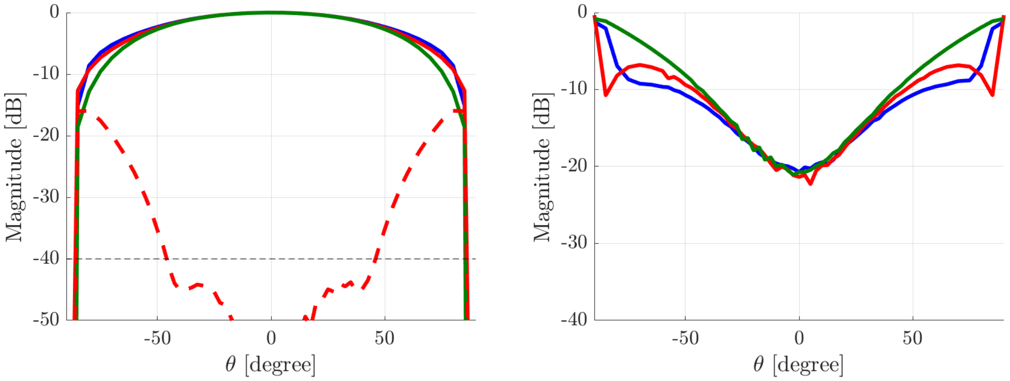

(c) Co- and Cross-polarization Radiation Patterns (d) Scanned ARC

Figure 5.8: Simulated (IAA) results for the proposed ULCP microstrip patch antenna using a homogeneous substrate. a) Antenna stackup properties. b) Reflection coefficient of the antenna. c) Co- and cross-polarization patterns based on Ludwig's third definition of polarization for *E*- (blue), *D*- (red), and *H*-plane (green). d) Scanned active reflection coefficient for *E*-, *D*-, and *H*-plane.

5.2.4 IAA: ADL Stackup

The ULCP microstrip patch antenna with the proposed ADL is setup in HFFS FEM using a $\lambda/2$ unit cell and dimensions shown in Fig. 5.4, where: $L_p = W_p = 36.9$ mm, $L_s = 12$ mm, $W_s = 1$ mm, $W_t = 1.74$ mm, $L_{stub} = 12$ mm, $\epsilon_{rf} = 3.66$, and $h_f = 30$ mils. For substrate stackup details see Fig. 5.9a. Notice that the patch size decreased by 1.3 mm and the slot increased by 2.5 mm, when compared to MoM simulated results shown in Section 5.2.2. This difference can be attributed to the presence of mutual coupling in the infinite array, as it occurred with the homogeneous substrate case. Fig. 5.9b shows the expected BW of the ULCP microstrip patch antenna. It can be seen that the antenna exhibits a BW of 74 MHz which corresponds to a %BW of 2.5%. In terms of polarization, the antenna shows sustained cross-polarization levels under -40 dB for $-20^\circ \leq \theta \leq 20^\circ$, with a well-defined null at boresight, as shown in Fig. 5.9c. This cross-polarization discrepancy between the homogeneous substrate and the ADL simulation can be the result of mutual coupling through the foam layer where the fields are not well confined under the microstrip patch. Nevertheless, the antenna shows an ARC below -10 dB for $-50^\circ \leq \theta \leq 50^\circ$, as illustrated in Fig. 5.9d. These results show that the proposed ADL alone does not allow the microstrip patch antenna to reach ULCP characteristics in a planar phased array. Section 5.2.5 explores a modified ADL that can yield ULCP characteristics in planar phased arrays.

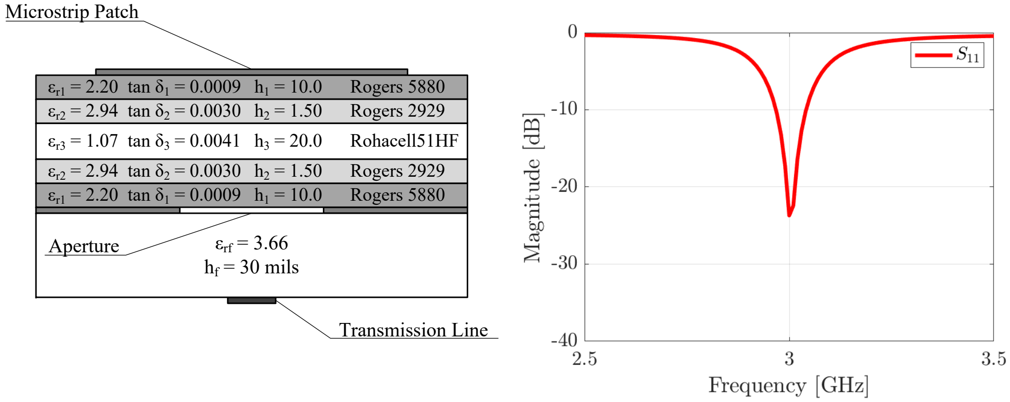

(a) Antenna Stackup Properties

(b) ARC at Boresight

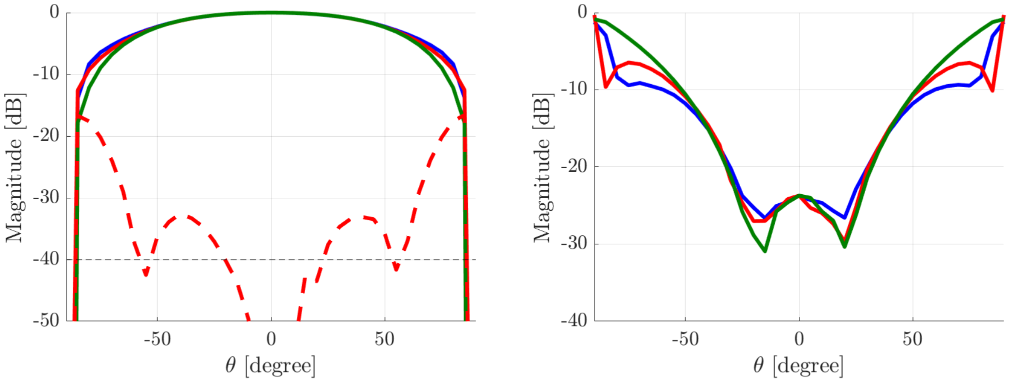

(c) Co- and Cross-polarization Radiation Patterns

(d) Scanned ARC

Figure 5.9: Simulated (IAA) results for the proposed ULCP microstrip patch antenna using the proposed ADL. a) Antenna stackup properties. b) Reflection coefficient of the antenna. c) Co- and cross-polarization patterns based on Ludwig's third definition of polarization for *E*- (blue), *D*- (red), and *H*-plane (green). d) Scanned active reflection coefficient for *E*-, *D*-, and *H*-plane.

5.2.5 IAA: Modified ADL

The ULCP microstrip patch antenna with a modified ADL is setup in HFFS FEM using a $\lambda/2$ unit cell and dimensions shown in Fig. 5.4, where: $L_p = W_p = 35.9$ mm, $L_s = 12$ mm, $W_s = 1$ mm, $W_t = 1.74$ mm, $L_{stub} = 12$ mm, $\epsilon_{rf} = 3.66$, and $h_f = 30$ mils. For substrate stackup details see Fig. 5.10a. Notice that the foam core thickness was reduced by 5 mils which required the patch to be decreased by 1 mm when compared to the previous results (i.e., IAA - ADL Stackup). This stackup modification raised the effective dielectric constant under the patch to 1.81 from ≈ 1.72. Fig. 5.10b shows the expected BW of the ULCP microstrip patch antenna. It can be seen that the antenna exhibits a reduction in BW, allowing 67 MHz which corresponds to a %BW of 2.2%. With this stackup modification, the antenna now exhibits sustained cross-polarization levels under -40 dB for $-52^\circ \leq \theta \leq 52^\circ$, with a well-defined null at boresight, as shown in Fig. 5.10c. Moreover, the antenna shows an ARC below -10 dB for most of $-45^\circ \leq \theta \leq 45^\circ$, as shown in Fig. 5.10d. These results show that the modified ADL allows for the microstrip patch to reach ULCP characteristics in a planar phased array. However, it is unclear if the mutual coupling is responsible for the required modification of the stackup given that the slot underneath the microstrip patch can also introduce more radiation due to the low permittivity foam.

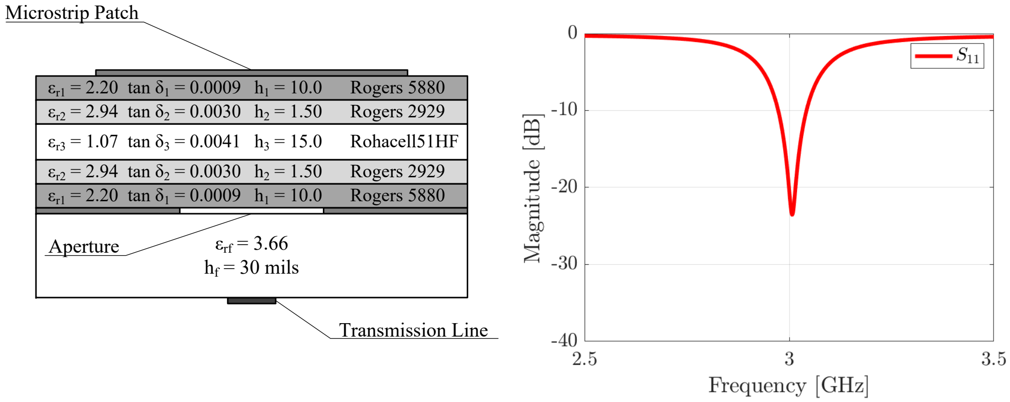

(a) Antenna Stackup Properties

(b) ARC at Boresight

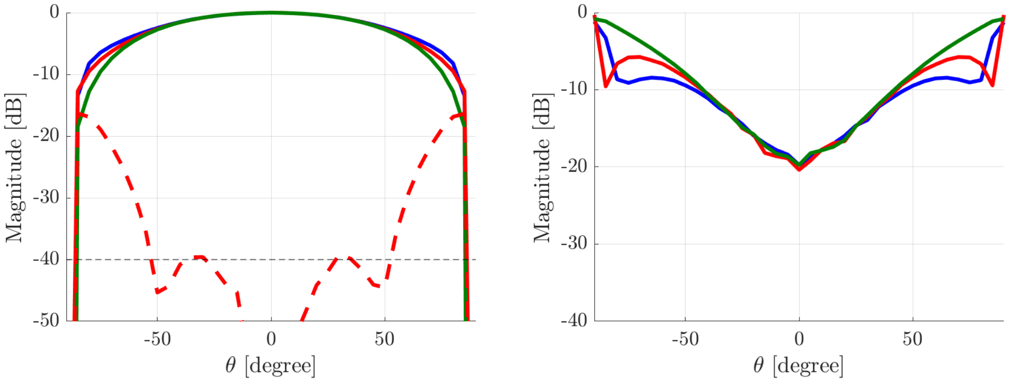

(c) Co- and Cross-polarization Radiation Patterns

(d) Scanned ARC

Figure 5.10: Simulated (IAA) results for the proposed ULCP microstrip patch antenna using the modified ADL. a) Antenna stackup properties. b) Reflection coefficient of the antenna. c) Co- and cross-polarization patterns based on Ludwig's third definition of polarization for *E*- (blue), *D*- (red), and *H*-plane (green). d) Scanned active reflection coefficient for *E*-, *D*-, and *H*-plane.

5.3 Summary

The design of an ULCP microstrip patch antenna was explored in this chapter. Section 5.1.1 proposed the ULCP antenna geometry made from an ADL and an aperture coupled microstrip patch. Mathematical relations to estimate the electrical properties of the ADL were shown and combined with the ULCP model to estimate cross-polarization levels in the antenna. Section 5.1.2 presented the simulated results of the ULCP microstrip patch antenna using HFSS MoM and IAA. MoM results from Section 5.2.1 and 5.2.2 showed cross-polarization levels that were close to those predicted by the ULCP microstrip patch model. IAA results from Section 5.2.3 to 5.2.5 showed that the ADL had to be modified to achieve ULCP characteristics. It is unclear at this point if mutual coupling alone is responsible for the required modification given that the slot underneath the microstrip patch can introduce more radiation in the antenna through the low permittivity foam. Nevertheless, this chapter proved that ULCP microstrip patch antennas are not only limited to a theoretical model but they can be made into a practical antenna designs.

Chapter 6

Conclusions

6.1 Conclusions

This work discussed the design of dual-polarized antenna elements with the goal of satisfying the planar phased array weather requirements of multi-function radars. In accordance to the hypothesis it was found that, the dielectric substrate underneath microstrip patch antennas play a fundamental role in cross-polarization performance. Multiple microstrip patch antenna elements with different bandwidths and polarization characteristics were designed considering the electrical properties of the substrate stackups and their feeding networks. Key take-aways and conclusions from this dissertation are summarized as follows:

- Co- and cross-polarization radiation patterns are highly dependent on co-ordinate systems and polarization definitions, as discussed in Section 3.1. In H/V polarization, (i.e., Ludwig's 2-I polarization definition) neither a dipole nor a microstrip patch antenna can satisfy the polarimetric weather requirements of the antenna due to the misprojection of electromagnetic fields in the AZ/EL coordinate system. However, microstrip patch antennas satisfy almost all polarimetric requirements with the exception of cross-polarized radiation bias in Ludwig's third definition of polarization [61] (i.e., orthogonal Huygen source polarization basis).

- Dual-polarized microstrip patch antennas show the highest scanned intrinsic cross-polarizations (IXR) between dipole, horizontal dipole over ground, slot, dielectric-covered slot, and waveguide antennas, as shown in Sections 3.3 - 3.5. These results make microstrip patch antennas highly calibratable. Previously discussed in [18], IXR relates to the relative errors in the final, calibrated, polarimetric measurement where high IXRs are an indication of the antenna's calibratability [63]. Thus, microstrip patch antenna elements are well suited for polarimetric weather measurements due to their high scanned IXRs.

- The ultra-low cross-polarization dielectric-covered slot antenna (ULCP-DCSA) design discussed in Section 3.4.4 exhibited higher IXRs than traditional dielectric-covered slot antennas. However, the ULCP-DCSA IXR is limited by co-polarized beam mismatch. It was found that dielectric-covered slot antennas satisfy an ultra-low cross-polarization (ULCP) condition when the substrate thickness and dielectric constant are $\approx 0.21\lambda_o$ and 1.72, respectively. This condition did not allow for good co-polarized matching between E- and H-plane of different polarizations.

- The ultra-low cross-polarization microstrip patch antenna design discussed in Section 3.5.1 exhibited higher IXRs than traditional microstrip patch antennas. It was found that microstrip patch antennas satisfy an ULCP condition when the substrate thickness and dielectric constants underneath the microstrip patch are $\approx 0.01\lambda_o$ and 1.72, respectively. Moreover, this condition allowed for good co-polarized matching between E- and H-plane of different polarizations. Therefore, the IXR of ULCP-MPAs exceeded 33 dB over $\theta_s = \pm 45°$, which is the highest IXR between all presented antennas.

- The Horus antenna design shown in Section 4.3.1 was made from two sub-assemblies, overcoming substrate thickness constraints imposed by PCB technology by separating the feeding network from the microstrip patches. The innovative separation between the sub-assemblies enabled the use of thick dielectric substrates with aperture coupling feeding technique, allowing for a fractional bandwidth of 15.4% with a planar backing ground for integration. Its polarization characteristics showed a co-polarized beam mismatch of 0.08 dB and scanned cross-polarization levels of -29 dB, based on Ludwig's third definition of polarization over $\theta_s = \pm 45°$.
- The PAIR antenna design shown in Section 4.3.2 was made using balanced probe-fed stacked microstrip patches, totaling a fractional bandwidth of 7.7%. The antenna design cleverly incorporates both (i.e., H- and V-polarization) feeding networks in one layer allowing for a planar backing ground plane for integration using only five electrical layers. Its polarization characteristics showed a co-polarized beam mismatch of 0.21 dB and scanned cross-polarization levels under -40 dB for $\theta_s = \pm 45°$ and $\phi_s = \pm 10°$. These scanning characteristics make the PAIR antenna ideal for polarimetric imaging radars.
- The Horus-ONR antenna design shown in Section 4.3.3 was made following the Horus manufacturing guidelines. The motivation behind the design was to increase the bandwidth capabilities of the Horus antenna. The Horus-ONR antenna does not need to comply with weather requirements,

therefore, a tradeoff between polarization characteristics was made to achieve the desired capabilities. It exhibited a bandwidth of 24.8% over the same scanning region (i.e., $\theta_s = \pm 45°$), representing nearly a 10% bandwidth improvement over the Horus antenna.

- A practical ULCP-MPA design was discussed in chapter 5 using an artificial dielectric layer (ADL). The use of an ADL was required in the ULCP-MPA because there is not a commercially available dielectric substrate with a permittivity of ≈ 1.72. Simulations for the antenna show what is possibly the lowest scanning cross-polarization antenna ever designed, -40 dB in $\theta_s = \pm 45°$, based on Ludwig's third definition of polarization. However, the antenna bandwidth is significantly low (i.e., less than 2%) given the substrate thickness requirement (i.e., $\approx 0.01\ \lambda_o$) for achieving an ULCP condition.

6.2 Research Limitations

There are some limitations with the results presented for mathematically modeled, simulated, and manufactured antennas presented in this dissertation. These limitations are summarized as follows:

- Unit-cell simulations for all frequencies and scanning angles were not acquired for all manufactured and designed antennas due to required computational time. However, it is expected from the antennas to behave similarly across their operational bandwidths. Active reflection coefficient calculations through mutual coupling measurements support this argument for the Horus, PAIR, and Horus-ONR antennas, as shown in Sections 4.3.1, 4.3.2, and 4.3.3.

- Subarray element patterns were not acquired through simulations. Computational memory limits were found using simulating tools that exceeded available resources. These patterns should predict more accurately the full array patterns given that they include array element mirroring. Nevertheless, published measurements in [42] show the expected scanned cross-polarization of the Horus subarray including array mirroring. These measurements predicted the expected cross-polarization cancelation on the principal planes for the new Horus antenna.

- Co- and cross-polarization radiation pattern measurements were not acquired for the manufactured arrays. It was discussed in [39] and expanded in [77] that phased array antennas exhibit edge diffractions when measured. If the size of the measured array is too small, edge effects will increase cross-polarization levels. For this reason, it is ineffective to measure any antenna element in a small array to predict the full array cross-polarization (i.e., scanned array cross-polarization).

- The performance of the Horus, PAIR, and Horus-ONR antennas will be influenced by the presence of a radome. However, the radome was not modeled in any geometry leaving the true antenna performance unknown. Nevertheless, the radome should not have a significant impact in the polarization characteristics of these antennas because its design, in principle, is to minimize their interactions (i.e., interactions between the antenna and the radome).

- The cross-polarization of a theoretical ULCP-DCSA shown in Section 3.4.4 requires a substrate thickness $\approx 0.21\lambda$ and dielectric constant ≈ 1.72. These findings did not consider the excitation of the aperture, surface waves, or the slot radiation in the back of the ground plane.

- The polarization characteristics of the ULCP-MPA shown in Section 3.5.1 were based in the electric current model. The electric current model does not include array mutual coupling or the slot radiation from the feeding network. For this reason, it was necessary to change the dielectric constant of the stackup to redefine this ULCP condition.

6.3 Future Research

The following research opportunities are proposed based on the findings of this work and its limitations:

- It proved difficult to gage whether polarimetric weather measurements are feasible in Huygen source polarization basis, due to the lack of studies in the literature. Exploring the feasibility of weather measurements using Huygen source polarization, as shown in [61], should be an area of research interest. A dual-polarized polarimetric phased array radar with digital capabilities would be ideal for this endeavor due to its ultimate beam-forming flexibility.
- This work used IXR to characterize dual-polarized antenna elements for polarimetric weather radars. This was proposed because of the relation between IXR and the total relative errors found in the measured returned signals of a fully calibrated system. Work from [87] show that the IXR of an array is limited due to the alignment between antenna elements (i.e., the embedded element IXR = the array IXR). However, if the elements were not aligned (i.e., randomly rotated elements in an aperture), the IXR of the array could be improved. Future studies in randomly oriented elements in phased arrays are needed. Important research questions that need to be answered

are the following: “Which kind of practical antenna elements can be used on these arrays?”, “How could the system be aligned or calibrated if the mutual coupling across the aperture is irregular?”, and “Are co- and cross-polarization at the element level important for polarimetric measurements if the array exhibits high IXRs?”.

- The surface waves in a theoretical ULCP-DCSA with substrate thickness and dielectric constant of $\approx 0.21\lambda$ and ≈ 1.72, do not introduce scan blindness in a field of view defined by $\theta_s = \pm\, 45°$. The radiation of the slot in the back of the ground plane can be mitigated by introducing another ground plane under the slot, converting the exposed transmission line into a stripline. Further exploration into this approach could potentially allow for a practical ULCP-DCSA. Moreover, the linearly polarized antenna could potentially become dual-polarized by introducing an orthogonal slot in the geometry.
- This work presented the design of a practical linearly polarized ULCP-MPA. This design can be expanded to include a second polarization adding a slotted ground as it was done for the Horus antenna. It is highly possible that a dual-polarized version of the ULCP-MPA can be designed.
- The ULCP antenna models proved mathematically uncertain when the antennas are part of an array. There is a gap for mathematical models that can include mutual coupling effects and other physical characteristics of the antenna.

References

[1] H. T. Friis, “A New Directional Receiving System”, *Proceedings of the Institute of Radio Engineers*, vol. 13, no. 6, pp. 685–707, 1925. DOI: `10.1109/JRPROC.1925.220990`.

[2] H. T. Friis and C. B. Feldman, “A Multiple Unit Steerable Antenna for Short-wave Reception”, *Bell System Technical Journal*, vol. 16, no. 3, pp. 337–419, 1937. DOI: `https://doi.org/10.1002/j.1538-7305.1937.tb00425.x`. eprint: `https://onlinelibrary.wiley.com/doi/pdf/10.1002/j.1538-7305.1937.tb00425.x`. [Online]. Available: `https://onlinelibrary.wiley.com/doi/abs/10.1002/j.1538-7305.1937.tb00425.x`.

[3] T. K. Sarkar, R. Mailloux, A. A. Oliner, M. Salazar-Palma, and D. L. Sengupta, “A History of Phased Array Antennas”, in *History of Wireless*. 2006, pp. 567–603.

[4] A. B. Chamberlain and W. B. Lodge, “The Broadcast Antenna”, *Proceedings of the Institute of Radio Engineers*, vol. 24, no. 1, pp. 11–35, 1936.

[5] A. Sayin, M. Cherniakov, and M. Antoniou, “Passive Radar Using Starlink Transmissions: A Theoretical Study”, in *2019 20th International Radar Symposium (IRS)*, 2019, pp. 1–7.

[6] R. Flamini, C. Mazzucco, R. Lombardi, C. Massagrande, F. Morgia, and A. Milani, “Millimeter-wave Phased Arrays for 5G: An Industry View on Current Issues and Challenges”, in *2019 IEEE International Symposium on Phased Array System Technology (PAST)*, 2019, pp. 1–2.

[7] *NWRT: End of an Era*, `https://www.nssl.noaa.gov/about/history/nwrt-decommission/`, (Accessed on 09/27/2020), 2016.

[8] D. E. Forsyth, J. F. Kimpel, D. S. Zrnic, S. S. Sandgathe, C. F. Pfeil, J. F. Heimmer, T. McNellis, J. E. Crain, A. M. Shapiro, J. D. Belville, and W. Benner, "The National Weather Radar Testbed (Phased-array)", in *Preprints, 32d Conf. on Radar Meteorology*, 2005, 12R.3.

[9] M. C. Leifer, V. Chandrasekar, and E. Perl, "Dual Polarized Array Approaches for MPAR Air Traffic and Weather Radar Applications", in *2013 IEEE International Symposium on Phased Array Systems and Technology*, 2013, pp. 485–489. DOI: `10.1109/ARRAY.2013.6731876`.

[10] R. Palmer, C. Fulton, J. Salazar, H. Sigmarsson, and M. Yeary, "The "Horus" Radar - An All-digital Polarimetric Phased Array Radar for Multi-mission Surveillance", *American Meteorological Society Annual Meeting, Phoenix, AZ*, 2019. DOI: `10.1109/PAST43306.2019.9020988`.

[11] Yanting Wang and V. Chandrasekar, "Polarization Isolation Requirements for Linear Dual-polarization Weather Radar in Simultaneous Transmission Mode of Operation", *IEEE Transactions on Geoscience and Remote Sensing*, vol. 44, no. 8, pp. 2019–2028, 2006, ISSN: 1558-0644. DOI: `10.1109/TGRS.2006.872138`.

[12] D. S. Zrnic and R. J. Doviak, "System Requirements for Phased Array Weather Radars", *in NOAA/NSSL Tech. Rep.*, 2005.

[13] Y. Wang, V. Chandrasekar, and V. N. Bringi, "Characterization and Evaluation of Hybrid Polarization Observation of Precipitation", *Journal of Atmospheric and Oceanic Technology*, vol. 23, no. 4, pp. 552–572, 2006. DOI: `10.1175/JTECH1869.1`. eprint: `https://doi.org/10.1175/JTECH1869.1`. [Online]. Available: `https://doi.org/10.1175/JTECH1869.1`.

[14] R. A. Brown and V. T. Wood, "Development of New WSR-88D Scanning Strategies for Convective Situations", National Severe Storms Laboratory, 1999.

[15] R. J. Doviak and D. Z. Zrnic, "WSR-88D Radar for Research and Enhancement of Operations: Polarimetric Upgrades to Improve Rainfall Measurements", National Severe Storms Laboratory, 1998.

[16] G. Zhang, R. J. Doviak, D. S. Zrnić, R. Palmer, L. Lei, and Y. Al-Rashid, "Polarimetric Phased-array Radar for Weather Measurement: A Planar or Cylindrical Configuration?", *Journal of Atmospheric and Oceanic*

Technology, vol. 28, no. 1, pp. 63–73, Jan. 2011, ISSN: 0739-0572. DOI: `10.1175/2010JTECHA1470.1`. eprint: `https://journals.ametsoc.org/jtech/article-pdf/28/1/63/3344370/2010jtecha1470\_1.pdf`. [Online]. Available: `https://doi.org/10.1175/2010JTECHA1470.1`.

[17] C. Fulton, J. L. Salazar, Y. Zhang, G. Zhang, R. Kelly, J. Meier, M. McCord, D. Schmidt, A. D. Byrd, L. M. Bhowmik, S. Karimkashi, D. S. Zrnic, R. J. Doviak, A. Zahrai, M. Yeary, and R. D. Palmer, "Cylindrical Polarimetric Phased Array Radar: Beamforming and Calibration for Weather Applications", *IEEE Transactions on Geoscience and Remote Sensing*, vol. 55, no. 5, pp. 2827–2841, 2017.

[18] T. D. Carozzi and G. Woan, "A Fundamental Figure of Merit for Radio Polarimeters", *IEEE Transactions on Antennas and Propagation*, vol. 59, no. 6, pp. 2058–2065, 2011.

[19] J Herd and S Duffy, "Overlapped Digital Subarray Architecture for Multiple Beam Phased Array Radar", *Antennas and Propagation (EUCAP), Proceedings of the 5th European Conference on*, pp. 3027–3030, 2011.

[20] C. Fulton and W. Chappell, "A Dual-polarized Patch Antenna for Weather Radar Applications", in *2011 IEEE International Conference on Microwaves, Communications, Antennas and Electronic Systems (COMCAS 2011)*, vol. 2, IEEE, 2011, pp. 1–5, ISBN: 978-1-4577-1694-2. DOI: `10.1109/COMCAS.2011.6105940`. [Online]. Available: `http://ieeexplore.ieee.org/lpdocs/epic03/wrapper.htm?arnumber=6105940`.

[21] J. A. Ortiz, J. Díaz, N. Aboserwal, J. L. Salazar, L. Jeon, S. Sim, and J. Chun, "Ultra-compact Universal Polarization X-band Unit Cell for High-performance Active Phased Array Radar", in *2016 IEEE International Symposium on Phased Array Systems and Technology (PAST)*, 2016, pp. 1–5. DOI: `10.1109/ARRAY.2016.7832592`.

[22] H. Saeidi-Manesh and G. Zhang, "High-isolation, low Cross-polarization, Dual-polarization, Hybrid Feed Microstrip Patch Array Antenna for MPAR Application", *IEEE Transactions on Antennas and Propagation*, vol. 66, no. 5, pp. 2326–2332, 2018, ISSN: 1558-2221. DOI: `10.1109/TAP.2018.2811780`.

[23] J. L. Salazar, E. J. Knapp, and D. J. McLaughlin, "Dual-polarization Performance of the Phase-tilt Antenna Array in a CASA Dense Network Radar", *2010 IEEE International Geoscience and Remote Sensing*

Symposium, pp. 3470–3473, 2010. DOI: `10.1109/IGARSS.2010.5650310`. [Online]. Available: `http://ieeexplore.ieee.org/lpdocs/epic03/wrapper.htm?arnumber=5650310`.

[24] J. L. Salazar, E. Loew, P.-S. Tsai, J. Vivekanandan, W. C. Lee, and V Chandrasekar, "Design and Development of a 2-D Electronically Scanned Dual-polarization Line-Replaceable-Unit (LRU) for Airborne Phased Array Radar for Atmospheric Research", *Preprints Proceedings of 36th International Conference on Radar Meteorology*, vol. 64, no. 1, pp. 1–6, 2013.

[25] S. Karimkashi and G. Zhang, "A Dual-polarized Series-fed Microstrip Antenna Array with Very High Polarization Purity for Weather Measurements", *IEEE Transactions on Antennas and Propagation*, vol. 61, no. 10, pp. 5315–5319, 2013, ISSN: 0018-926X. DOI: `10.1109/TAP.2013.2273813`. [Online]. Available: `http://ieeexplore.ieee.org/lpdocs/epic03/wrapper.htm?arnumber=6562773`.

[26] M. Mirmozafari and G. Zhang, "A Highly Isolated Dual-polarized Linear Array Antenna with Very Low Cross-polarization", in *2017 IEEE International Symposium on Antennas and Propagation USNC/URSI National Radio Science Meeting*, 2017, pp. 1809–1810.

[27] N. Ong, "Manufacturing Cost Estimation for PCB Assembly: An Activity-based Approach", *International Journal of Production Economics*, vol. 38, no. 2, pp. 159 –172, 1995, ISSN: 0925-5273. DOI: `https://doi.org/10.1016/0925-5273(94)00089-S`. [Online]. Available: `http://www.sciencedirect.com/science/article/pii/092552739400089S`.

[28] C. A. Balanis, *Antenna Theory: Analysis and Design.* John Wiley & Sons, 2015, p. 1072, ISBN: 9781118642061.

[29] J. Schuss and J. Hanfling, "Nonreciprocity and Scan Blindness in Phased Arrays Using Balanced-fed Radiators", *IEEE Transactions on Antennas and Propagation*, vol. 35, no. 2, pp. 134–138, 1987.

[30] D. R. Jackson and N. G. Alexopoulos, "Simple Approximate Formulas for Input Resistance, Bandwidth, and Efficiency of a Resonant Rectangular Patch", *IEEE Transactions on Antennas and Propagation*, vol. 39, no. 3, pp. 407–410, 1991.

[31] D. M. Pozar, “A Review of Bandwidth Enhancement Techniques for Microstrip Antennas”, in *Microstrip Antennas: The Analysis and Design of Microstrip Antennas and Arrays*, D. M. Pozar and D. H. Schaubert, Eds., IEEE Press, 1995, ch. 4, pp. 157–166, ISBN: 0-7803-1078-0.

[32] J. L. Volakis, Ed., *Antenna Engineering Handbook*, 4th ed. New York: McGraw-Hill, 2007, OCLC: ocm55685786, ISBN: 9780071475747.

[33] D. M. Pozar, “Microstrip Antenna Aperture-coupled to a Microstripline”, *Electronics Letters*, vol. 21, no. 2, p. 49, 1985, ISSN: 00135194. DOI: `10.1049/el:19850034`.

[34] J. Salazar, *Dual-polarized Radiating Patch Antenna*, U.S. Patent 2016 0079672 A1, March 17, 2016. [Online]. Available: `https://www.google.com/patents/US20160079672`.

[35] D. Sun, Z. Zhang, X. Yan, and X. Jiang, “Design of Broadband Dual-polarized Patch Antenna with Backed Square Annular Cavity”, *IEEE Transactions on Antennas and Propagation*, vol. 64, no. 1, pp. 43–52, 2016. DOI: `10.1109/TAP.2015.2500904`.

[36] N. Aboserwal, N. R. Ccoillo Ramos, Z. Qamar, and J. L. Salazar-Cerreno, “An Accurate Analytical Model to Calculate the Impedance Bandwidth of a Proximity Coupled Microstrip Patch Antenna (PC-MSPA)”, *IEEE Access*, vol. 8, pp. 41 784–41 793, 2020. DOI: `10.1109/ACCESS.2020.2976750`.

[37] M. Mirmozafari, “Design and Implementation of a Phased Array Antenna for Multi-mission Applications”, PhD dissertation, University of Oklahoma, Norman, OK, USA, 2018.

[38] M. Mirmozafari, S. Saeedi, G. Zhang, and Y. Rahmat-Samii, “A Crossed Dipole Phased Array Antenna Architecture with Enhanced Polarization and Isolation Characteristics”, *IEEE Transactions on Antennas and Propagation*, vol. 68, no. 6, pp. 4469–4478, 2020.

[39] J. L. Salazar, N. Aboserwal, J. D. Díaz, J. A. Ortiz, and C. Fulton, “Edge Diffractions Impact on the Cross Polarization Performance of Active Phased Array Antennas”, in *2016 IEEE International Symposium on Phased Array Systems and Technology (PAST)*, 2016, pp. 1–5. DOI: `10.1109/ARRAY.2016.7832571`.

[40] S. Karimkashi and G. Zhang, "Optimizing Radiation Patterns of a Cylindrical Polarimetric Phased Array Radar for Multimissions", *IEEE Transactions on Geoscience and Remote Sensing*, vol. 53, no. 5, pp. 2810–2818, 2015.

[41] J. E. Stailey and K. D. Hondl, "Multifunction Phased Array Radar for Aircraft and Weather Surveillance", *Proceedings of the IEEE*, vol. 104, no. 3, pp. 649–659, 2016.

[42] J. D. Díaz, J. L. Salazar-Cerreno, J. A. Ortiz, N. A. Aboserwal, R. M. Lebrón, C. Fulton, and R. D. Palmer, "A Cross-stacked Radiating Antenna with Enhanced Scanning Performance for Digital Beamforming Multifunction Phased-array Radars", *IEEE Transactions on Antennas and Propagation*, vol. 66, no. 10, pp. 5258–5267, 2018, ISSN: 1558-2221. DOI: `10.1109/TAP.2018.2862252`.

[43] J. L. Salazar, T. Yu, M. McCord, J. Diaz, J. A. Ortiz, C. Fulton, M. Yeary, R. Palmer, B. Cheong, H. Bluestein, J. M. Kurdzo, and B. Isom, "An Ultra-fast Scan C-band Polarimetric Atmospheric Imaging Radar (PAIR)", in *2019 IEEE International Symposium on Phased Array System Technology (PAST)*, 2019, pp. 1–5.

[44] J. Diaz, J. Salazar, J. Ortiz, C. Fulton, N. Aboserwal, R. Kelley, and R. Palmer, "A Dual-polarized Stacked Patch Antenna with Wide-angle and Low Cross-polarization for Fully Digital Multifunction Phased Array Radars", in *Fifth International Symposium on Phased Array Systems and Technology*, Boston, MA, 2016.

[45] M. Mirmozafari, H. Saeidi-Manesh, and G. Zhang, "Highly Isolated Crossed Dipole Antenna with Matched Copolar Beams", *Electronics Letters*, vol. 54, no. 8, pp. 470–472, 2018, ISSN: 0013-5194. DOI: `10.1049/el.2018.0519`.

[46] J. D. Díaz, N. Aboserwal, J. T. Logan, R. W. Kindt, and J. L. Salazar, "Ultra-low Cross Polarization Microstrip Patch Antennas for Phased Arrays", in *2019 IEEE International Symposium on Phased Array System Technology (PAST)*, 2019, pp. 1–4.

[47] R. Mailloux, *Phased Array Antenna Handbook.* Artech House, 2005.

[48] M. Henderson, M. B. Davis, and M. Huisjen, "GDPAA Advanced Technology Demonstration Overview and Results", in *2010 IEEE International*

Symposium on Phased Array Systems and Technology, 2010, pp. 140–143. DOI: `10.1109/ARRAY.2010.5613380`.

[49] D. S. Zrnic, G. Zhang, and R. J. Doviak, “Bias Correction and Doppler Measurement for Polarimetric Phased-array Radar”, *IEEE Transactions on Geoscience and Remote Sensing*, vol. 49, no. 2, pp. 843–853, 2011. DOI: `10.1109/TGRS.2010.2057436`.

[50] K. Sperzel, “Creeping Wave Propagation on Cylindrical Radiating Structures”, Master Thesis, University of Oklahoma, Norman, OK, USA, 2019.

[51] D. M. Pozar, *Microwave Engineering*, 4th ed. John Wiley and Sons, 2012.

[52] D. M. Pozar, “A Relation Between the Active Input Impedance and the Active Element Pattern of a Phased Array”, *IEEE Transactions on Antennas and Propagation*, vol. 51, no. 9, pp. 2486–2489, 2003. DOI: `10.1109/TAP.2003.816302`.

[53] D. M. Pozar, “The Active Element Pattern”, *IEEE Transactions on Antennas and Propagation*, vol. 42, no. 8, pp. 1176–1178, 1994. DOI: `10.1109/8.310010`.

[54] S. Holland, “Low-profile, Modular, Ultra-wideband Phased Arrays”, PhD dissertation, University of Massachusetts Amherst, Amherst, MA, USA, 2011.

[55] Ansys, *High Frequency Structure Simulator*, version 18.1. [Online]. Available: `https://www.ansys.com/products/electronics/ansys-hfss`.

[56] N. A. Aboserwal, J. L. Salazar, J. A. Ortiz, J. D. Díaz, C. Fulton, and R. D. Palmer, “Source Current Polarization Impact on the Cross-polarization Definition of Practical Antenna Elements: Theory and Applications”, *IEEE Transactions on Antennas and Propagation*, vol. 66, no. 9, pp. 4391–4406, 2018, ISSN: 1558-2221. DOI: `10.1109/TAP.2018.2845945`.

[57] A. Ludwig, “The Definition of Cross Polarization”, *IEEE Transactions on Antennas and Propagation*, vol. 21, no. 1, pp. 116–119, 1973.

[58] G. F. Masters and S. F. Gregson, “Coordinate System Plotting for Antenna Measurements,” *AMTA 29th Annual Symposium of the AMTA*, pp. 1–10, 2007.

[59] A. D. Byrd, "Simulation of Polarimetric Phased Array Weather Radars", Master Thesis, University of Oklahoma, Norman, OK, USA, 2016.

[60] G. Zhang, R. J. Doviak, D. S. Zrnic, J. Crain, D. Staiman, and Y. Al-Rashid, "Phased Array Radar Polarimetry for Weather Sensing: A Theoretical Formulation for Bias Corrections", *IEEE Transactions on Geoscience and Remote Sensing*, vol. 47, no. 11, pp. 3679–3689, 2009. DOI: `10.1109/TGRS.2009.2029332`.

[61] J. Dong, Q. Liu, and X. Wang, "New Polarization Basis for Polarimetric Phased Array Weather Radar: Theory and Polarimetric Variables Measurement", *International Journal of Antennas and Propagation*, vol. 2012, pp. 1–15, 2012. DOI: `10.1155/2012/193913`.

[62] G. H. Golub and C. F. van Loan, *Matrix Computations*, 3rd ed. The John Hopkins University Press, 1996.

[63] J. Logan, "Low Cross-Polarization Vivaldi Arrays", PhD dissertation, University of Massachusetts Amherst, Amherst, MA, USA, 2016.

[64] Y. Rahmat-Samii, "Useful Coordinate Transformations for Antenna Applications", *IEEE Transactions on Antennas and Propagation*, vol. 27, no. 4, pp. 571–574, 1979. DOI: `10.1109/TAP.1979.1142138`.

[65] C. M. Knop and G. I. Cohn, "Radiation from an Aperture in a Coated Plane", *Radio Sci. J. Res.*, vol. 68D, no. 4, pp. 363–378, 1964.

[66] Y. Lo, D. Solomon, and W. Richards, "Theory and Experiment on Microstrip Antennas", *IEEE Transactions on Antennas and Propagation*, vol. 27, no. 2, pp. 137–145, 1979. DOI: `10.1109/TAP.1979.1142057`.

[67] K. Carver and J. Mink, "Microstrip Antenna Technology", *IEEE Transactions on Antennas and Propagation*, vol. 29, no. 1, pp. 2–24, 1981, ISSN: 0096-1973. DOI: `10.1109/TAP.1981.1142523`.

[68] D. Jackson and N. Alexopoulos, "Gain Enhancement Methods for Printed Circuit Antennas", *IEEE Transactions on Antennas and Propagation*, vol. 33, no. 9, pp. 976–987, 1985.

[69] D. R. Jackson and J. T. Williams, "A Comparison of CAD Models for Radiation from Rectangular Patches", *in Intl. Journal of Microwave*

and Millimeter-Wave Computer Aided Design, vol. 1, no. 2, pp. 236–248, 1991.

[70] D. Pozar and D. Schaubert, "Scan Blindness in Infinite Phased Arrays of Printed Dipoles", *IEEE Transactions on Antennas and Propagation*, vol. 32, no. 6, pp. 602–610, 1984.

[71] K. C. Gupta, "Broadbanding Techniques for Microstrip Patch Antennas - A Review", University of Colorado, Tech. Rep., 1988.

[72] A. Sabban, "A New Broadband Stacked Two-layer Microstrip Antenna", *Antennas and Propagation Society International Symposium, 1983*, vol. 21, pp. 63–66, 1983. DOI: `10.1109/APS.1983.1149074`.

[73] S. Gao, "Microstrip Antenna Elements and Dual-polarized Arrays for Active Integration", PhD thesis, Shanghai University, 1999.

[74] S. Gao, L. Li, and P. Gardner, "Recent Research Developments in Microwave Theory & Techniques", in *Dual-polarized Antennas for Wireless Communications and Radar Systems*, B. Beker and Y. Chen, Eds., Research Signpost, 2002, ch. 8, pp. 1–28, ISBN: 81-7736-099-X.

[75] K. Woelder and J. Granholm, "Cross-polarization and Sidelobe Suppression in Dual Linear Polarization Antenna Arrays", *IEEE Transactions on Antennas and Propagation*, vol. 45, no. 12, pp. 1727–1740, 1997, ISSN: 0018926X. DOI: `10.1109/8.650190`. [Online]. Available: `http://ieeexplore.ieee.org/lpdocs/epic03/wrapper.htm?arnumber=650190`.

[76] L. M. Bhowmik, "Applications of Floquet Port Analysis to Modern Phased Array Antennas", PhD dissertation, University of Oklahoma, Norman, OK, USA, 2019.

[77] J. A. Ortiz, "Impact of Edge Diffraction in Dual-polarized Phased Array Antennas", PhD dissertation, University of Oklahoma, Norman, OK, USA, 2020.

[78] M. Yeary, R. Palmer, C. Fulton, J. Salazar, and H. Sigmarsson, "Recent Advances on an S-band All-digital Mobile Phased Array Radar", in *2019 IEEE International Symposium on Phased Array System Technology (PAST)*, 2019, pp. 1–5. DOI: `10.1109/PAST43306.2019.9020988`.

[79] F. Croq and D. Pozar, “Millimeter-wave Design of Wide-band Aperture-coupled Stacked Microstrip Antennas”, *IEEE Transactions on Antennas and Propagation*, vol. 39, no. 12, pp. 1770–1776, 1991, ISSN: 0018-926X. DOI: `10.1109/8.121599`. [Online]. Available: `http://ieeexplore.ieee.org/stamp/stamp.jsp?arnumber=121599http://ieeexplore.ieee.org/lpdocs/epic03/wrapper.htm?arnumber=121599`.

[80] M. Yamazaki, E. Rahardjo, and M. Haneishi, “Construction of a Slot-coupled Planar Antenna for Dual Polarization”, *Electronics Letters*, vol. 30, no. 22, p. 1814, 1994, ISSN: 00135194. DOI: `10.1049/el:19941261`.

[81] A. A. Serra, P. Nepa, G. Manara, G. Tribellini, and S. Cioci, “A Wide-band Dual-polarized Stacked Patch Antenna”, *IEEE Antennas and Wireless Propagation Letters*, vol. 6, pp. 141–143, 2007, ISSN: 15361225. DOI: `10.1109/LAWP.2007.893101`.

[82] T. M. F. Elshafiey, “Full Wave Analysis of a Ferrite Cross-patch Antenna”, in *2007 Loughborough Antennas and Propagation Conference*, IEEE, 2007, pp. 197–200, ISBN: 1-4244-0775-3. DOI: `10.1109/LAPC.2007.367464`. [Online]. Available: `http://ieeexplore.ieee.org/lpdocs/epic03/wrapper.htm?arnumber=4218499`.

[83] Y. Lubin and A. Hessel, “Wide-band, Wide-angle Microstrip Stacked-patch-element Phased Arrays”, *IEEE Transactions on Antennas and Propagation*, vol. 39, no. 8, pp. 1062–1070, 1991. DOI: `10.1109/8.97339`.

[84] R. B. Waterhouse, “Design of Probe-fed Stacked Patches”, *IEEE Transactions on Antennas and Propagation*, vol. 47, no. 12, pp. 1780–1784, 1999. DOI: `10.1109/8.817653`.

[85] H. Hirsch and D. Grove, *Practical Simulation of Radar Antennas and Radomes*, 304 pp. Artech House Antenna Library Series, 1988.

[86] J. L. Salazar-Cerreño, V. Chandrasekar, J. M. Trabal, P. Siquera, R. Medina, E. Knapp, and D. J. McLaughlin, “A Drop Size Distribution (DSD)-based Model for Evaluating the Performance of Wet Radomes for Dual-polarized Radars”, *Journal of Atmospheric and Oceanic Technology*, vol. 31, no. 11, pp. 2409 –2430, 1Nov. 2014. DOI: `10.1175/JTECH-D-13-00208.1`. [Online]. Available: `https://journals.ametsoc.org/view/journals/atot/31/11/jtech-d-13-00208_1.xml`.

[87] T. D. Carozzi, “Intrinsic Cross-polarization Ratio (IXR) for Antenna Arrays and Improving Polarimetry Via Polarization Diversity”, in *2015 International Conference on Electromagnetics in Advanced Applications (ICEAA)*, 2015, pp. 630–633. DOI: `10.1109/ICEAA.2015.7297193`.

Appendix A

List of Acronyms and Abbreviations

$PAARD$	Phased Array Antenna Research & Development Group
$ARRC$	Advanced Radar Research Center
IXR	Intrinsic Cross-Polarization
$PAIR$	Polarimetric Atmospheric Imaging Radar
$ULCP-MPA$	Ultra-Low Cross-Polarization Microstrip Patch Antenna
$ULCP-DCSA$	Ultra-Low Cross-Polarization Dielectric Covered Slot Antenna
LRU	Line Replaceable Unit
$NOAA$	National Oceanic and Atmospheric Administration
FAA	Federal Aviation Administration
$MPAR$	Multifunction Phased Array Radar
$WSR-88D$	Weather Surveillance Radar - 1988 Doppler
PCB	Printed Circuit Board

H	Horizontal
V	Vertical
ATD	Advanced Technology Demonstrator
TL	Transmission Line
$STSR$	Simultaneous Transmit and Receive
$APAR$	Airborne Phased Array Radar
$ULCP$	Ultra-Low Cross Polarization
$NSSL$	National Severe Storms Laboratory
$MIT-LL$	Massachusetts Institute of Technology Lincoln Laboratory
$CPPAR$	Cylindrical Polarimetric Phased Array Radar
$GDPAA-ATD$	Geodesic Dome Phased Array Antenna, Advanced Technology Demonstrator
RF	Radio Frequency
ARC	Active Reflection Coefficient
AEP	Active Element Pattern
$2D$	Two-Dimensional
$HFSS$	High-Frequency Structure Simulator
BW	Bandwidth
DDM	Domain Decomposition Method

$L1$	Ludwig's first definition of polarization
$L2-I$	Ludwig's second definition of polarization, y-polarized dipole
$L2-II$	Ludwig's second definition of polarization, x-polarized dipole
$L3$	Ludwig's third definition of polarization
AZ	Azimuth
EL	Elevation
AUT	Antenna Under Test
FoM	Figure of Merit
TE	Transverse Electric
TM	Transverse Magnetic
MMN	Multisection Matching Network
$SMP-Max$	Sub Miniature Push-on
$PTFE$	Polytetrafluoroethylene
ADL	Artificial Dielectric Layer
MoM	Method of Moments
FEM	Finite Element Method
IAA	Infinite Array Approach

Appendix B

Manufactured Antenna Array References

B.1 Horus Antenna

Figs. B.1-B.8 show individual metallic layers in the manufactured Horus antenna for sub-assemblies 1 and 2. Note that V-polarization is rotated at the array every two rows while H-polarization is rotated every two columns. The size of the manufactured unit is 15.98” inches which represents a gap between adjacent subarrays of 20 mils.

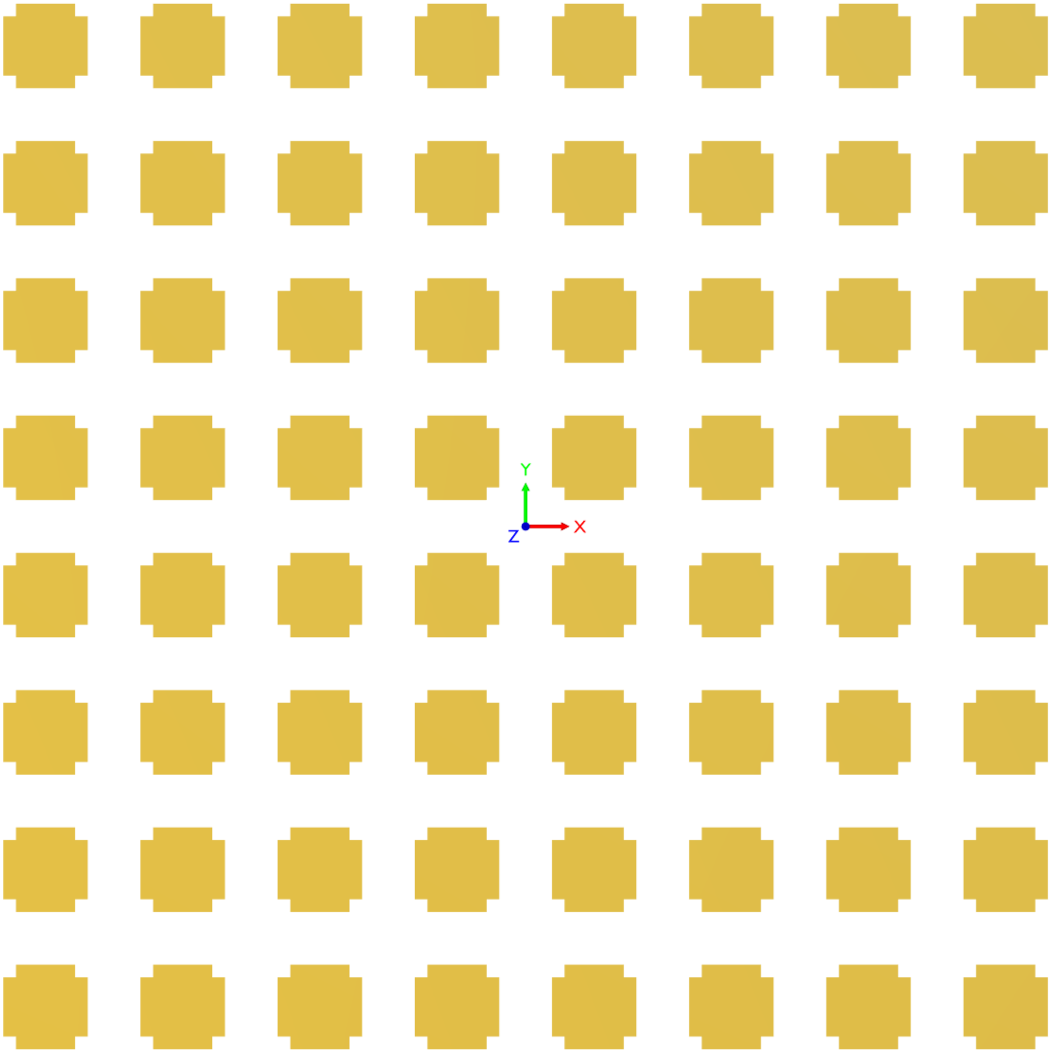

Figure B.1: Parasitic microstrip patch layer of Horus antenna in sub-assembly 2.

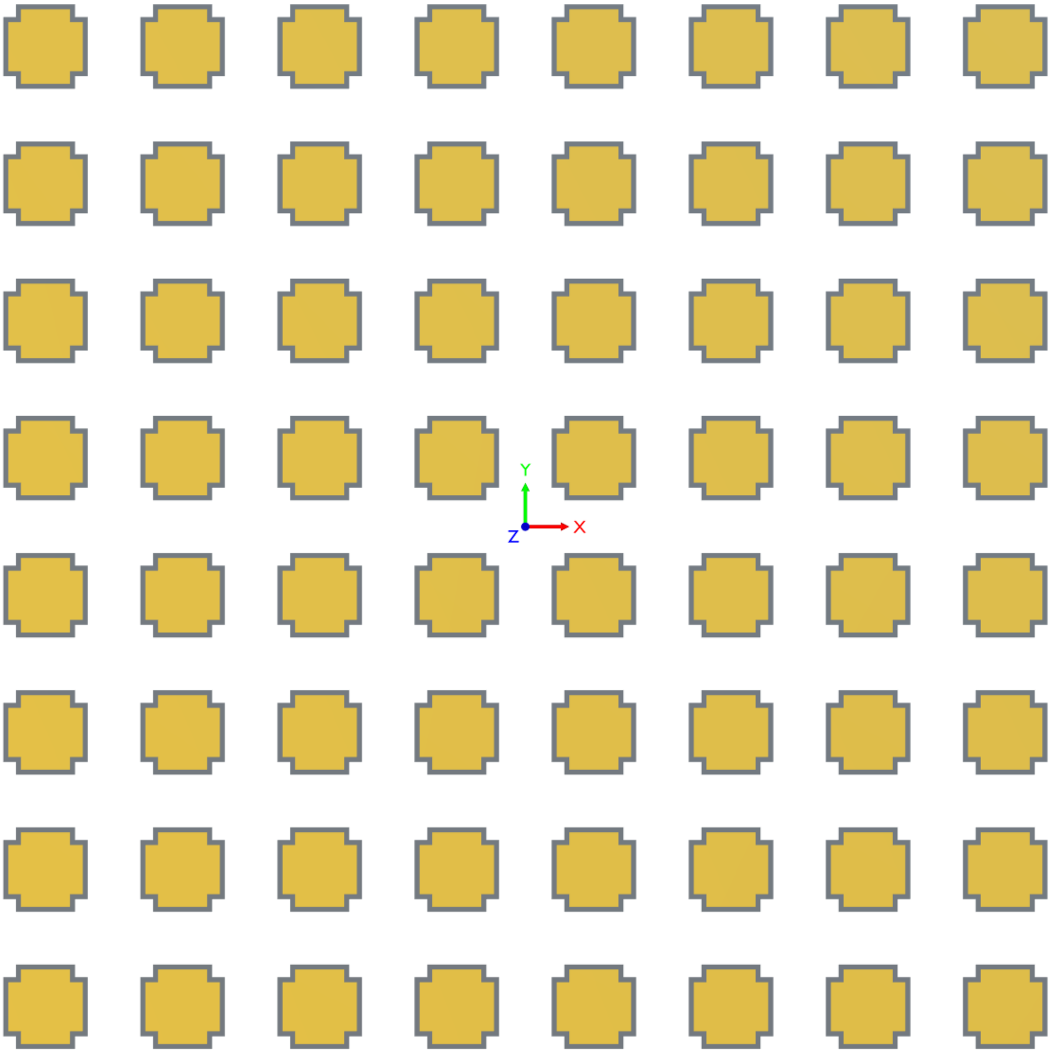

Figure B.2: Driven microstrip patch layer of Horus antenna in sub-assembly 2. The shadow microstrip patch references the parasitic located in layer 1.

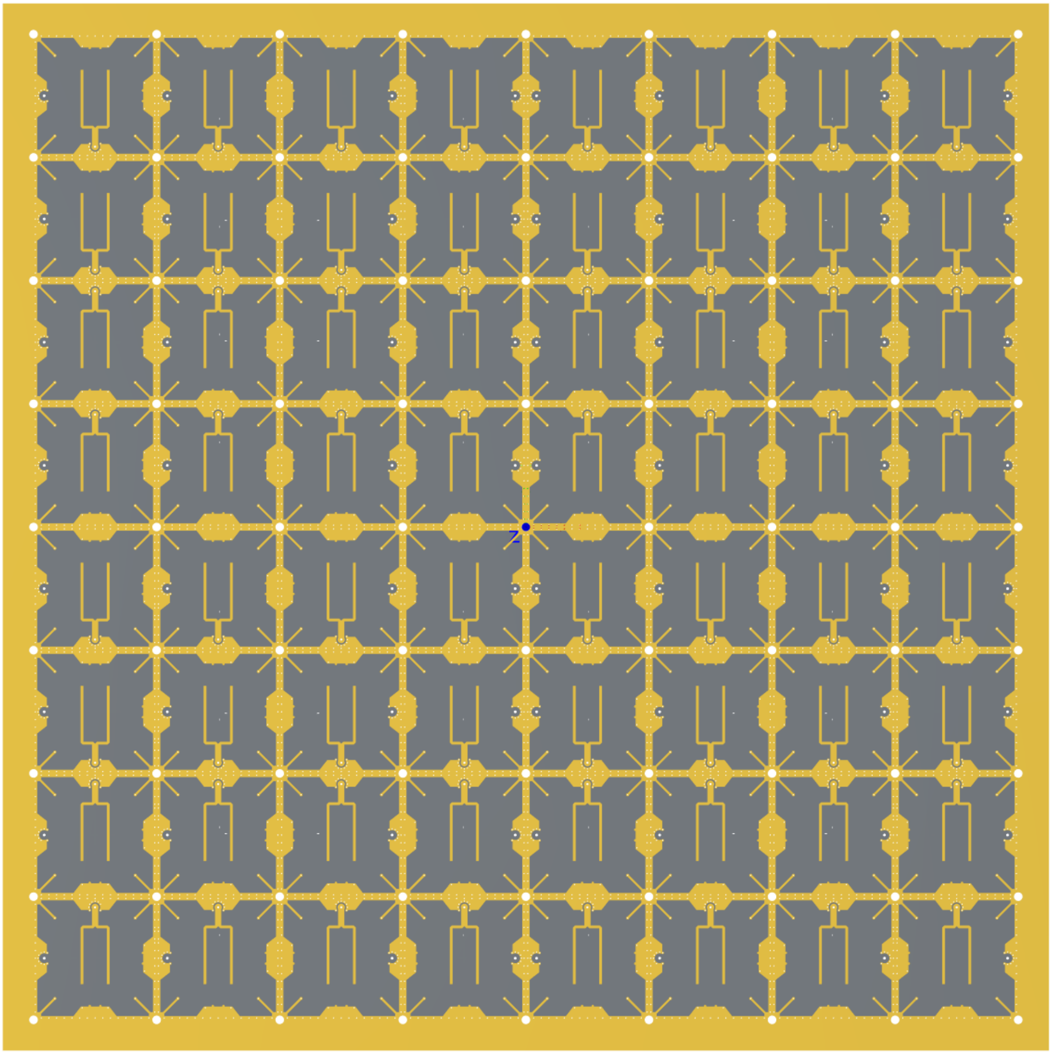

Figure B.3: V-polarization layer of Horus antenna in sub-assembly 1.

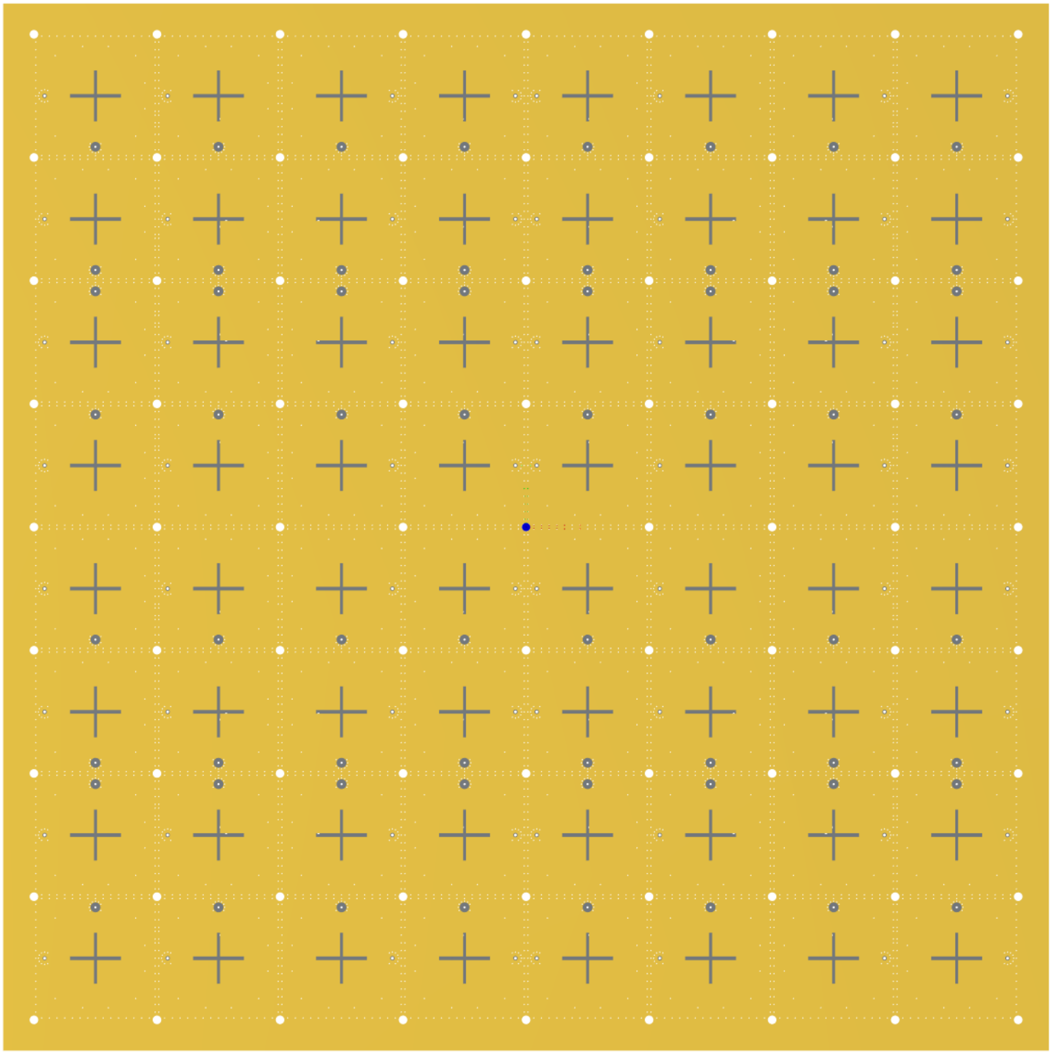

Figure B.4: Slotted ground layer of Horus antenna in sub-assembly 1.

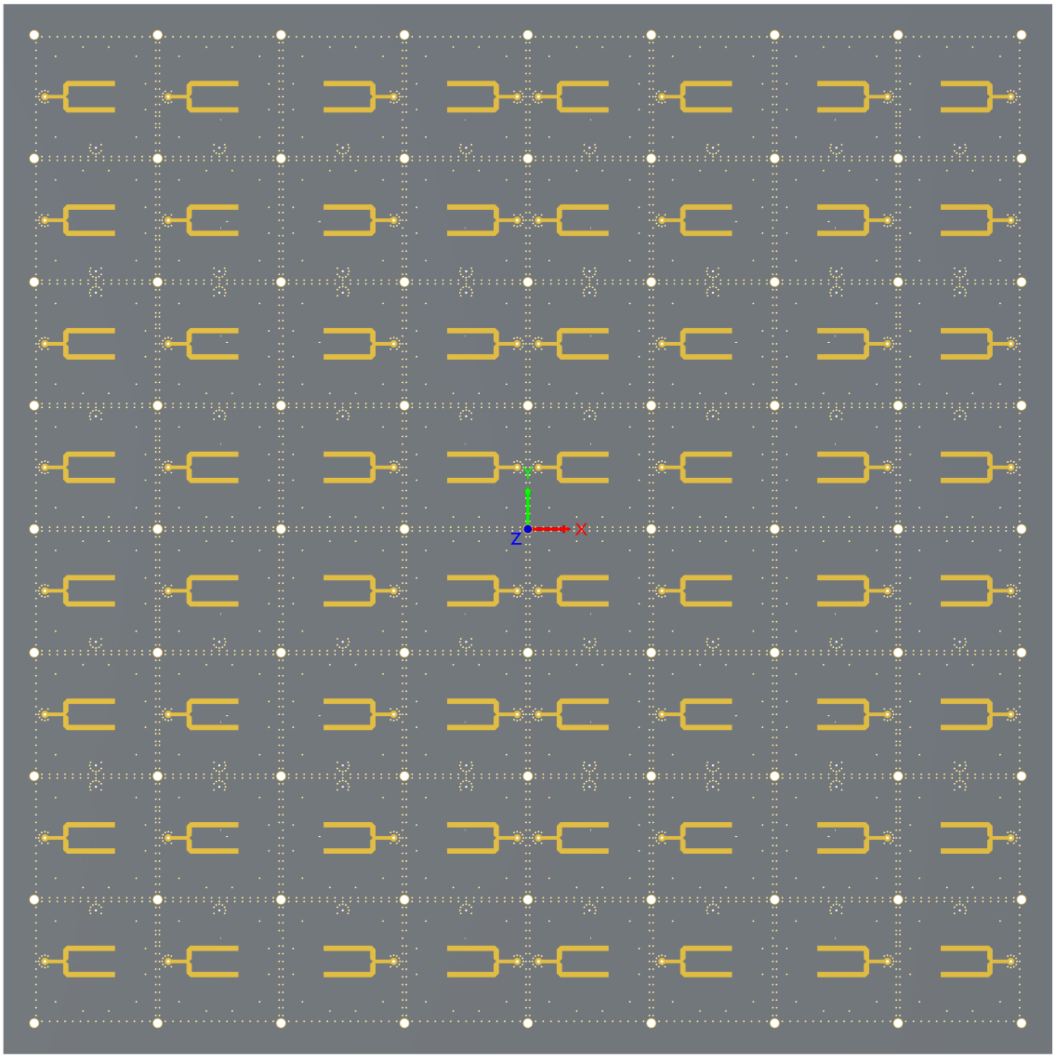

Figure B.5: H-polarization layer of Horus antenna in sub-assembly 1.

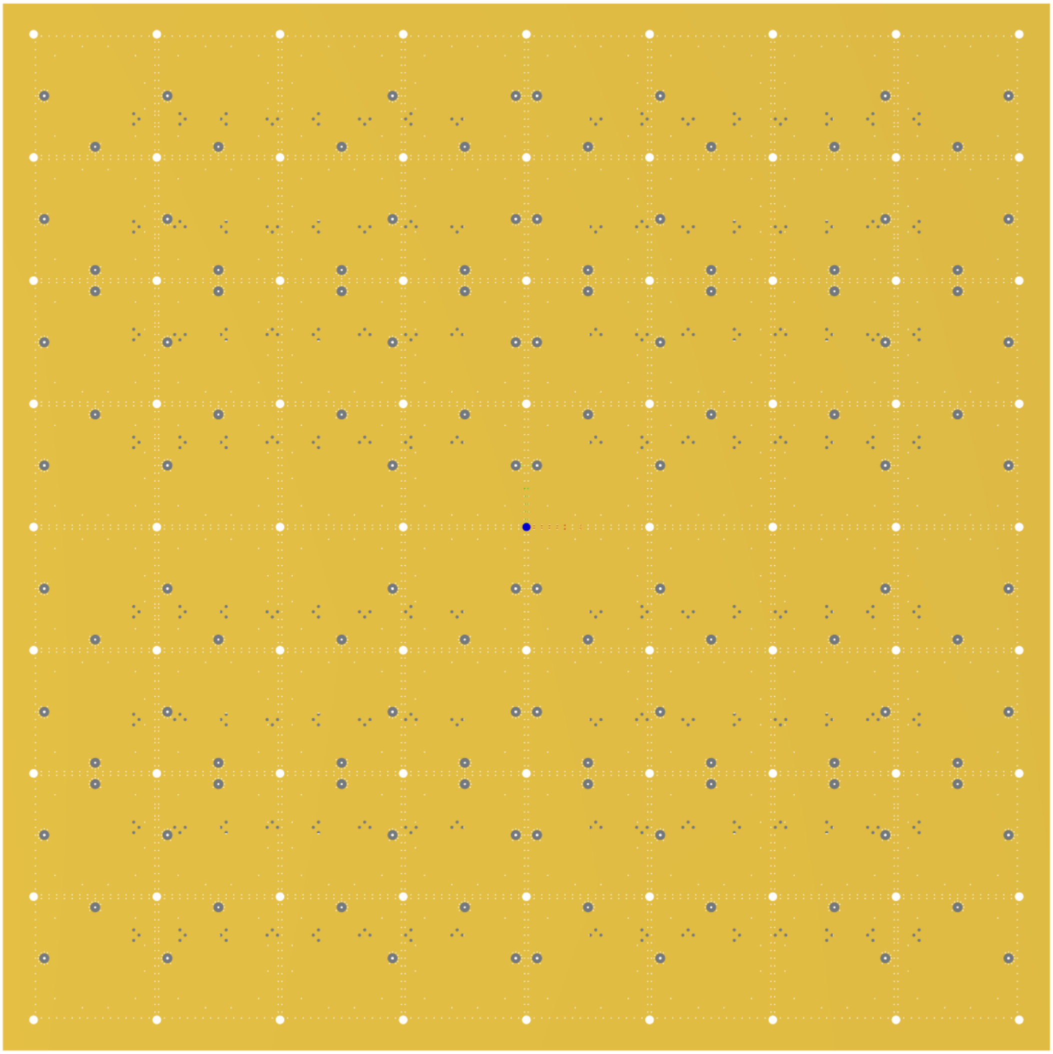

Figure B.6: Ground layer of Horus antenna in sub-assembly 1.

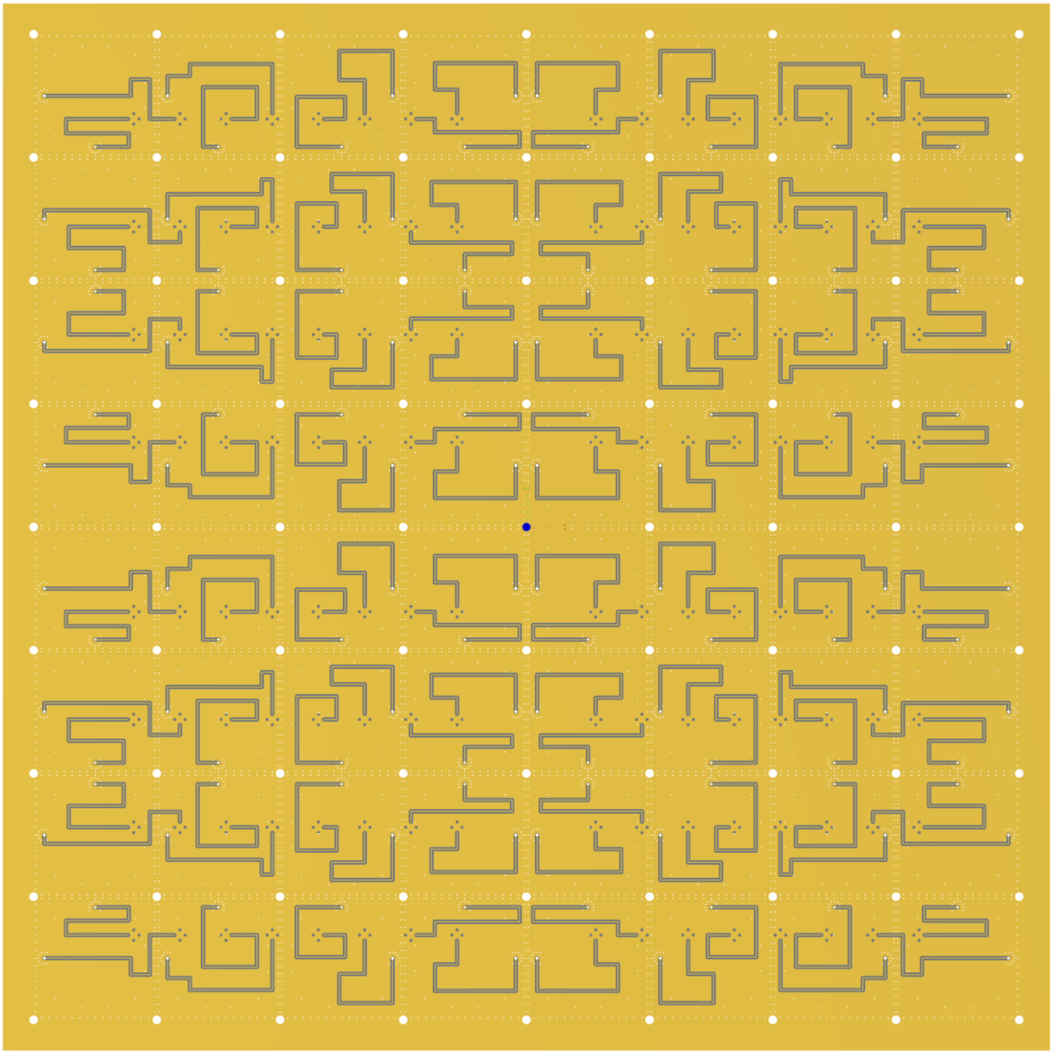

Figure B.7: H/V feeding network and ground layer of Horus antenna in subassembly 1.

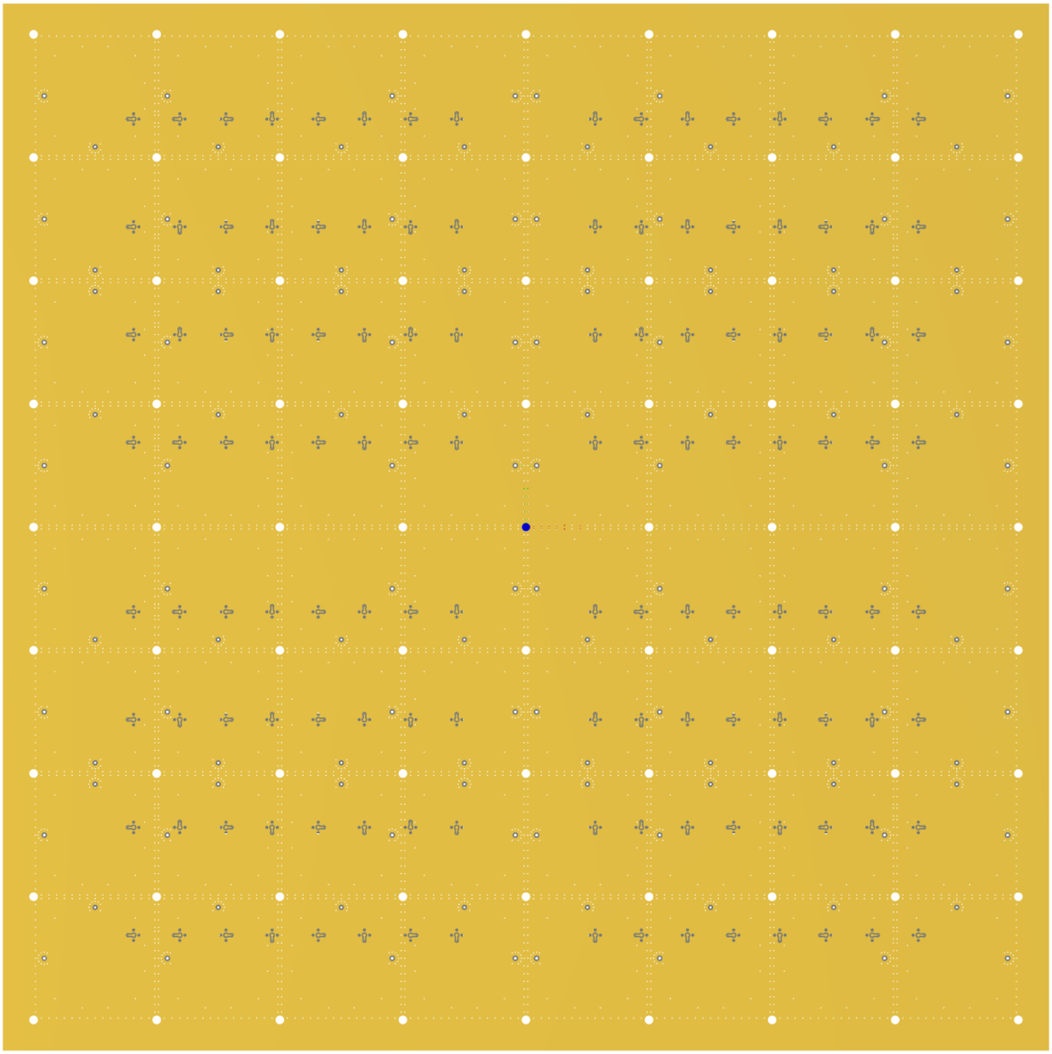

Figure B.8: H/V feeding network and ground layer of Horus antenna in subassembly 1.

B.2 PAIR Antenna

Figs. B.9-B.13 show the individual metallic layers in the manufactured PAIR antenna. The manufactured array was designed to have a gap between adjacent subarrays of 20 mils. Mirroring between V- and H-polarizations was introduced on the 8 x 8 due to the arrangement of the electronics. This mirroring did not exhibit significant advantages in cross-polarization due to the highly symmetrical arrangement of the antenna above the layer 3 ground plane.

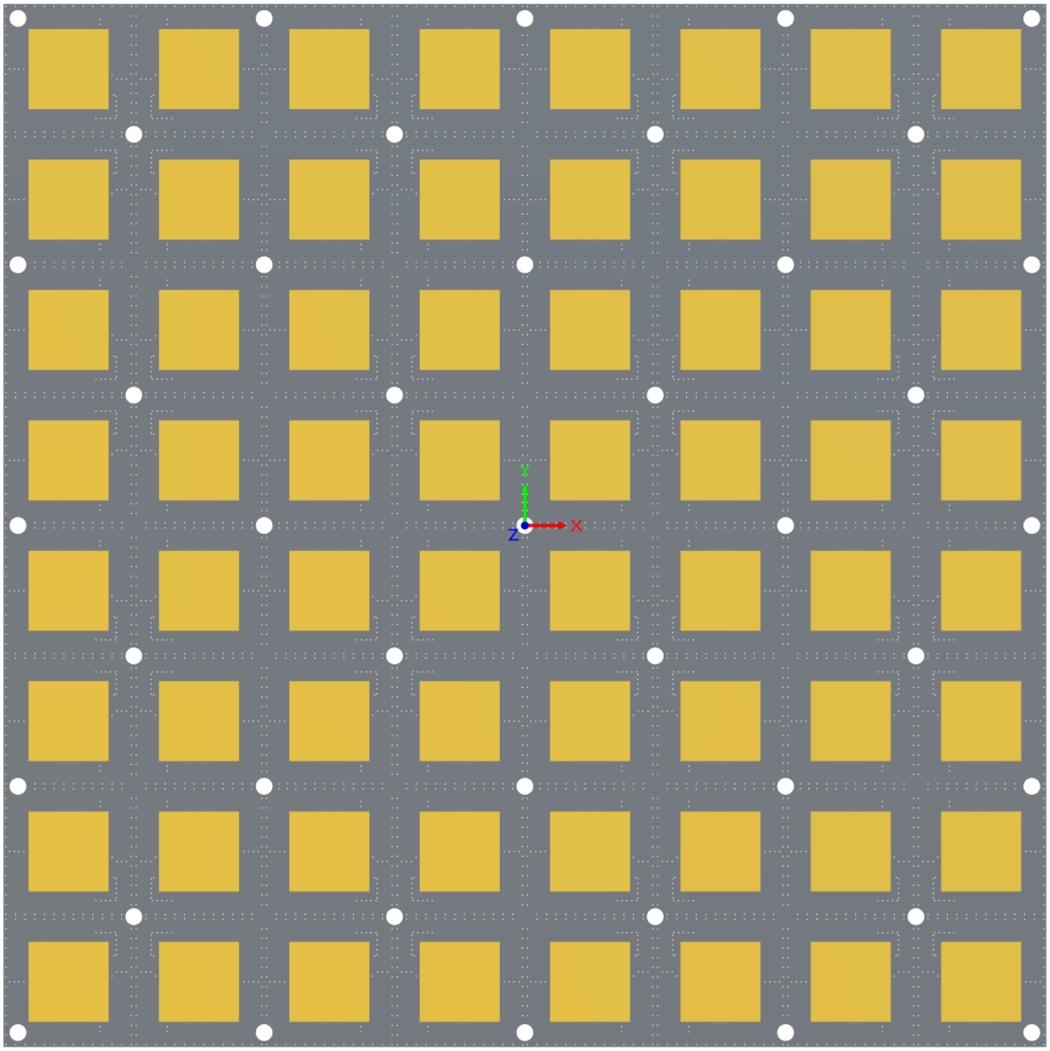

Figure B.9: Parasitic microstrip patch layer of PAIR antenna.

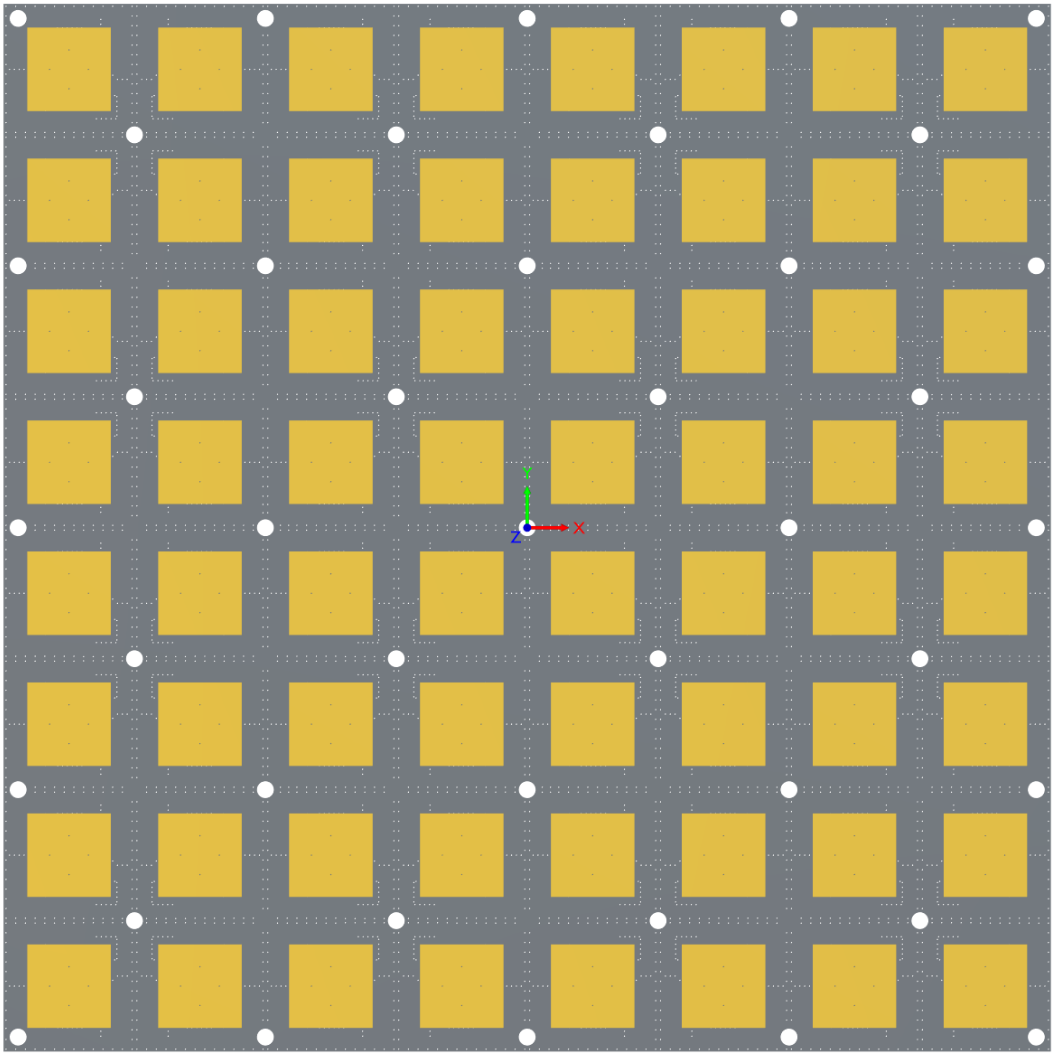

Figure B.10: Driven microstrip patch layer of PAIR antenna.

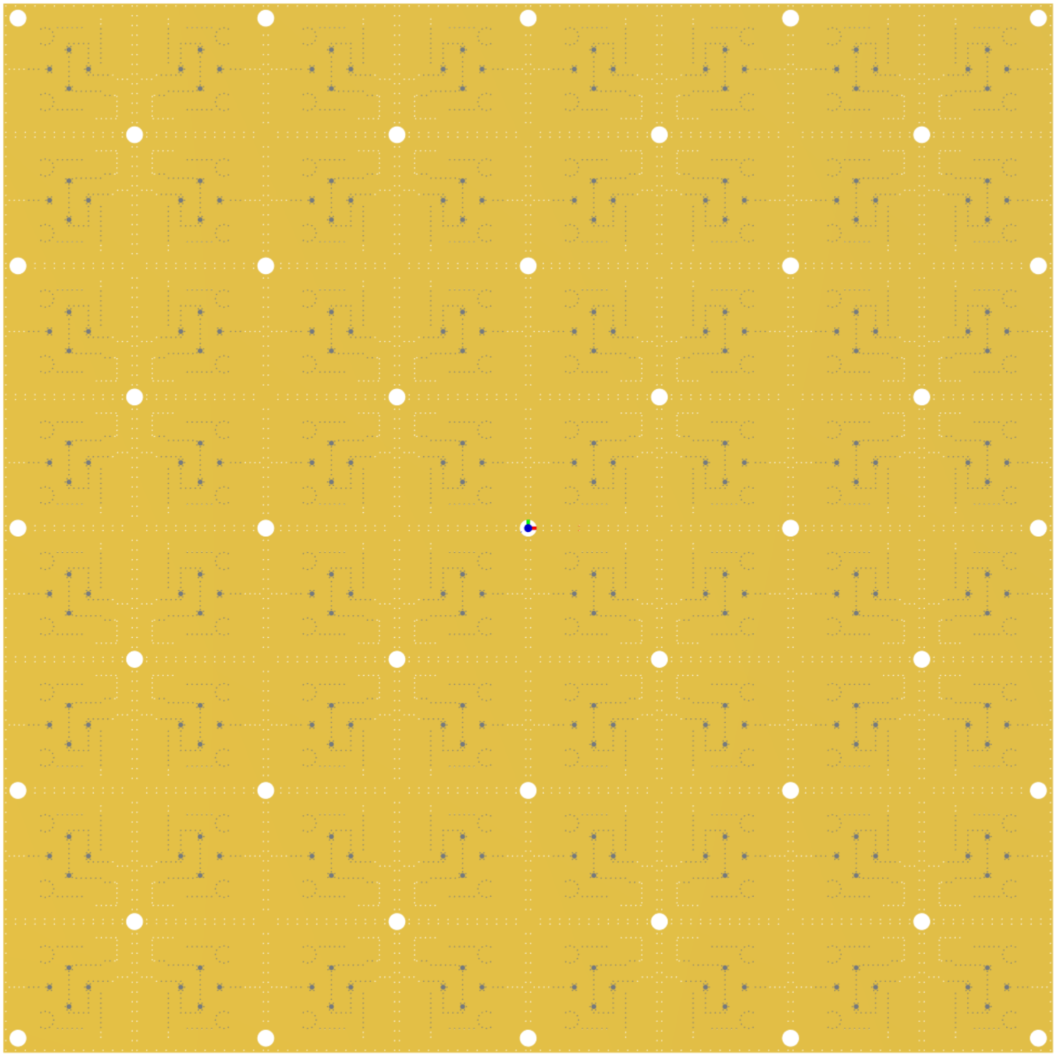

Figure B.11: Microstrip patch ground layer of PAIR antenna.

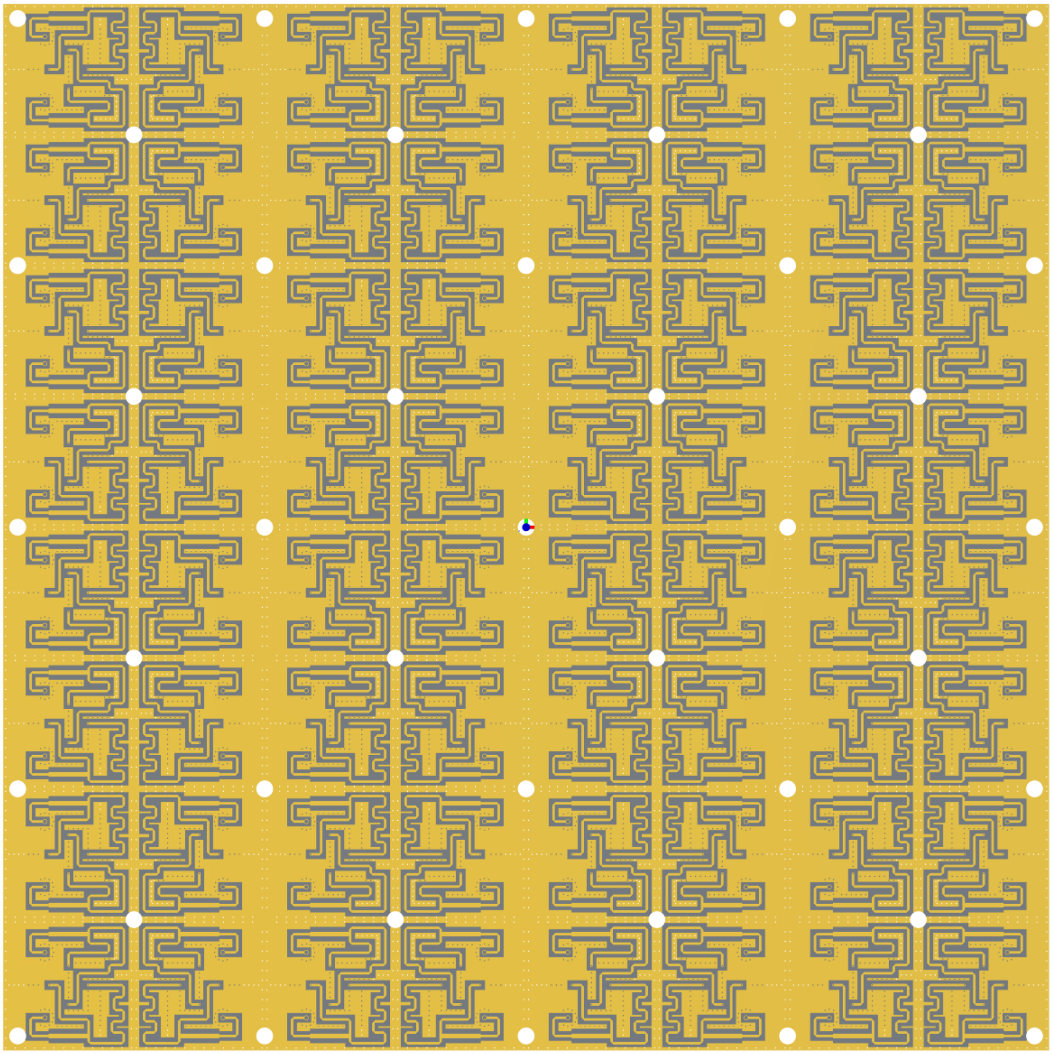

Figure B.12: Feeding network layer of PAIR antenna.

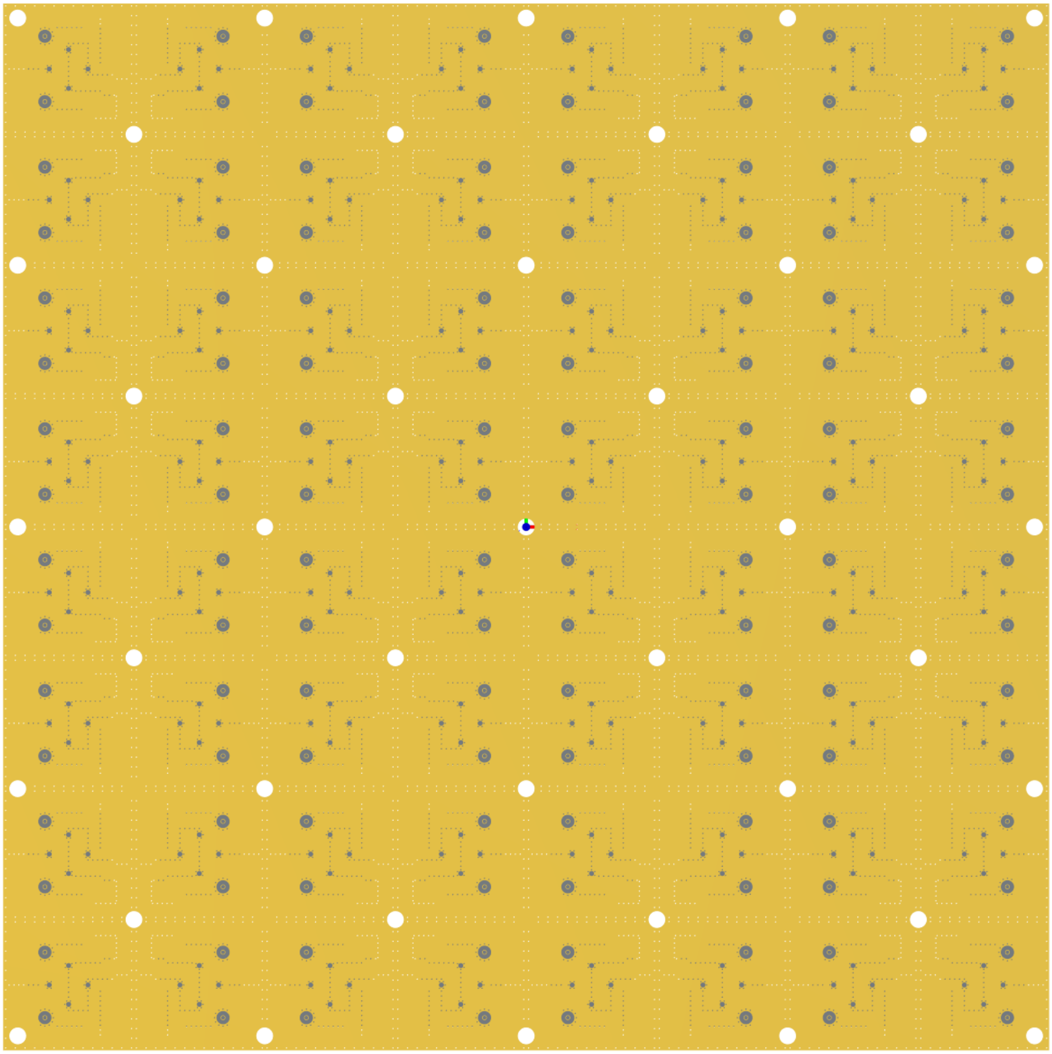

Figure B.13: Bottom ground layer of PAIR antenna.

Appendix C

Summary of Contributions

Journal Papers

[1] **Diaz, J.D.**, Salazar, J.L., Ortiz, J.A., Aboserwal, N., Lebron, R.M., Fulton, C., & Palmer, R. (2018). “A Cross-Stacked Radiating Antenna with Enhanced Scanning Performance for Digital Beam-Forming Multifunction Phased-Array Radars.” *Transactions on Antennas and Propagation*, Vol. 66, No. 10, pp. 5258-5267.

[2] J. A. Ortiz, J. L. Salazar-Cerreno, **J. D. Díaz**, R. M. Lebrón, N. A. Aboserwal and L. Jeon, ”Low-Cost CMOS Active Array Solution for Highly Dense X-Band Weather Radar Network,” in IEEE Transactions on Antennas and Propagation, vol. 68, no. 7, pp. 5421-5430, July 2020

[3] Aboserwal, N., Salazar, J.L., **Diaz, J.D.**, Ortiz, J.A., & Fulton, C. (2018). “Source Current Polarization Impract on the Cross-Polarization Definition of Practical Antenna Elements: Theory and Applications.” *Transactions on Antennas and Propagation*, Vol. 66, No. 9, pp. 4391-4406.

Refereed Conference Papers

[1] R. Lebrón, **J. D. Diaz** and J. L. Salazar-Cerreno, ”A Procedure to Characterize and Predict Active Phased Array Antenna Radiation Patterns from Planar Near-Field Measurements,” 2018 AMTA Proceedings, Williamsburg, VA, 2018, pp. 1-4.

[2] **Diaz, J.D.**, Aboserwal, N., Logan, J.T., Kindt, R.W., Salazar, J.L. (2019). “Ultra-Low Cross Polarization Microstrip Patch Antennas for Phased Arrays” *2019 IEEE International Symposium on Phased Array System & Technology (PAST)*, Boston, MA.

[3] **Diaz, J.D.**, Salazar, J.L., Ortiz, J.A., Aboserwal, N., Fulton, C., & Palmer, R. (2016). “A Dual-Polarized Stacked Patch Antenna with Wide-Angle and Low Cross-Polarization for Fully Digital Multifunction Phased Array Radars.” *2016 IEEE International Symposium on Phased Array Systems and Technology (PAST)* Boston, MA.

[4] Ortiz, J.A., Salazar, J.L., **Diaz, J.D.**, Aboserwal, N., Jeon, L., Sim, S., & Chun, J. (2016). “Ultra-Compact Universal Polarization X-band Unit Cell for High-Performance Active Phased Array Radar.” *2016 IEEE International Symposium on Phased Array Systems and Technology (PAST)* Boston, MA.

[5] Salazar, J.L., Aboserwal, N., **Diaz, J.D.**, Ortiz, J.A., Fulton, C. (2016). “Edge Diffraction Impact on the Cross-Polarization Performance of Active Phased Array Antennas.” *2016 IEEE International Symposium on Phased*

Array Systems and Technology (PAST) Boston, MA.

Student Paper Competition Awards

[1] Best Paper Award - 2016 IEEE International Symposium on Phased Array Systems & Technology - Waltham, MA

[2] Best Paper Award - 2015 AMS Transition of Research to Operations - Phoenix, AZ

Other Conference Papers

[1] Salazar, J., Ortiz, J., **Diaz, J.D.**, Aboserwal, N., Yu, T., Fulton, C., Yeary., M., & Palmer, R. (2018). “Update of a Low-Profile C-band Active Array Antenna for a Polarimetric Imaging Radar System.” *IEEE International Symposium on Antennas and Propagation / USNC-URSI Radio Science Meeting.* Boston, MA.

[2] Salazar, J., **Diaz, J.D.**, Ortiz, J., Fulton, C., Aboserwal, N., Sigmarsson, H., Yeary., M., & Palmer, R. (2018). “An Ultra Low-Cross-Polarization S-band Active Array Antenna for a Fully Digital Polarimetric Phased Radar System.” *IEEE International Symposium on Antennas and Propagation / USNC-URSI Radio Science Meeting.* Boston, MA.

[3] Salazar, J., Ortiz, **J.D., Diaz**, J., Aboserwal, N., Yu, T., Fulton, C., Yeary., M., & Palmer, R. (2018). “A Low-Profile C-band Active Array Antenna for a Multifunction Polarimetric Imaging Radar System.” *48th European Microwave Conference.* Madrid, Spain.

[4] Aboserwal, N., Salazar, J., Ortiz, & **J.D., Diaz**, J. (2017). “The Impact of Higher Order Modes on the Cross Polarization Levels of a Rectangular Patch Antenna.” *Symposium on Antennas and Propagation / URSI Radio Science.* San Diego, CA.

[5] **Diaz, J.D.**, Estupinan, J., & Konarik, S. (2014). “Using Atmospheric Freezing Level to Predict Severe Hail in WFO Miami County Warning Area.” *26th Conference on Weather Analysis and Forecasting / 22nd Con-*

ference on Numerical Weather Prediction. Atlanta, GA.